Karlsruhe Institute of Technology

Seismic investigation of subsurface structure at the Herrenknecht test site - V_S and Q

Master's thesis of

Ahmad Rasho

at the Geophysical Institute (GPI)
KIT-Department of Physics
Karlsruhe Institute of Technology (KIT)

Date of submission:
18.06.2025

Supervisor:	Prof. Dr. Thomas Bohlen
Co-supervisor:	apl. Prof. Dr. Joachim Ritter
Advisor:	Dr. Laura Gaßner
Co-advisor:	Dr. Thomas Hertweck

Erklärung / Statutory declaration

Ich versichere wahrheitsgemäß, die Arbeit selbstständig verfasst, alle benutzten Hilfsmittel vollständig und genau angegeben und alles kenntlich gemacht zu haben, was aus Arbeiten anderer unverändert oder mit Abänderungen entnommen wurde sowie die Satzung des KIT zur Sicherung guter wissenschaftlicher Praxis in der momentan gültigen Fassung beachtet zu haben.

I declare truthfully that I have written this thesis all by myself, that I have fully and accurately specified all auxiliary means used, that I have correctly cited (marked) everything that was taken, either unchanged or with modification, from the work of others, and that I have complied with the current version of the KIT statutes for safeguarding good scientific practice.

Karlsruhe, 18.06.2025

Signature: Ahmad Rasho

Abstract

Deep geothermal energy is considered a crucial renewable resource for future electricity and heat generation, particularly in urban environments. To reduce the risk associated with costly drilling for urban geothermal reservoirs, vibroseis measurement campaigns must be undertaken. This requirement is addressed by the Urban Vibroseis Truck (UVT), which enables high-resolution surveys in spatially constrained settings.

This work presents the first geophysical characterization of the subsurface at the Herrenknecht UVT test site. The objective was to provide an initial model for future full-wave inversion processes and for subsequent validation of the ground force signal generated by the urban vibration truck. To achieve this, a one-dimensional shear-wave velocity (V_S) profile was created using the multichannel analysis of surface waves (MASW), along with an estimate of the Rayleigh wave quality factor (Q) using the spectral ratio method.

The resulting 1D V_S models revealed significant near-surface heterogeneity—up to 2 m in one of the measured profiles, attributed to variable fill material. In contrast, the deeper layers exhibited consistent stratigraphy and velocity structures. Forward modeling was conducted using `SOFI2D` software to validate the shear-wave profiles. This was achieved by comparing synthetic and observed seismograms and dispersion images, which highlighted discrepancies in certain shots and convergence in others taken at different locations.

The attenuation properties were estimated using the spectral ratio method, which had first been validated through analytical and synthetic viscoelastic models prior to application to the field data. The resulting Q values provided a global measure of site attenuation and demonstrated robustness under well-controlled conditions.

List of Figures

2.1 Neighborhood of P and Q before and after deformation (Müller and Weber, 2007). . . . 4
2.2 Displacement of elastic particles during the passage of P and S body waves, as well as Rayleigh and Love surface waves (Clauser, 2018). . . . 7
2.3 Layered half-space with free surface (Müller and Weber, 2007). . . . 8
2.4 Rayleigh wave components with different wavelengths propagating through a layered medium. Wave components at varying frequencies reflect soil properties at corresponding depths (Olafsdottir, 2016). . . . 11
2.5 Schematic diagram of generalized standard linear solid (GSLS) composed of L so-called relaxation mechanisms or Maxwell bodies. k_l and η_l $(l = 1, \dots L)$ represent elastic moduli and Newtonian viscosities, respectively (Bohlen, 2002). . . . 13

3.1 Overview of MASWaves (*MASWaves User Manual* 2017). . . . 21
3.2 Example of a MASW measurement profile. A line-up of $N = 24$ geophones with equal spacing dx is shown. The source offset is denoted as x_1. The length of the receiver spread is L, and the total length of the measurement profile is L_T (Olafsdottir et al., 2018). . . . 22
3.3 Effect of topography on surface-wave generation and the quality of MASW data. O denote correct acquisition, while X indicate incorrect one (C. B. Park and Adkins-Heljeson, 2006). . . . 23
3.4 Overview of the dispersion analysis (Olafsdottir et al., 2018). . . . 24
3.5 Layered Earth model used for inversion analysis (Olafsdottir et al., 2018). . 28
3.6 Overview of automatic inversion algorithm. . . . 31

4.1 Side trench excavated at the Herrenknecht test site (Photograph by Thomas Hertweck). . . . 34
4.2 Shallow borehole, approximately 30 cm deep, at the Herrenknecht test site (Photograph by the author). . . . 34
4.3 Herrenknecht test site. The blue and red lines indicate the locations and directions of the first and second profiles, respectively. The brown circle marks the location of the shallow borehole, and the black line shows the position of the side trench (source: Google Maps). . . . 36
4.4 MASW field acquisition configuration at the Herrenknecht test site (Photograph by the author). . . . 36
4.5 Seepage trench and displacement of the geophones (Photograph by the author). 37

5.1 Seismograms from shot 1 (a), shot 10 (c), and shot 20 (e), along with their corresponding dispersion images (b, d, and f). . . . 41
5.2 Seismograms from shot 28 (a), shot 37 (c), and shot 47 (e), along with their corresponding dispersion images (b, d and f). . . . 42

5.3 Dispersion images for shots 1 through 20, with the corresponding picked dispersion curve indicated by red points. 44
5.4 Dispersion images for shots 28 through 47, with the corresponding picked dispersion curve indicated by red points. 45
5.5 Comparison of inversion results for shot 1 with c_T = 2, 1, 0.1, and 0.03 m/s: (top) dispersion curves; (middle) misfit histories; and (bottom) shear-wave velocity profiles. 47
5.6 Inversion results from all shots along the first profile: (a) theoretical dispersion curves—frequency versus Rayleigh-wave velocity; (b) theoretical dispersion curves—Rayleigh-wave velocity versus wavelength. 49
5.7 Inversion results from all shots along the first profile: (a) shear-wave velocity profiles; and (b) the median shear-wave velocity profile with its standard deviation. 50
5.8 Inversion results from all shots along the second profile: (a) theoretical dispersion curves—frequency versus Rayleigh-wave velocity; (b) theoretical dispersion curves—Rayleigh-wave velocity versus wavelength. 51
5.9 Inversion results from all shots along the second profile: (a) shear-wave velocity profiles; and (b) the median shear-wave velocity profile with its standard deviation. 52
5.10 Inversion results for both profiles: (a) median shear-wave velocity profiles of the first and second profiles; and (b) the total median shear-wave velocity profile, including its standard deviation. 53
5.11 Comparison between the observed real data from shots 1 and 20 of the first profile and the synthetic viscoelastic modeled data, calculated using an approximate quality factor of $Q = 15$. 56
5.12 Comparison between the observed real data from shots 28 and 47 of the second profile and the synthetic viscoelastic modeled data, calculated using an approximate quality factor of $Q = 15$. 57

6.1 3D analytical shot gather with a constant quality factor of $Q = 20$. 60
6.3 Global Q value computed from all traces of the 3D analytical shot gather. . 61
6.2 Results of the spectral ratio method applied to the 3D analytical solution of the acoustic wave equation with a constant quality factor ($Q = 20$): (a) amplitude spectra within the frequency range of 10–70 Hz; (b) log-spectral ratios for offsets of 10, 20, 30, 40, 50, 60, and 70 m; (c), (d), and (e) linear regressions applied to the log-spectral ratios corresponding to trace pairs for $x_1 = 5, 10, 40$ m and $x_2 = 70$ m; and (f) median Q values and associated median errors derived from multiple trace pairs using trace 5 as a reference. 62
6.4 Approximation of $Q = 20$ using five L-relaxation mechanisms and the corresponding relaxation frequencies. 63
6.5 Viscoelastic modeled shot gather with an approximated $Q = 20$: (a) without applying a window and (b) with a window applied to isolate the Rayleigh wave from other wave phases. 64
6.6 Results of the spectral ratio method applied to windowed viscoelastic modeled shot gather with a homogeneous approximated quality factor ($Q = 20$). (a) amplitude spectra within the frequency range of 5–45 Hz; (b) log-spectral ratios for offsets of 10, 20, 30, 40, 50, 60, and 70 m; (c), (d), and (e) linear regressions applied to the log-spectral ratios corresponding to trace pairs for $x_1 = 5, 10, 40$ m and $x_2 = 70$ m; and (f) median Q values and associated median error derived from multiple trace pairs using trace 30 as reference. . 65
6.7 Global Q value computed using all traces of viscoelastic modeled shot gather. (a) with applying a window; (b) without applying a window. 66

6.8 Shot 1 from field data. (a) shows the data without applying a window; (b) displays the result after applying a window to isolate the Rayleigh wave from other seismic phases. 66
6.9 Results of the spectral ratio method applied to field data shot 1, with a source offset of 1 m: (a) amplitude spectra within the frequency range of 5–120 Hz; (b) log-spectral ratios computed for offsets of 10, 20, 30, 40, 50, 60, and 70 m; (c), (d), and (e) linear regressions applied to the log-spectral ratios corresponding to trace pairs for $x_1 = 5, 10, 40$ m and $x_2 = 70$ m; and (f) median Q values and associated median error derived from multiple trace pairs using trace 30 as reference. 68
6.10 Global Q values computed from field data using all traces for: (a) windowed shot 1; (b) non-windowed shot 1; (c) windowed shot 10; and (d) non-windowed shot 10. 69
6.11 Global Q value for the first and second profiles. 69

List of Tables

4.1 Soil stratigraphy and initial shear-wave velocity estimates at the test site . 34
4.2 Overview of MASW configuration at the Herrenknecht test site. 35

5.1 Initial model parameters used for the inversion analysis. 46
5.2 Inversion model parameters for the first and second profiles, along with the total median values and their associated uncertainties. 53
5.3 SOFI2D model parameter; Depth (z), S-wave velocity (β), P-wave velocity (V_P), density (ρ), quality factors (Q_S, Q_P), number relaxation mechanisms (L), relaxiation of frequencies (f) and relaxation time (τ). 54

6.1 Inversion model parameters for the first and second profiles (P1 and P2), along with the estimated quality factors of Rayleigh wave (Q), S-wave (Q_S), and P-wave (Q_P). 70

Contents

Erklärung / Statutory declaration **iii**

Abstract **v**

List of Figures **vii**

List of Tables **xi**

1 Introduction **1**

2 Theoretical foundations **3**
2.1 Analysis of strain . . . 3
2.1.1 Components of the displacement vector . . . 3
2.1.2 Equilibrium conditions . . . 4
2.2 Wave types . . . 5
2.2.1 Body waves . . . 6
2.2.2 Surface waves . . . 8
2.3 Attenuation . . . 12
2.4 Q factor and spectral ratio method . . . 15

3 MASWaves software - applications and workflow **19**
3.1 Overview of the multichannel analysis of surface waves (MASW) . . . 19
3.2 MASWaves software - workflow . . . 20
3.2.1 Field acquisition . . . 20
3.2.2 Dispersion analysis . . . 23
3.2.3 Inversion analysis . . . 27
3.2.4 Automatic inversion algorithm . . . 30

4 Site description and field acquisition **33**
4.1 Geological structure and subsurface conditions . . . 33
4.2 MASW field acquisition and survey design . . . 35

5 Multichannel analysis of surface waves applied to field data **39**
5.1 Field data and dispersion analysis . . . 39
5.2 Inversion analysis . . . 46
5.3 Model validation through synthetic and observed data comparison . . . 54
5.4 Discussion . . . 58

6 Estimation of quality factor (Q) **59**
6.1 Application of spectral ratio method . . . 59
6.1.1 Applications on analytical solution of acoustic seismic wave . . . 60

6.1.2 Applications on viscoelastic FD-modeled shot gather 63
6.1.3 Application on real data 66
6.2 Discussion 70

7 Summary **71**

A Software **73**

B Seismogram/Dispersion images of Herrenknecht test site **85**

Bibliography **97**

Acknowledgments **99**

Chapter 1

Introduction

The UVT project was designed to develop, construct, and validate a novel urban mobile seismic vibrator through geophysical field experiments. The engineering development of the vibrator has been led by Herrenknecht GmbH, while field validation is currently being conducted by the Geophysical Institute at the Karlsruhe Institute of Technology (KIT). A principal objective of the project is to validate the ground force emitted by the vibrator using multiple methodologies, thereby allowing for a comprehensive evaluation of the system's performance. These methodologies necessitate homogeneous subsurface conditions to decouple the effects of vibrator performance from those of ground heterogeneity.

This thesis presents the first geophysical characterization of the subsurface at the Herrenknecht test site. A one-dimensional shear-wave velocity profile (1D V_S) was developed using the multichannel analysis of surface waves (MASW) technique. Additionally, the quality factor (attenuation) of the test site was estimated using the spectral ratio method. The study integrates both theoretical groundwork and practical application, employing the open-source software `MASWaves` Olafsdottir et al. (2018) for processing and analyzing multichannel surface wave records.

The thesis begins with a theoretical overview of elastic wave propagation, distinguishing between body waves and surface waves. Particular emphasis is placed on Rayleigh waves, focusing on their properties and dispersion behavior in vertically heterogeneous media. The geophysical model used to describe attenuation is explained, and the spectral ratio method for estimating the quality factor is presented. Subsequently, the geological setting and preliminary subsurface conditions at the test site are summarized.

The implementation of the MASW methodology is described in a structured three-step workflow:

1. **Seismic Data Acquisition:** Seismic signals are generated using impulse sources (sledgehammer) and recorded along two perpendicular linear profiles.
2. **Dispersion Analysis and Curve Extraction:** The recorded data were processed to produce dispersion images that illustrate the frequency-dependent behavior of the surface waves. Fundamental-mode dispersion curves were then extracted, capturing the frequency-dependent velocity variations.
3. **Inversion Analysis:** The extracted dispersion curves were inverted to obtain a one-dimensional shear-wave velocity profile, providing a quantitative representation of the subsurface.

The derived 1D profile was subsequently employed in the forward modeling of viscoelastic waveforms using `SOFI2D` software (Bohlen et al., 2016). These synthetic seismograms were

then compared to observed field data and the dispersion images from various shot locations, allowing an assessment of model accuracy and reliability. The results are critically evaluated, with particular focus on the potential limitations inherent in the MASW technique.

Finally, the quality factor was estimated using the spectral ratio method. This approach was first validated through analytical solutions of acoustic wave and viscoelastic synthetic data. The validated method was then applied to the full dataset, using all traces from each shot, and a global median value was computed to characterize site attenuation properties.

Chapter 2

Theoretical foundations

One of the principal objectives in geophysics is the determination of subsurface soil parameters and the delineation of structural characteristics. In this section, the physical principles governing seismic wave propagation—including wave types and their properties—are presented following the frameworks established by Müller and Weber (2007), Lay and Wallace (1995), Clauser (2018), and Olafsdottir (2016).

To ensure clarity in the mathematical description of the theory, we employ index notation for vectors and Einstein's summation convention.

2.1 Analysis of strain

2.1.1 Components of the displacement vector

Consider a body subjected to external forces and consequently deformed. A point P located at x_i is displaced to P' by a vector u_i (Fig. 2.1), while a neighboring point Q, initially at $x_i + y_i$, is displaced to Q' according to

$$z_i = u_i + \mathrm{d}u_i = u_i + \frac{\partial u_i}{\partial x_j} y_j \tag{2.1}$$

The resulting change z_i in the vicinity of point P is composed of translation, deformation and rotation components:

$$z_i = \underbrace{u_i}_{\text{translation}} + \underbrace{\varepsilon_{ij} y_j}_{\text{deformation}} + \underbrace{\xi_{ij} y_j}_{\text{rotation}} \tag{2.2}$$

where the strain and rotation tensors are defined as

$$\varepsilon_{ij} = \frac{1}{2}\left(\frac{\partial u_i}{\partial x_j} + \frac{\partial u_j}{\partial x_i}\right), \quad \xi_{ij} = \frac{1}{2}\left(\frac{\partial u_i}{\partial x_j} - \frac{\partial u_j}{\partial x_i}\right) \tag{2.3}$$

The symmetric tensor ε_{ij} characterizes the deformation, while the antisymmetric tensor ξ_{ij} represents the rotation.

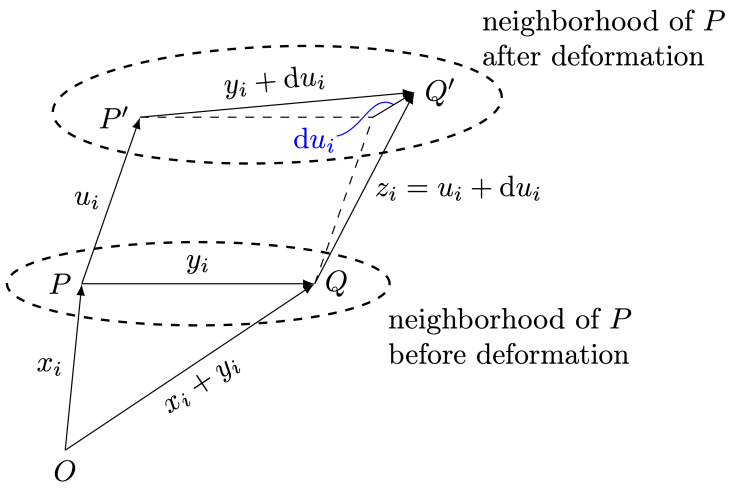


Figure 2.1: *Neighborhood of P and Q before and after deformation (Müller and Weber, 2007).*

2.1.2 Equilibrium conditions

For a deformable body, the conditions of equilibrium are satisfied when the resultant force and moment vanish:

$$\int_V \vec{F}\, dV + \int_S \vec{P}\, df = 0 \quad \text{(force)} \tag{2.4}$$

$$\int_V (\vec{x} \times \vec{F})\, dV + \int_S (\vec{x} \times \vec{P})\, df = 0 \quad \text{(moment)} \tag{2.5}$$

Here, $\vec{F}$ denotes the body force (including inertial effects), and $\vec{P}$ represents the traction vector acting on the surface S with outward unit normal $\vec{n}$. By expressing $\vec{P}$ through the stress tensor p_{ij} as $P_i = p_{ij} n_j$, and by applying Gauss's theorem, the following relation is obtained:

$$\int_S P_{in}\, df = \int_V \nabla \cdot \vec{P}_i\, dV \tag{2.6}$$

which leads to the result

$$\int_V \left(F_i + \nabla \cdot \vec{P}_i\right) dV = 0 \tag{2.7}$$

Because this condition must hold for any arbitrary volume V, the integrand must be identically zero. Employing the Einstein summation convention, the equilibrium condition is then given by

$$F_i + \frac{\partial p_{ij}}{\partial x_j} = 0 \tag{2.8}$$

where the components of the body force vector $\vec{F}$ are defined as

$$F_i = -\rho \frac{\partial^2 u_i}{\partial t^2} + f_i \tag{2.9}$$

The first term represents the inertial forces, while f_i is taken to encompass all other body forces. Here, ρ denotes the mass density, and u_i represents the displacement components. Accordingly, the equation of motion is expressed as

$$\rho \frac{\partial^2 u_i}{\partial t^2} = \frac{\partial p_{ij}}{\partial x_j} + f_i \tag{2.10}$$

This means that the displacement u_i from the prestressed state depends only on the additional stress and the additional body forces. If the body is initially at rest, then $p_{ij} = 0$ and $f_i = 0$.

The response of the medium to applied forces is characterized by the theory of linear elasticity, wherein a linear stress-strain relationship is assumed. Under this theoretical framework, elastic deformations are considered infinitesimal.

In an elastic medium, the stress tensor p_{ij} is related to the strain tensor via Hooke's law:

$$p_{ij} = C_{ijkl} \varepsilon_{kl} \tag{2.11}$$

where C_{ijkl} denotes the elasticity tensor, which encapsulates the material's elastic moduli. Due to the symmetry of the deformations and stress tensors and conservation of the elastic deformation energy. The number of components reduces from 81 to 21. This is the maximum number of (independent) elasticity constants an anisotropic body can have. For isotropic media, the elasticity tensor is expressed in terms of only two Lamé parameters, λ and μ, as follows:

$$p_{ij} = \lambda \, \varepsilon_{kk} \, \delta_{ij} + 2\mu \, \varepsilon_{ij} \tag{2.12}$$

In this context, μ, which represents the shear modulus, quantifies the material's resistance to shear deformation.

2.2 Wave types

The equation of motion independent of the coordinate system is given by

$$\rho \frac{\partial^2 \vec{u}}{\partial t^2} = (\lambda + 2\mu) \nabla \nabla \cdot \vec{u} - \mu \nabla \times \nabla \times \vec{u} + \vec{f} \tag{2.13}$$

$\vec{f}$ contains only the body forces that act in addition to those of the forces at rest.

The ground displacement field $\vec{u}$ is expressed in terms of elastic potentials: the scalar compressional potential Φ and the vector shear potential $\vec{\Psi}$, as follows:

$$\vec{u} = \nabla \Phi + \nabla \times \vec{\Psi} \tag{2.14}$$

Similar to $\vec{u}$, the body force ($\vec{f}$) can be written as

$$\vec{f} = \nabla\varphi + \nabla \times \vec{\psi} \tag{2.15}$$

By inserting the ground displacement field Eq. 2.14 and the body force Eq. 2.15 in Eq. 2.13, the following is obtained:

$$\nabla^2\Phi - \frac{1}{\alpha^2}\frac{\partial^2\Phi}{\partial t^2} = -\frac{\varphi}{\lambda + 2\mu} \quad \text{with} \quad \alpha^2 = \frac{\lambda + 2\mu}{\rho} \tag{2.16}$$

$$-\nabla \times \nabla \times \vec{\Psi} - \frac{1}{\beta^2}\frac{\partial^2\vec{\Psi}}{\partial t^2} = -\frac{\vec{\psi}}{\mu} \quad \text{with} \quad \beta^2 = \frac{\mu}{\rho} \tag{2.17}$$

2.2.1 Body waves

In an isotropic elastic medium, two types of waves are observed: compressional waves (P-waves) and shear waves (S-waves). Both are classified as body waves, as their propagation occurs throughout the Earth's interior, in contrast to surface waves.

P-Wave

Compressional waves—commonly referred to as longitudinal waves—are characterized by oscillations that occur parallel to the direction of wave propagation. Their velocity, as shown in Eq. 2.16, is given by

$$\alpha = \sqrt{\frac{\lambda + 2\mu}{\rho}}$$

Seismological observations commonly designate P-waves as primary waves because their velocity consistently exceeds that of S-waves.

S-Wave

Shear waves, also known as transverse waves, exhibit oscillations that are oriented perpendicular to the direction of wave propagation. The velocity of S-wave propagation is given by

$$\beta = \sqrt{\frac{\mu}{\rho}}$$

It is invariably lower than the velocity of P-waves. Consequently, S-waves are conventionally referred to as secondary waves.

In fluids or gases—the acoustic case—only P-waves are able to propagate, as the shear modulus μ vanishes. Under this condition, the wave velocities reduce to

$$\alpha = \sqrt{\frac{\lambda}{\rho}} \tag{2.18}$$

$$\beta = 0 \tag{2.19}$$

Fig. 2.2 illustrates the various types of wave-induced particle displacements.

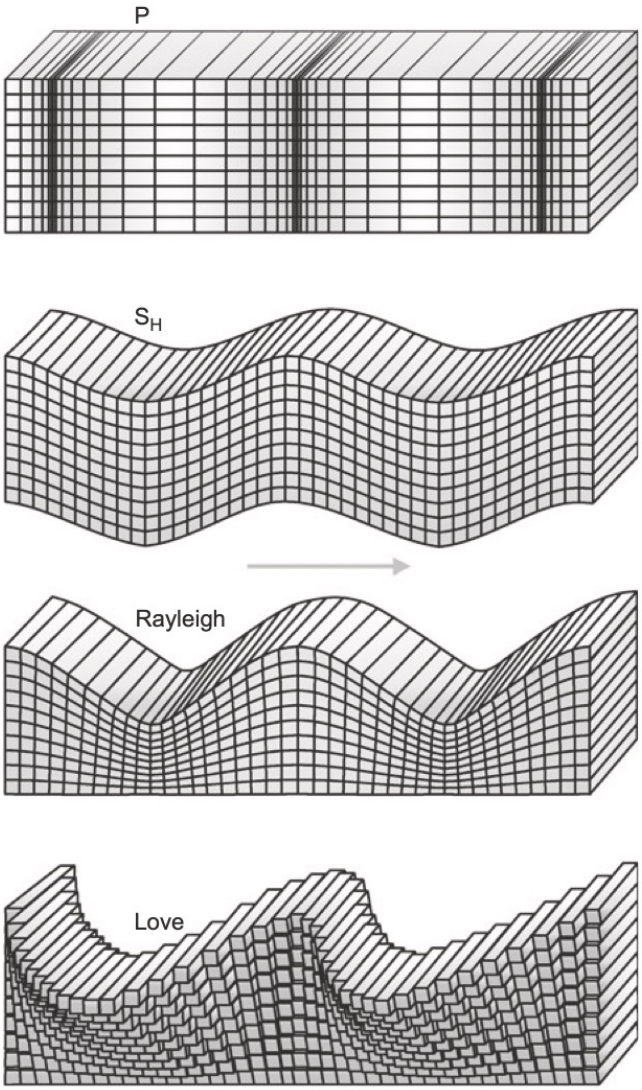


Figure 2.2: *Displacement of elastic particles during the passage of P and S body waves, as well as Rayleigh and Love surface waves (Clauser, 2018).*

2.2.2 Surface waves

Apart from body waves, the near-surface region of the Earth predominantly confines another category of seismic waves. These are known as surface waves (Rayleigh and Love waves). Surface waves propagate along the Earth's surface, and their amplitudes are significant only within a depth of a few wavelengths.

Free surface waves in layered media

A layered half-space is considered, as illustrated in Fig. 2.3.

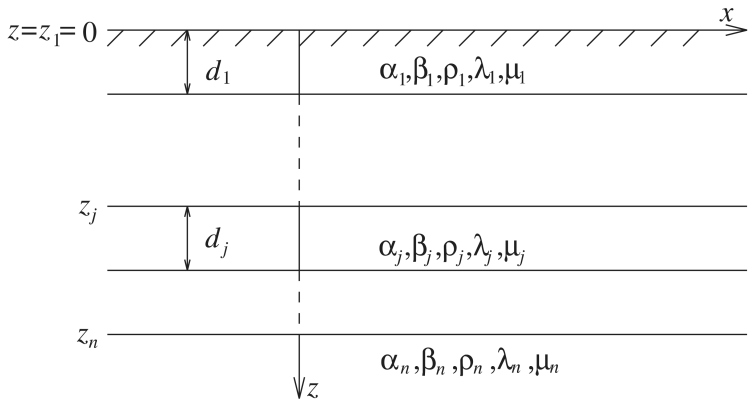


Figure 2.3: *Layered half-space with free surface (Müller and Weber, 2007).*

Using Cartesian coordinates x, y, and z, and assuming independence from y, the displacement field is decomposed into contributions from P-, SV-, and SH-waves. SV-waves exhibit vertically polarized particle motion in a vertical plane perpendicular to the direction of propagation, while SH-waves exhibit horizontally polarized motion in a horizontal plane perpendicular to the direction of propagation. Surface waves resulting from P–SV-wave coupling are referred to as Rayleigh waves and are polarized in the x–z plane.

$$\begin{aligned} \text{Horizontal displacement:} \quad u &= \frac{\partial \Phi}{\partial x} - \frac{\partial \Psi}{\partial z} \\ \text{Vertical displacement:} \quad w &= \frac{\partial \Phi}{\partial z} + \frac{\partial \Psi}{\partial x} \end{aligned} \tag{2.20}$$

The potentials Φ and Ψ satisfy the wave equation:

$$\nabla^2 \Phi = \frac{1}{\alpha^2} \frac{\partial^2 \Phi}{\partial t^2}, \quad \nabla^2 \Psi = \frac{1}{\beta^2} \frac{\partial^2 \Psi}{\partial t^2} \tag{2.21}$$

Surface waves involving only SH-motion are referred to as Love waves. These are polarized in the y-direction, and the displacement v in each layer satisfies the wave equation:

$$\nabla^2 v = \frac{1}{\beta^2} \frac{\partial^2 v}{\partial t^2}$$

For harmonic excitation ($\omega > 0$), the assumed solution (ansatz) for Φ_j, Ψ_j, and v_j in the j-th layer is given by

$$\begin{Bmatrix} \Phi_j \\ \Psi_j \\ v_j \end{Bmatrix} = \begin{Bmatrix} A_j(z) \\ B_j(z) \\ C_j(z) \end{Bmatrix} \exp\left[i\omega\left(t - \frac{x}{c}\right)\right] = \begin{Bmatrix} A_j(z) \\ B_j(z) \\ C_j(z) \end{Bmatrix} \exp\left[i(\omega t - kx)\right] \tag{2.22}$$

For a homogeneous half-space, the following boundary condition must be satisfied:

$$\lim_{z\to\infty} \begin{Bmatrix} A_j(z) \\ B_j(z) \\ C_j(z) \end{Bmatrix} = 0 \tag{2.23}$$

The problem constitutes an eigenvalue problem, with c (the phase velocity) and $k = \omega/c$ as eigenvalues. (For fixed ω), a finite number (≤ 1) of eigenvalues exist. Here, only the case where the eigenvalues are real and non-negative is considered, as it is of greatest practical importance. The corresponding surface waves are referred to as normal modes.

Rayleigh waves at the surface of a homogeneous half-space

For a homogeneous half-space ($z > 0$), characterized by P- and S-wave velocities α and β, respectively, the following ansatz is considered:

$$\Phi = A(z)\exp[i(\omega t - kx)], \quad \Psi = B(z)\exp[i(\omega t - kx)] \tag{2.24}$$

By substituting this ansatz into the wave equation (Eq. 2.21), the following differential equation is obtained:

$$\ddot{A}(z) + k^2\left(\frac{c^2}{\alpha^2} - 1\right)A(z) = 0 \tag{2.25}$$

The general solution of this equation takes the form

$$A(z) = A_1 e^{-ik\delta z} + A_2 e^{ik\delta z}, \quad \text{where } \delta = \sqrt{\frac{c^2}{\alpha^2} - 1} \tag{2.26}$$

From the boundary conditions of Eq. 2.23, it follows that δ must be purely imaginary; therefore, $A_2 = 0$. Consequently, the potentials are given as

$$A(z) = A_1 e^{-ik\delta z}, \quad B(z) = B_1 e^{-ik\gamma z}, \quad \text{where } \gamma = \sqrt{\frac{c^2}{\beta^2} - 1} \tag{2.27}$$

γ is negative imaginary, so it gives further limits for c ($c < \beta$).

Accordingly, the potentials in Eq. 2.24 are now expressed as

$$\Phi = A_! \exp[i(\omega t - kx - k\delta z)], \quad \Psi = B_1 \exp[i(\omega t - kx - k\gamma z)] \tag{2.28}$$

By applying the boundary conditions $p_{zz} = p_{zx} = 0$ at $z = 0$, the following system of equations are obtained:

$$-\frac{\omega^2}{\alpha^2}\frac{\lambda}{\mu}A_1 + 2(-k^2\delta^2 A_1 - k^2\gamma B_1) = 0 \tag{2.29}$$

$$-2k^2\delta A_1 + (-k^2 + k^2\gamma^2)B_1 = 0 \tag{2.30}$$

Upon simplification, this system reduces to

$$\left(\frac{c^2}{\beta^2} - 2\right) A_1 + 2\gamma B_1 = 0 \tag{2.31}$$

$$2\delta A_1 + \left(2 - \frac{c^2}{\beta^2}\right) B_1 = 0 \tag{2.32}$$

Non-trivial solutions for A_1 and B_1 exist only if the determinant of this system equals zero. This condition yields the following equation for c:

$$\left(\frac{c^2}{\beta^2} - 2\right)^2 + 4\delta\gamma = 0 \tag{2.33}$$

Within the range $0 < c < \beta$, this equation simplifies to

$$\left(\frac{c^2}{\beta^2} - 2\right)^2 = 4\left(1 - \frac{c^2}{\beta^2}\right)^{1/2}\left(1 - \frac{c^2}{\alpha^2}\right)^{1/2} \tag{2.34}$$

Squaring both sides yields

$$\frac{c^2}{\beta^2}\left[\frac{c^6}{\beta^6} - 8\frac{c^4}{\beta^4} + \left(24 - 16\frac{\beta^2}{\alpha^2}\right)\frac{c^2}{\beta^2} - 16\left(1 - \frac{\beta^2}{\alpha^2}\right)\right] = 0 \tag{2.35}$$

The trivial solution $c = 0$ is excluded from consideration. For $c = 0$, the expression in brackets is negative, whereas for $c = \beta$, it is positive. Hence, at least one real solution must exist within the interval $0 < c < \beta$. Therefore, a valid solution to the eigenvalue problem is present: a wave can propagate along the surface of a homogeneous half-space, with amplitudes that decay with depth. In this simple case, dispersion does not occur, and c is independent of ω.

However, when the Lamé parameters—and thus α, β, and ρ—vary with depth in a vertically heterogeneous elastic half-space, dispersion arises, and c becomes a function of ω. The corresponding equation is commonly known as the Rayleigh secular equation and is expressed in implicit form as Socco et al. (2010):

$$F_R(\lambda(z), \mu(z), \rho(z), k, \omega) = 0 \tag{2.36}$$

At each frequency ω, non-trivial solutions to the eigenvalue problem that satisfy the boundary conditions for surface wave motion exist only for discrete wavenumbers $k = k_j(\omega)$, where $j = 0, \ldots, N_M - 1$ and N_M denotes the number of modes (Aki and Richards, 2002). Once these wavenumbers are determined, the phase velocities of the Rayleigh waves—i.e., the propagation velocities of individual frequency components—are computed as

$$c_j(\omega) = \frac{\omega}{k_j(\omega)}, \quad j = 0, \ldots, N_M - 1 \tag{2.37}$$

The Rayleigh secular equation cannot be solved analytically; nevertheless, several numerical techniques have been developed to solve the eigenvalue problem defined by Eq. 2.36. The method employed in this study is discussed in chapter 3.

The analysis of surface wave methods has been conducted based on the dispersion properties of Rayleigh waves in a vertically heterogeneous medium. In such media, Rayleigh wave velocity increases with depth, and waves with longer wavelengths—corresponding to lower frequencies—propagate more rapidly than those with shorter wavelengths and higher frequencies. The relationship between frequency f, Rayleigh phase velocity $c(f)$, and wavelength $\lambda(f)$ is expressed as

$$\lambda(f) = \frac{c(f)}{f} \tag{2.38}$$

Accordingly, in Fig. 2.4, only the material properties of the uppermost layer influence the phase velocity of the wave component (1). In contrast, the properties of the deeper subsurface layers affect the phase velocities of wave components (2) and (3).

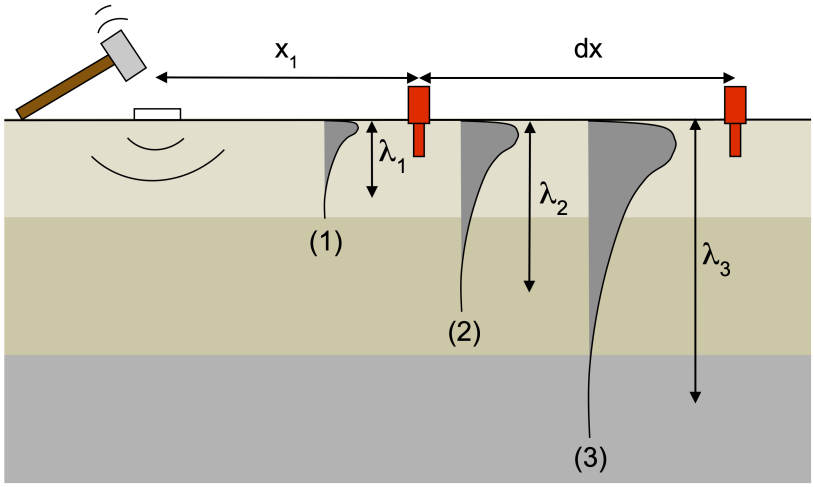


Figure 2.4: *Rayleigh wave components with different wavelengths propagating through a layered medium. Wave components at varying frequencies reflect soil properties at corresponding depths (Olafsdottir, 2016).*

2.3 Attenuation

The amplitude of a seismic wave that travels through anelastic media decreases due to different reasons like geometrical spreading, deflection of the seismic wave due to scattering, and (anelastic) attenuation, which represents the actual dissipation of seismic wave mechanical energy that is then converted to heat. The near-surface produces strong attenuation and thus degrades the quality of seismic images. The mathematical framework that phenomenologically describes the effects of attenuation is the viscoelastic model. In this model, only one additional frequency-dependent parameter, known as the quality factor, denoted by $Q(\omega)$, is introduced for each wave type to quantify the effects of attenuation.

$$Q(\omega)^{-1} = -\frac{1}{2\pi}\frac{\Delta E}{E} \tag{2.39}$$

where E is the total stored energy, and $-\Delta E$ is energy loss per cycle (period) of a sinusoidal deformation. A high Q value indicates low attenuation, and a low Q value indicates high energy loss (Aki and Richards, 2002).

In the viscoelastic model, the stress–strain relationship given in Eq. 2.12 involves replacing the elasticity tensor C_{ijkl} with time- and frequency-dependent moduli $M(t)$ and $\bar{M}(\omega)$, respectively:

$$p(t) = M(t) * \varepsilon(t), \quad \text{time domain} \tag{2.40}$$

$$\bar{p}(\omega) = \bar{M}(\omega)\bar{\varepsilon}(\omega), \quad \text{frequency domain} \tag{2.41}$$

Here, $\bar{M}(\omega) \in \mathbb{C}$, and the symbol $(*)$ denotes convolution in the time domain.

The stress–strain relation in the time domain can be written as

$$p(t) \equiv \sigma(t) = M(t)\varepsilon(t) = \dot{\Upsilon}(t)\varepsilon(t), \tag{2.42}$$

where the modulus $M(t) \in \mathbb{R}$ is interpreted as the stress impulse response function of the viscoelastic medium, and $\Upsilon(t)$ is referred to as the stress relaxation function.

The relationship between the modulus $M(t)$ and the stress relaxation function $\Upsilon(t)$ is given by

$$M(t) = \dot{\Upsilon}(t). \tag{2.43}$$

To compute $M(t)$ or $\Upsilon(t)$, a mathematical model is required that reproduces the observed behavior, particularly the frequency-dependent quality factor $Q(\omega)$. The most widely used model is the Generalized Standard Linear Solid (GSLS) model (Liu et al., 1976).

The GSLS model consists of a superposition of rheological (Maxwell) bodies arranged in parallel (springs k_l and dashpots η_l) and a Hooke spring k_0 (see Fig. 2.5).

The stress relaxation function $\Upsilon(t)$ of the GSLS is determined via a relaxation experiment in which a step strain is applied:

$$\epsilon(t) = \epsilon_0 H(t), \tag{2.44}$$

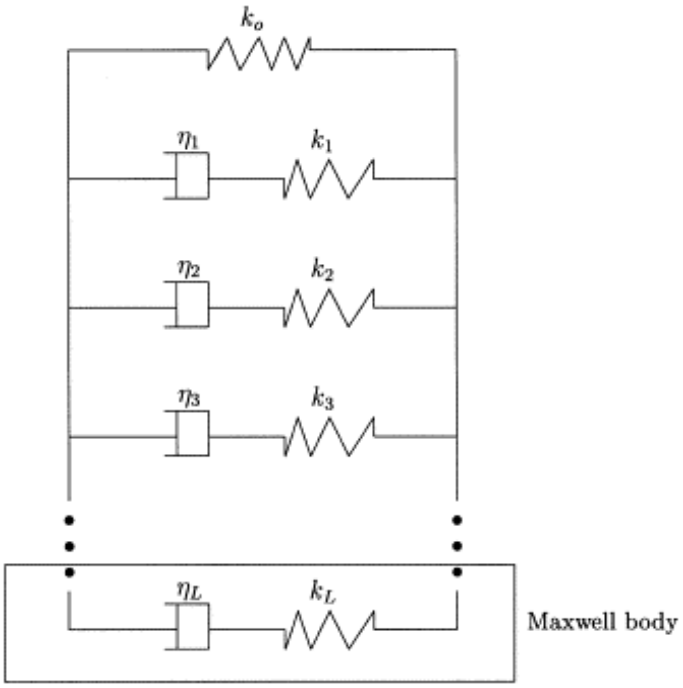


Figure 2.5: *Schematic diagram of generalized standard linear solid (GSLS) composed of L so-called relaxation mechanisms or Maxwell bodies. k_l and η_l ($l = 1, \dots L$) represent elastic moduli and Newtonian viscosities, respectively (Bohlen, 2002).*

and the resulting stress relaxation is given by

$$\sigma(t) = \epsilon_0 \Upsilon(t). \tag{2.45}$$

The stress–strain relation in each Maxwell body is

$$\frac{\dot{\sigma}_l}{k_l} + \frac{\sigma_l}{\eta_l} = \dot{\epsilon}_l, \quad l = 1, \dots, L \tag{2.46}$$

and for the single Hookean body:

$$\sigma_0 = k_0 \epsilon_0. \tag{2.47}$$

Since the strain is identical in all components:

$$\epsilon := \epsilon_0 = \epsilon_1 = \cdots = \epsilon_L \tag{2.48}$$

The total stress is obtained by summing the individual stresses:

$$\sigma = \sum_{l=0}^{L} \sigma_l. \tag{2.49}$$

Zener (1948) introduces new variables and formulations that are defined by

- $\tau_{\sigma l}$: Stress relaxation time of the l-th mechanism,

- $\tau_{\epsilon l}$: Strain retardation time of the l-th mechanism,

- $M_R = \lim_{t\to\infty} M(t)$: Relaxed modulus.

These are related to the viscosities η_l and spring moduli k_l as follows:

$$\tau_{\sigma l} = \frac{\eta_l}{k_l} \tag{2.50}$$

$$\tau_{\epsilon l} = \frac{\eta_l}{k_0} + \frac{\eta_l}{k_l} \tag{2.51}$$

$$M_R = k_0 \tag{2.52}$$

Each relaxation process can be expressed in terms of the GSLS stress relaxation function in the time domain (Bai and Tsvankin, 2016).

$$\Upsilon(t) = M_R \left\{ 1 + \sum_{l=1}^{L} \left(\frac{\tau_{\epsilon l}}{\tau_{\sigma l}} - 1 \right) e^{-t/\tau_{\sigma l}} \right\} H(t) \tag{2.53}$$

The Heaviside function is represented by $H(t)$, and the number of relaxation mechanisms is denoted by L.

Using Eq. 2.53, the complex modulus of the GSLS in the frequency domain is given by

$$\overline{M}(\omega) = M_r + iM_i = i\omega\overline{\Upsilon}(\omega) = M_R \left\{ 1 - L + \sum_{l=1}^{L} \frac{1 + i\omega\tau_{\epsilon l}}{1 + i\omega\tau_{\sigma l}} \right\}. \tag{2.54}$$

The quality factor $Q(\omega)$ is then given by

$$Q(\omega) = \frac{M_r}{M_i} = \frac{1 - L + \sum_{l=1}^{L} \frac{1+\omega^2\tau_{\epsilon l}\tau_{\sigma l}}{1+\omega^2\tau_{\sigma l}^2}}{\sum_{l=1}^{L} \frac{\omega(\tau_{\epsilon l} - \tau_{\sigma l})}{1+\omega^2\tau_{\sigma l}^2}}. \tag{2.55}$$

The dispersion relationship is expressed as

$$c(\omega) = \sqrt{\frac{M_r}{\varrho}} = \sqrt{\frac{M_R}{\varrho} \left(1 - L + \sum_{l=1}^{L} \frac{1 + \omega^2\tau_{\epsilon l}\tau_{\sigma l}}{1 + \omega^2\tau_{\sigma l}^2} \right)}, \quad Q \gg 1 \tag{2.56}$$

To estimate a set of 2L model parameters $(\tau_{\epsilon l}, \tau_{\sigma l})$ that approximates a target function $\tilde{Q}(\omega)$, one minimizes the objective function.

$$J(\tau_{\sigma l}, \tau_{\epsilon l}) := \int_{\omega_1}^{\omega_2} \left(Q^{-1}(\omega, \tau_{\sigma l}, \tau_{\epsilon l}) - \tilde{Q}^{-1}(\omega) \right)^2 d\omega = \min \tag{2.57}$$

where $Q(\omega, \tau_{\sigma l}, \tau_{\epsilon l})$ corresponds to the expression in Eq. 2.55.

2.4 Q factor and spectral ratio method

The importance of the quality factor has been well established in various studies, including hydrocarbon exploration, earthquake seismology, and site investigation in engineering. Various methods have been proposed to study and estimate the quality factor; however, its estimation remains associated with significant uncertainty. The spectral ratio method (Båth, 1974) is the most widely employed method. It relies on spectral amplitude ratios at two different distances or between two stations (traces), under the assumption that changes in spectral amplitude result primarily from anelastic attenuation, rather than from scattering or geometric spreading effects.

The amplitude spectrum of a seismic wave at a station, denoted as $|A(\omega)|$, is expressed as

$$|A(\omega)| = |A_0(\omega)| \exp\left(-\frac{\omega}{2}\int \frac{dx}{Q(x)c(x)}\right) = |A_0(\omega)| \exp\left(-\frac{\omega t}{2Q}\right) \tag{2.58}$$

where $|A_0(\omega)|$ encompasses all contributing factors, including geometrical spreading, the source spectrum function, source radiation pattern, instrumental response, and site effects on surface waves. Here, c denotes velocity, ω is the angular frequency, x is the distance along the propagation path, t represents the travel time, and Q is the average quality factor.

Let $|A_1(\omega)|$ and $|A_2(\omega)|$ represent the amplitude spectra of the same signal recorded at two stations, 1 and 2, respectively. By taking the logarithm of the amplitude ratio, the general expression simplifies to

$$\ln\frac{|A_2(\omega)|}{|A_1(\omega)|} = \ln\frac{|A_{0,2}(\omega)|}{|A_{0,1}(\omega)|} - \frac{\omega(t_2 - t_1)}{2Q} = \ln\frac{|A_{0,2}(\omega)|}{|A_{0,1}(\omega)|} - \frac{\omega(x_2 - x_1)}{2cQ} \tag{2.59}$$

In this context, the term $x_2 - x_1$ represents the travel distance between stations.

Eq. 2.59 is applicable to scenarios involving only two stations. When the first term on the right-hand side is constant, the expression $\ln|A_2(\omega)|/|A_1(\omega)|$ can be plotted against ω, yielding a linear relationship. Therefore, Q can be estimated from the linear (negative) slope m of the logarithmic amplitude ratio between the two stations (Tonn, 1989):

$$Q = -\frac{(x_2 - x_1)}{2cm} \tag{2.60}$$

The spectral ratio method is highly sensitive to noise; thus, a high signal-to-noise ratio is required. Moreover, in near-surface environments characterized by large heterogeneity and rapid velocity variations, the spectral ratio method encounters increased challenges.

Relationship between the quality factor of Rayleigh waves (Q) and body wave quality factors (Q_S, Q_P).

The attenuation factor of Rayleigh waves is related to the quality factors of both P-waves (Q_P) and S-waves (Q_S). In general, when the ratio of shear-wave velocity to compressional-wave velocity (β/α) exceeds 0.4, the attenuation coefficient exhibits a significant dependence on Q_P, indicating that Q_P cannot be neglected. In all other cases, the attenuation of Rayleigh waves—and thus Q—depends solely on Q_S.

Empirical relationships often assume that, at shallow depths where shear deformation dominates, $Q_S \approx Q$. In many near-surface materials, it was typically observed that $Q_P \approx 2Q_S$ (Xia, Miller, C. Park, and Tian, 2002).

Analytical solution of acoustic seismic wave with constant Q

To examine and validate the spectral ratio method, the method is applied to an analytical shot gather. The shot gather was generated using the 3D analytical solution of the inhomogeneous acoustic wave equation, given by

$$\left[\Delta - \frac{1}{c^2}\frac{\partial^2}{\partial t^2}\right] p(x, x_s, t) = -4\pi f(x_s, t) \tag{2.61}$$

where x_s denotes the location of the source, and x represents the point at which the pressure p is calculated, produced by an external force source f located at x_s.

The solution to this equation is the Green's function $G(x, x_s, t)$:

$$\left[\Delta - \frac{1}{c^2}\frac{\partial^2}{\partial t^2}\right] G(x, x_s, t) = -4\pi\delta(x - x_s)\delta(t) \tag{2.62}$$

where δ is the Dirac delta function.

Applying the Fourier transform to this equation yields the Helmholtz equation in the frequency domain:

$$\left[k^2 + \Delta\right] \hat{G}(x, x_s, \omega) = -4\pi\delta(x - x_s) \tag{2.63}$$

where the wavenumber k is defined as $k = \frac{\omega}{c}$.

The 3D solution to the Helmholtz equation is given by

$$\hat{G}_{3D}(x, x_s, \omega) = \frac{e^{-ikr}}{r} \tag{2.64}$$

where $r = \|x - x_s\|$ is the distance between the source and the observation point.

Thus, the solution to equation (2.61) in the frequency domain can be expressed through convolution as

$$\hat{p}_{3D}(x, 0, \omega) = \hat{G}_{3D}(x, 0, \omega)\hat{f}(\omega) \tag{2.65}$$

where $\hat{f}(\omega)$ is the Fourier transform of the source function.

To investigate wave propagation in a constant-Q material, the solution to the wave equation must be multiplied by an attenuation factor $e^{-\zeta x}$, following Kjartansson's model (Kjartansson, 1979), where ζ is the attenuation coefficient given by

$$\zeta = \tan\left(\frac{\pi\Gamma}{2}\right)\mathrm{sgn}(\omega)\frac{\omega}{c} \tag{2.66}$$

and Γ is expressed in terms of the quality factor Q

$$\Gamma = \frac{1}{\pi} \tan^{-1}\left(\frac{1}{Q}\right) \approx \frac{1}{\pi Q} \tag{22}$$

The phase velocity c varies with frequency according to

$$c = c_0 \left|\frac{\omega}{\omega_0}\right|^{\Gamma} \tag{2.67}$$

where c_0 is the phase velocity at an arbitrary reference frequency ω_0.

Consequently, the 3D analytical solution (2.65) of the inhomogeneous acoustic wave equation (2.61) in the frequency domain, considering constant Q attenuation, becomes

$$\hat{p}_{3D}(x, 0, \omega) = e^{-\zeta x} \frac{e^{-ikr}}{r} \hat{f}(\omega) \tag{2.68}$$

Applying the inverse Fourier transform yields the solution in the time domain.

Chapter 3

MASWaves software - applications and workflow

This chapter introduces the multichannel analysis of surface waves (MASW) method. The method consists of three principal steps: field acquisition, dispersion imaging, and inversion analysis. The theoretical background of the software package used, `MASWaves`, is explained.

It is important here to distinguish between the shear velocity, denoted by β, and the shear-wave velocity profile, denoted by V_S.

3.1 Overview of the multichannel analysis of surface waves (MASW)

The importance of shear-wave velocity in the shallow subsurface has been recognized across a wide range of geotechnical applications. The shear modulus, which is directly related to a material's stiffness, represents one of the most critical parameters in engineering geophysics. Seismically, shear-wave velocity (β) serves as its most reliable indicator.

Herrenknecht test site characterization, including the definition and determination of the shear-wave velocity structure, is essential. An initial 1D shear-wave velocity profile will be established at the test site.

Surface waves produced by a vertical source, commonly referred to as ground roll (Rayleigh wave), are characterized by high energy and account for more than two-thirds of the total seismic land energy. These waves tend to dominate seismic surveys and are particularly sensitive to shear velocity. A key feature of surface waves is their dispersive nature, meaning that waves with different wavelengths propagate at varying depths and therefore exhibit different velocities. The dispersion characteristics of surface waves can thus be utilized to derive the near-surface shear velocity profile (V_S).

The first method employed in the early 1980s to construct the shear-wave velocity profile of the near surface using the dispersion characteristics of surface waves (Rayleigh waves) was the Spectral Analysis of Surface Waves (SASW), introduced by Nazarian et al. (1983). An impact source (sledgehammer) was applied to the surface, and two receivers were placed at predetermined distances from the source. The method was repeated multiple times with varying distances between the source and the receivers to investigate specific target depths. The acquired data were analyzed in the frequency domain to generate a dispersion curve by calculating the phase differences between successive receiver deployments (Xia,

Miller, and C. Park, 1999). This approach was time-consuming in both data acquisition and processing.

The second method employed in this work is the Multichannel Analysis of Surface Waves (MASW), developed at the Kansas Geological Survey (KGS) (Xia, Miller, and C. Park, 1999). The MASW method is mainly comprised of three steps: multichannel field measurements, dispersion analysis, and inversion analysis. Two main types of MASW are distinguished based on the source used. The first type, active MASW, utilizes an active source at the surface, such as a sledgehammer, to analyze the dispersion of surface waves with slightly high frequency. The acquisition typically consists of 24 or more geophones spread over distances ranging from a few meters to hundreds of meters. The investigation depth for this method is generally shallower than 30 meters. The second type, passive MASW, employs low-frequency sources such as tidal motion and cultural noise to target lower-frequency waves with greater penetration depth; consequently, the investigation depth is increased to more than 30 meters.

The main advantages of MASW, as compared to the SASW method, are regarded as including a more efficient data-acquisition routine in the field, data-processing procedures that are faster and less labor-intensive, and the improved identification and elimination of noise from recorded data.

3.2 MASWaves software - workflow

`MASWaves` is an open-source software package that is used for processing and analyzing multichannel surface wave records by applying the MASW method. The software was developed at the Faculty of Civil and Environmental Engineering, University of Iceland. It is written in MATLAB® *MASWaves User Manual* (2017) and consists of two primary parts:

- `MASWaves Dispersion:` A dispersion analysis tool for surface wave data.
- `MASWaves Inversion:` An inversion analysis tool for estimating shear-wave velocity V_S profiles.

The accuracy of the software in both types of analysis was validated by the developer through comparisons with existing software and theoretical models. The performance of the `MASWaves Dispersion` tool was benchmarked against the `Geopsy` software package. Dispersion curves extracted from both software tools exhibited excellent agreement. The `MASWaves Inversion` tool was verified by comparing its results with those obtained using the `WinSASW` software, as well as with theoretical dispersion curves reported in the literature (Olafsdottir et al., 2018). These comparisons confirmed the precision of the software and its ability to differentiate between fundamental- and higher-mode experimental dispersion curves. Additional field tests, conducted at a site in Iceland, demonstrated strong agreement between MASW-derived dispersion curves and those obtained through SASW.

3.2.1 Field acquisition

The 1D active MASW acquisition is conducted by deploying 24 low-frequency vertical geophones or more in a linear array on the ground, with uniform spacing (dx) and receiver spread length (L). An impulsive source (e.g., a sledgehammer) is positioned at a source offset (x_1), which denotes the distance from the source to the first geophone, as shown in Fig. 3.2 on page 22. The Rayleigh wave dispersion curve, derived from the recorded data, is inverted to estimate the 1D shear-wave velocity V_S profile; this profile characterizes the subsurface materials directly beneath the midpoint of the geophone spread. For 2D

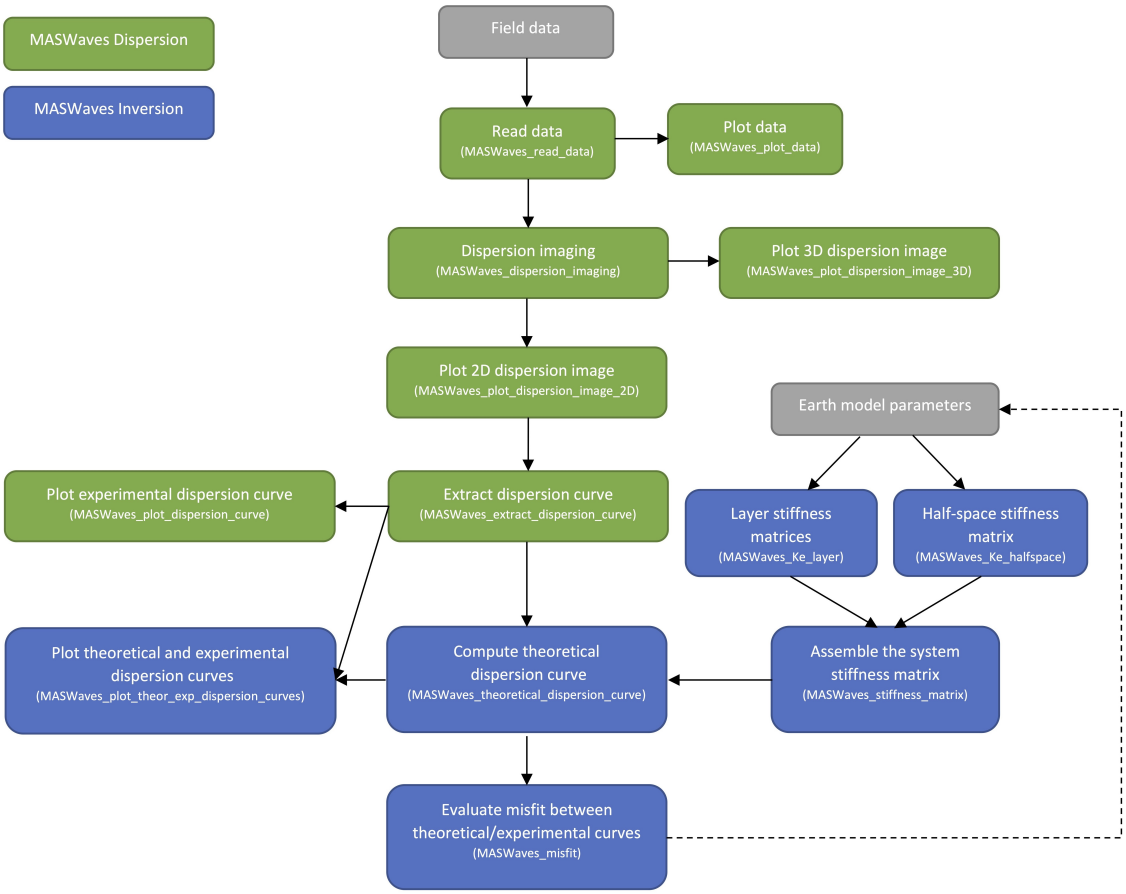


Figure 3.1: *Overview of MASWaves (*MASWaves User Manual *2017).*

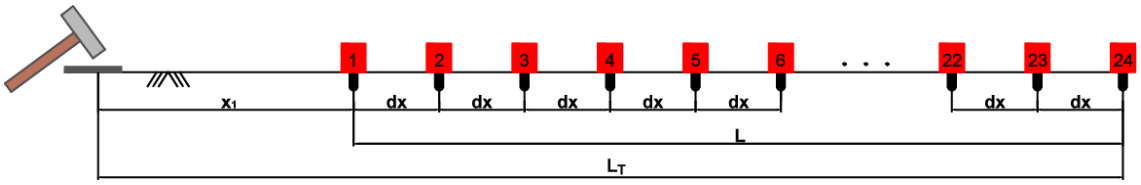


Figure 3.2: *Example of a MASW measurement profile. A line-up of $N = 24$ geophones with equal spacing dx is shown. The source offset is denoted as x_1. The length of the receiver spread is L, and the total length of the measurement profile is L_T (Olafsdottir et al., 2018).*

imaging, the acquisition setup—comprising the geophone spread and source offset—is shifted laterally at regular intervals. Each 1D V_S profile obtained from individual records is interpolated to generate a 2D shear-wave velocity map. This approach allows the identification of lateral variations in subsurface properties (Xia, Miller, C. Park, and Ivanov, 2000).

The configuration parameters of MASW acquisition—namely, the source offset x_1, receiver spread length L, and receiver spacing dx—are considered critical in determining the resolution of dispersion imaging, as well as the minimum and maximum investigation depths. An empirical criterion that is widely adopted states that the maximum observable wavelength ($\lambda_{\max}$) during data acquisition is approximately equal to the receiver spread length L (C. Park and Carnevale, 2010):

$$\lambda_{\max} \approx L \tag{3.1}$$

The maximum investigation depth ($Z_{\max}$) is defined by the longest observable wavelength and is given as half of $\lambda_{\max}$:

$$Z_{\max} = 0.5\lambda_{\max} = \frac{L}{2} \tag{3.2}$$

The optimum source offset distance x_1 to avoid the near-field effect is established when the offset equals half the wavelength and is therefore expressed as

$$x_1 = \frac{L}{2} \quad \text{when} \quad \lambda_{\max} \approx L \tag{3.3}$$

The minimum investigation depth—or the minimum resolvable thickness (H_1) of the uppermost layer— is governed by the highest measurable frequency ($f_{\max}$) and the corresponding phase-velocity ($c_{\min}$) (Stokoe et al., 1994):

$$H_1 \geq 0.5\lambda_{\min} = 0.5\frac{c_{\min}}{f_{\max}} \tag{3.4}$$

A smaller receiver spacing, dx, allows for more accurate measurement of shorter wavelengths, $\lambda_{\min}$, without spatial aliasing—a phenomenon characterized by the distortion or misrepresentation of wavefield signals due to insufficient spatial sampling of the seismic wavefield. This relationship is governed by the Nyquist criterion ($dx \leq \frac{\lambda_{\min}}{2}$) (Xia, Miller, C. Park, and Ivanov, 2000), which states that the minimum resolvable wavelength, $\lambda_{\min}$, decreases proportionally as dx is reduced.

$$H_1 \geq H_{\min} \approx dx \tag{3.5}$$

Therefore, although H_1 is not directly determined by dx, the shortest wavelength that can be reliably measured is influenced by the choice of dx; in turn, this affects the minimum thickness of the uppermost layer, H_1, that can be resolved.

Surface-wave propagation is significantly affected by topographic conditions. Optimal surface-wave generation is achieved over flat ground extending at least one receiver-spread length, L. Minor topographic variations along the entire survey line are typically considered negligible; however, surface relief exceeding approximately 10% of L will substantially hinder surface-wave generation Fig. 3.3.

In this thesis, a modified procedure for MASW acquisition and 1D V_S profiling is adopted. Instead of using a single record with a fixed source offset x_1, the procedure acquires multiple records with varying source offsets along a stationary geophone spread. For each record, the dispersion curve is extracted and inverted to obtain a 1D V_S profile. The final subsurface model is derived from the median of all profiles.

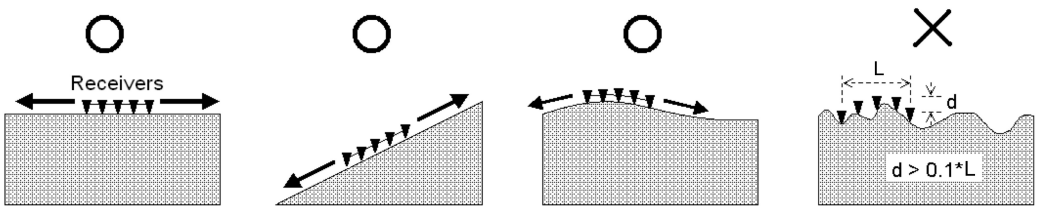


Figure 3.3: *Effect of topography on surface-wave generation and the quality of MASW data. O denote correct acquisition, while X indicate incorrect one (C. B. Park and Adkins-Heljeson, 2006).*

3.2.2 Dispersion analysis

Thec software employs the phase shift method (C. Park, 1998) to transform multichannel surface wave records into phase-velocity spectra. This method visualizes the dispersion properties of different surface wave modes (e.g., fundamental/higher modes) through their frequency content and characteristic phase velocities. The dispersion analysis workflow consists of four main steps (Fig. 3.4 on the following page):

1. Import data and determine the testing range for Rayleigh wave velocity.
2. Fourier transformation and amplitude normalization.
3. Dispersion imaging.
4. Extraction of dispersion curves.

Step 1: Import data and determine the testing range for Rayleigh wave velocity.

Initially, the multichannel recorded data $u(x,t)$ are imported, and the testing range for the phase velocities of Rayleigh waves is determined.

$$c_{\mathrm{T,min}} \leq c_{\mathrm{T}} \leq c_{\mathrm{T,max}} \tag{3.6}$$

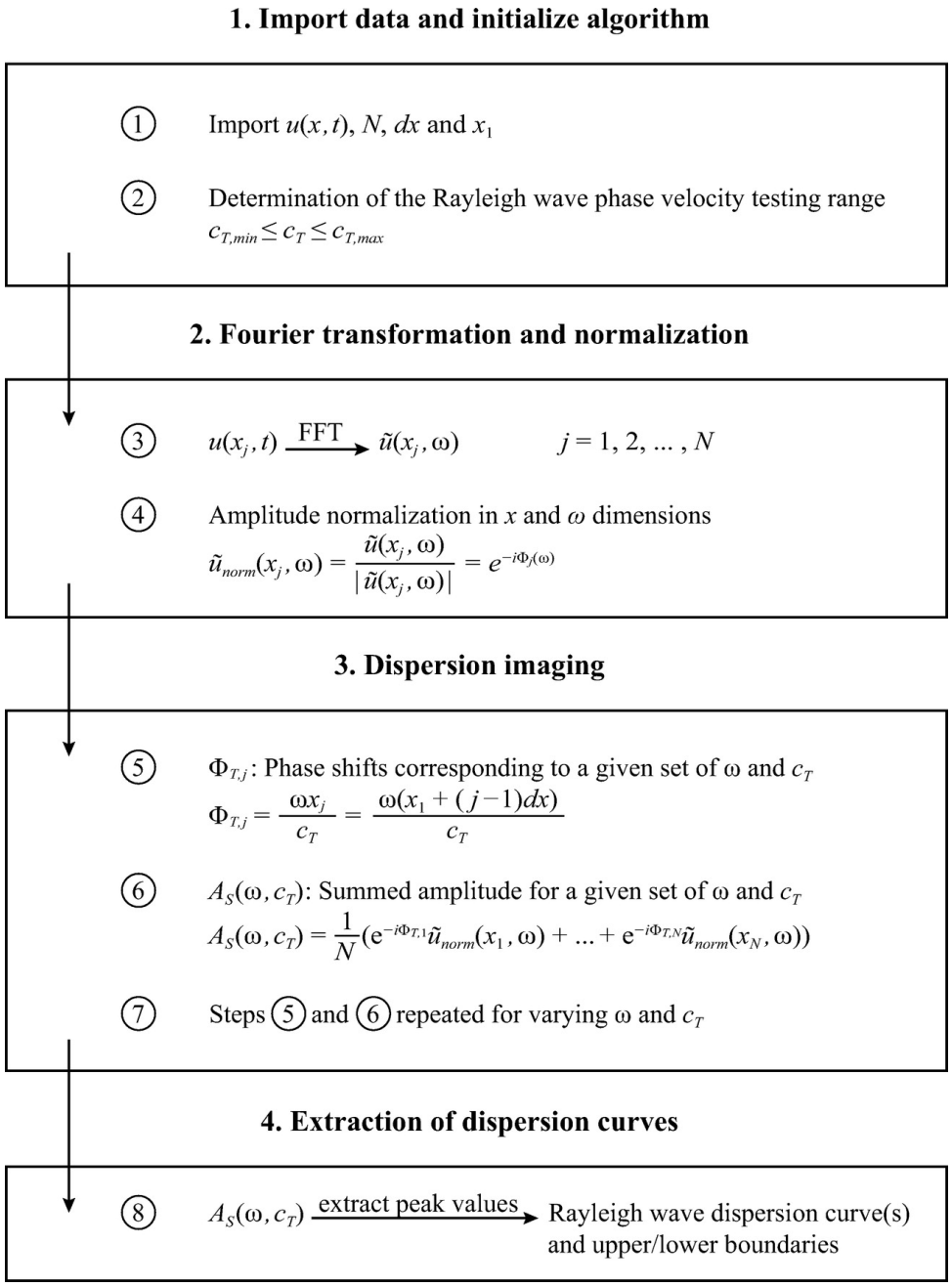


Figure 3.4: *Overview of the dispersion analysis (Olafsdottir et al., 2018).*

Step 2: Fourier transformation and amplitude normalization

The recorded wave field $u(x,t)$ is transformed into the frequency domain representation $\tilde{u}(x,\omega)$, where ω denotes the angular frequency.

$$\tilde{u}(x,\omega) = \int_{-\infty}^{\infty} u(x,t)e^{-i\omega t}\,dt \tag{3.7}$$

in which the discrete Fourier transform is applied.

For an N-channel surface wave record $u(x_j,t)$ $(j = 1,2,\ldots,N)$, the Fourier transform is applied individually to each trace, so that the data are decomposed into their respective frequency components, $\tilde{u}(x_j,\omega)$ $(j = 1,2,\ldots,N)$.

The transformed wavefield is expressed as:

$$\tilde{u}(x_j,\omega) = A_j(\omega)P_j(\omega), \quad j = 1,2,\ldots,N$$

where:

- $A_j(\omega)$: amplitude term (incorporates attenuation and geometric spreading effects),
- $P_j(\omega)$: phase term (encodes the dispersion properties).

The phase term is related to the characteristic phase-velocity $c(\omega)$ of the frequency component ω as follows:

$$P_j(\omega) = e^{-i\Phi(\omega)x_j} \tag{3.8}$$

with

$$\Phi(\omega) = \frac{\omega}{c(\omega)} \tag{3.9}$$

Substituting Eq. 3.9 in Eq. 3.8 yields:

$$P_j(\omega) = e^{-i\frac{\omega x_j}{c(\omega)}} \tag{3.10}$$

To isolate the dispersion properties, the transformed wavefield $\tilde{u}(x_j,\omega)$ is normalized.

$$\tilde{u}_{\text{norm}}(x_j,\omega) = \frac{\tilde{u}(x_j,\omega)}{|\tilde{u}(x_j,\omega)|} = e^{-i\frac{\omega x_j}{c(\omega)}} \tag{3.11}$$

thereby removing geometric spreading and attenuation effects while preserving information related to phase-velocity.

Step 3: Dispersion imaging

The imaging process is based on slant-stacking, in which amplitudes are summed along slanted paths in the offset domain. The slant-stack function $\tilde{S}(\omega,c_T)$ is defined as follows:

$$\tilde{S}(\omega,c_T) = \int_{x_1}^{x_N} e^{-i\Phi_T x}\frac{\tilde{u}(x,\omega)}{|\tilde{u}(x,\omega)|}\,dx = \int_{x_1}^{x_N} e^{-i\Phi_T x}\tilde{u}_{norm}(x,\omega)\,dx \tag{3.12}$$

To determine the dispersion characteristics of $u(x,t)$, the function $\tilde{S}(\omega,c_T)$ is analyzed. Maxima are observed in $\tilde{S}(\omega,c_T)$ when the testing phase-velocity c_T matches the actual phase-velocity $c(\omega)$ at a given frequency. These dispersion characteristics are visualized by tracing the maxima across various frequency values ω.

Within a specified phase-velocity range (Eq. 3.6 on page 23), the testing velocity c_T is varied incrementally. For each frequency ω, the slant-stack function is computed numerically and examined for maxima:

$$\tilde{S}_s(\omega, c_T) = \sum_{j=1}^{N} e^{-i\Phi_T x_j} \; \tilde{u}_{j,norm}(\omega) = \sum_{j=1}^{N} e^{-i\Phi_T x_j} P_j(\omega) \tag{3.13}$$

where

$$\Phi_T = \frac{\omega}{c_T} \tag{3.14}$$

Maxima in $\tilde{S}(\omega, c_T)$ are found when

$$\Phi_T = \Phi(\omega) \tag{3.15}$$

By combining Equations (3.9), (3.14), and (3.15), the following relation is obtained:

$$\frac{\omega}{c_T} = \frac{\omega}{c(\omega)} \quad \Rightarrow \quad c_T = c(\omega) \tag{3.16}$$

The values of $\tilde{S}_s(\omega, c_T)$ are complex, and their absolute value are given by:

$$A_s(\omega, c_T) = \left| \tilde{S}_s(\omega, c_T) \right|$$

This quantity represents the slant-stacked amplitude associated with the testing phase-velocity c_T and frequency ω.

To ensure comparability across all cases, the amplitude A_s is normalized:

$$A_{s,norm}(\omega, c_T) = \frac{A_s(\omega, c_T)}{N} \tag{3.17}$$

The two-dimensional phase-velocity spectrum, or dispersion image, is then obtained by plotting the normalized summed amplitude values $A_{s,norm}$ in the frequency–phase-velocity domain. Peaks in this amplitude spectrum correspond to the dispersion characteristics of the recorded surface waves.

Step 4: Extraction of dispersion curves

Following the computation of the phase-velocity spectrum, the experimental dispersion curve is extracted using a semi-automated picking tool integrated into the software employed in this study. This tool detects the maximum amplitude within a defined frequency range that meets or exceeds the natural frequency of the geophone utilized.

The detected points are visualized, and the fundamental mode is determined via visual inspection. Points corresponding to the fundamental mode are then manually selected by the analyst. The analyst repeats this process when higher-order modes are present. Additionally, the analyst may manually include further points by interacting directly with the dispersion image, as necessary.

Inaccurate identification of the fundamental mode may result in significant errors in the inverted shear-wave velocity profile.

3.2.3 Inversion analysis

The inversion analysis is performed to obtain a shear-wave velocity profile by back-calculating the experimental dispersion curve using Rayleigh wave propagation theory. A plane-layered elastic Earth model is assumed for this process. The theoretical dispersion curve is computed based on the model parameters, which are iteratively adjusted to minimize the difference between the theoretical and experimental dispersion curves.

Key components of the inversion analysis are as follows:

1. Estimation of initial model parameters.
2. Compute theoretical dispersion curves using a mathematical model (stiffness matrix method).
3. Error estimation and misfit minimization between theoretical and experimental dispersion curves.

Step 1: Estimation of initial model parameters.

The initial model parameters required for inversion are estimated under the assumption of an n-plane-layered Earth model, in which each layer is assumed to be homogeneous linear elastic. Each layer, indexed by layer number, is characterized by its thickness (h), shear-wave velocity (β), compressional-wave velocity (α), and mass density (ρ) (see Fig. 3.5). The estimation process is informed by prior knowledge of the site. As the fundamental mode is relatively less sensitive to both compressional-wave velocity and mass density, these parameters are held constant throughout the inversion.

Step 2: Compute theoretical dispersion curves.

The Rayleigh secular equation is a fundamental relation used to compute theoretical dispersion curves. For a plane-layered medium with homogeneous, linear elastic layers (see Fig. 3.5), it is expressed as:

$$F_{R,q}(k_q, c_q, \boldsymbol{\beta}, \boldsymbol{\alpha}, \boldsymbol{\rho}, \boldsymbol{h}) = 0, \quad q = 1, \ldots, Q \tag{3.18}$$

where:

- Q: Number of points at which the theoretical dispersion curve is evaluated.
- n: Number of layers, with the $(n+1)$-th layer representing the half-space.
- f_q, ω_q: Frequency and angular frequency at point q.
- c_q: Rayleigh wave phase-velocity at frequency f_q.
- k_q: Wave number at f_q, given by $k_q = \dfrac{2\pi f_q}{c_q} = \dfrac{\omega_q}{c_q}$.
- $\boldsymbol{\beta}, \boldsymbol{\alpha}, \boldsymbol{\rho}, \boldsymbol{h}$: Shear-velocity, compressional-velocity, mass density, and layer thickness vectors, respectively.

The equation is typically solved using stiffness matrix methods. The element stiffness matrix of a distinct layer relates the stresses at the upper and lower interfaces of the layer to the corresponding displacements. For each layer, including the half-space, the corresponding element stiffness matrix is derived and expressed as:

$$\mathbf{p}_{e,i} = \mathbf{k}_{e,i}\mathbf{u}_{e,i} \tag{3.19}$$

Here, $\mathbf{k}_{e,i}$ denotes the element stiffness matrix of the i-th layer; $\mathbf{u}_{e,i}$ represents the element displacement vector; and $\mathbf{p}_{e,i}$ is the element external load vector applied at the upper and

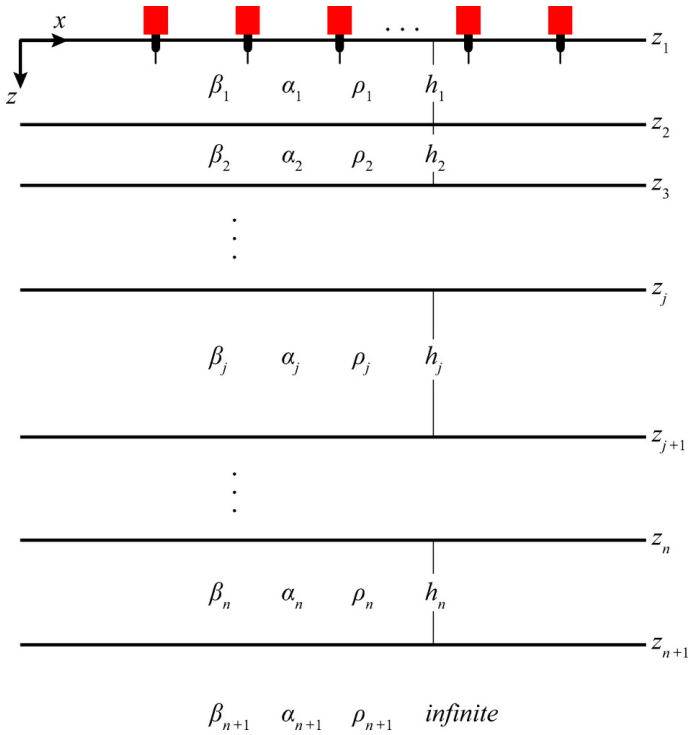


Figure 3.5: *Layered Earth model used for inversion analysis (Olafsdottir et al., 2018).*

lower boundaries of finite layers ($i = 1, \ldots, n$).

The element matrices are assembled to construct the global system matrix:

$$\mathbf{P} = \mathbf{K}\mathbf{u} \tag{3.20}$$

where $\mathbf{K}$ represents the system stiffness matrix of the layered Earth model, and $\mathbf{P}$ and $\mathbf{u}$ denote the system force and displacement vectors, respectively.

The computation of the theoretical dispersion curve involves determining phase velocities $c_{t,q}$ for a set of wavelengths $\lambda_{t,q}$, using the stiffness matrix method. This process is iterative and matches wavelengths present in the experimental dispersion curve. For each point $q = 1, \ldots, Q$:

$$\lambda_{t,q} = \lambda_{e,q} \tag{3.21}$$

where $\lambda_{t,q}$ and $\lambda_{e,q}$ are the theoretical and experimental wavelengths at point q, respectively. The corresponding wave number is computed as:

$$k_{t,q} = \frac{2\pi}{\lambda_{t,q}} \quad \text{for } q = 1, \ldots, Q \tag{3.22}$$

Given an assumed test phase-velocity c_T and the calculated wave number $k_{t,q}$, the element stiffness matrix $\mathbf{K}_{e,i}$ is constructed for each layer $i = 1, \ldots, n+1$, including the half-space.

For finite layers ($i = 1, \ldots, n$):

$$\mathbf{K}_{e,i} = \begin{bmatrix} \kappa_{11,i} & \kappa_{12,i} & \kappa_{13,i} & \kappa_{14,i} \\ \kappa_{21,i} & \kappa_{22,i} & \kappa_{23,i} & \kappa_{24,i} \\ \kappa_{31,i} & \kappa_{32,i} & \kappa_{33,i} & \kappa_{34,i} \\ \kappa_{41,i} & \kappa_{42,i} & \kappa_{43,i} & \kappa_{44,i} \end{bmatrix} \tag{3.23}$$

For the half-space ($i = n + 1$):

$$\mathbf{K}_{e,n+1} = \begin{bmatrix} \kappa_{11,n+1} & \kappa_{12,n+1} \\ \kappa_{21,n+1} & \kappa_{22,n+1} \end{bmatrix} \tag{3.24}$$

These element stiffness matrices $\mathbf{K}_{e,i}$ are assembled into the global system stiffness matrix $\mathbf{K}$ as follows:

$$\mathbf{K} = \begin{bmatrix} \boldsymbol{K}_{11,1} & \boldsymbol{K}_{12,1} & & & & & \\ \boldsymbol{K}_{21,1} & \boldsymbol{K}_{22,1} + \boldsymbol{K}_{11,2} & \boldsymbol{K}_{12,2} & & & & \\ & \boldsymbol{K}_{21,2} & \boldsymbol{K}_{22,2} + \boldsymbol{K}_{11,3} & \boldsymbol{K}_{12,3} & & & \\ & & \ddots & \ddots & \ddots & & \\ & & & \boldsymbol{K}_{21,n-1} & \boldsymbol{K}_{22,n-1} + \boldsymbol{K}_{11,n} & \boldsymbol{K}_{12,n} & \\ & & & & \boldsymbol{K}_{21,n} & \boldsymbol{K}_{22,n} + \boldsymbol{K}_{e,n+1} & \end{bmatrix} \tag{3.25}$$

The natural modes of Rayleigh wave propagation are obtained by considering a system with no external loads, such that:

$$\mathbf{K}\mathbf{u} = 0 \tag{3.26}$$

For nontrivial solutions, the determinant of the global stiffness matrix must vanish. Modal solutions at various frequencies are therefore found by solving:

$$F_R(c, k) = \det(\mathbf{K}) = 0 \tag{3.27}$$

To solve the dispersion equation for a given wave number $k_{t,q}$, a test phase-velocity c_T is incrementally adjusted within the bounds $c_{T,min} \leq c_T \leq c_{T,max}$. A sign change in $\det(\mathbf{K})$ indicates the bracketing of the fundamental mode velocity, which is then refined to the desired accuracy:

$$c_{t,q} = c_T \tag{3.28}$$

By repeating this procedure across the wave numbers $k_{t,q}$ for $q = 1, \ldots, Q$, the complete theoretical dispersion curve is obtained.

Step 3: Error estimation and misfit minimization

The local search algorithm is employed to fit the theoretical and experimental dispersion curves. The initial set of model parameters (Fig. 3.5 on the facing page) is used to compute the theoretical Rayleigh wave phase velocities $c_{t,q}$ for each wavelength $\lambda_{t,q}$. The algorithm includes manual updates—performed by the user—of the shear-wave velocity vectot, $\boldsymbol{\beta} = [\beta_1, \ldots, \beta_{n+1}]^T$, the thickness vector, $\boldsymbol{h} = [h_1, \ldots, h_n]^T$, or both after each iteration, while the remaining parameters are held constant.

The percentage error ϵ, or misfit, is evaluated as

$$\epsilon = \frac{1}{Q} \sum_{q=1}^{Q} \frac{\sqrt{(c_{\mathrm{e},q} - c_{t,q})^2}}{c_{\mathrm{e},q}} \cdot 100 \tag{3.29}$$

Convergence is defined as the condition in which the misfit, ϵ, is reduced to $\epsilon_{\max}$ or lower, or when the discrepancy between the experimental and theoretical dispersion curves is minimized to an acceptably small value. If sufficient agreement is not attained, the shear-wave velocity profile is iteratively updated for each layer.

Local search methods are characterized by a strong dependence on the analyst's expertise. These techniques are implemented through the manual adjustment and optimization of parameters after each iteration; they are particularly sensitive to the initial model estimation and to the identification of local minima within the theoretical–experimental misfit function.

To address these limitations, an optimization solver is employed in this study to reduce the misfit.

3.2.4 Automatic inversion algorithm

The algorithm employed is based on a self-developed strategy, *Adaptive Testing Velocity Step Size Strategy*, which defines the range of testing velocities used to compute the theoretical dispersion curve. This range is selected based on the dispersion image, wherein the minimum and maximum velocities are identified. From this image, four distinct testing velocity steps (c_T) are defined as follows:

$$c_T = [2, 1, 0.1, 0.03]\,\mathrm{m/s} \tag{3.30}$$

The inversion code is structured into four stages (Fig. 3.6). In each stage, a different step size for the testing velocity is applied, beginning with a large step size of 2 m/s and progressively decreasing in subsequent stages. The selection of these step sizes was informed by extensive empirical testing. While larger step sizes accelerate computation and tend to reduce the overall misfit, smaller step sizes yield more accurate results by substantially lowering the misfit value and enhancing resolution. This refinement is particularly advantageous in regions where the experimental dispersion curve displays complex shapes or densely sampled data points, which complicate the misfit minimization process.

The inversion procedure commences with the loading of experimental dispersion data $(c_{e,q}, \lambda_{e,q})$, which had been semi-manually selected. Initial model parameters are defined.

The core inversion loop is carried out using `fminsearch`, a nonlinear optimization solver in which the simplex search algorithm of Nelder and Mead (1965) is implemented to minimize the misfit between theoretical and experimental dispersion curves. The Nelder–Mead method is commonly employed for derivative-free optimization, especially in scenarios where derivatives are unavailable, unreliable, or computationally expensive to compute.

The inversion process is terminated under one of the following conditions:

1. The misfit drops below a predefined threshold.
2. No significant improvement is observed over several iterations.

Upon termination, the procedure advances to the next inversion stage using a finer testing velocity step. The model parameters obtained from the preceding stage are adopted as the

initial model for the subsequent iteration. This iterative process is repeated across all four stages. For each stage, the misfit evolution is documented, and both the theoretical and experimental dispersion curves are plotted. This visualization facilitates the monitoring of the inversion's progress and ensures convergence toward a local minimum.

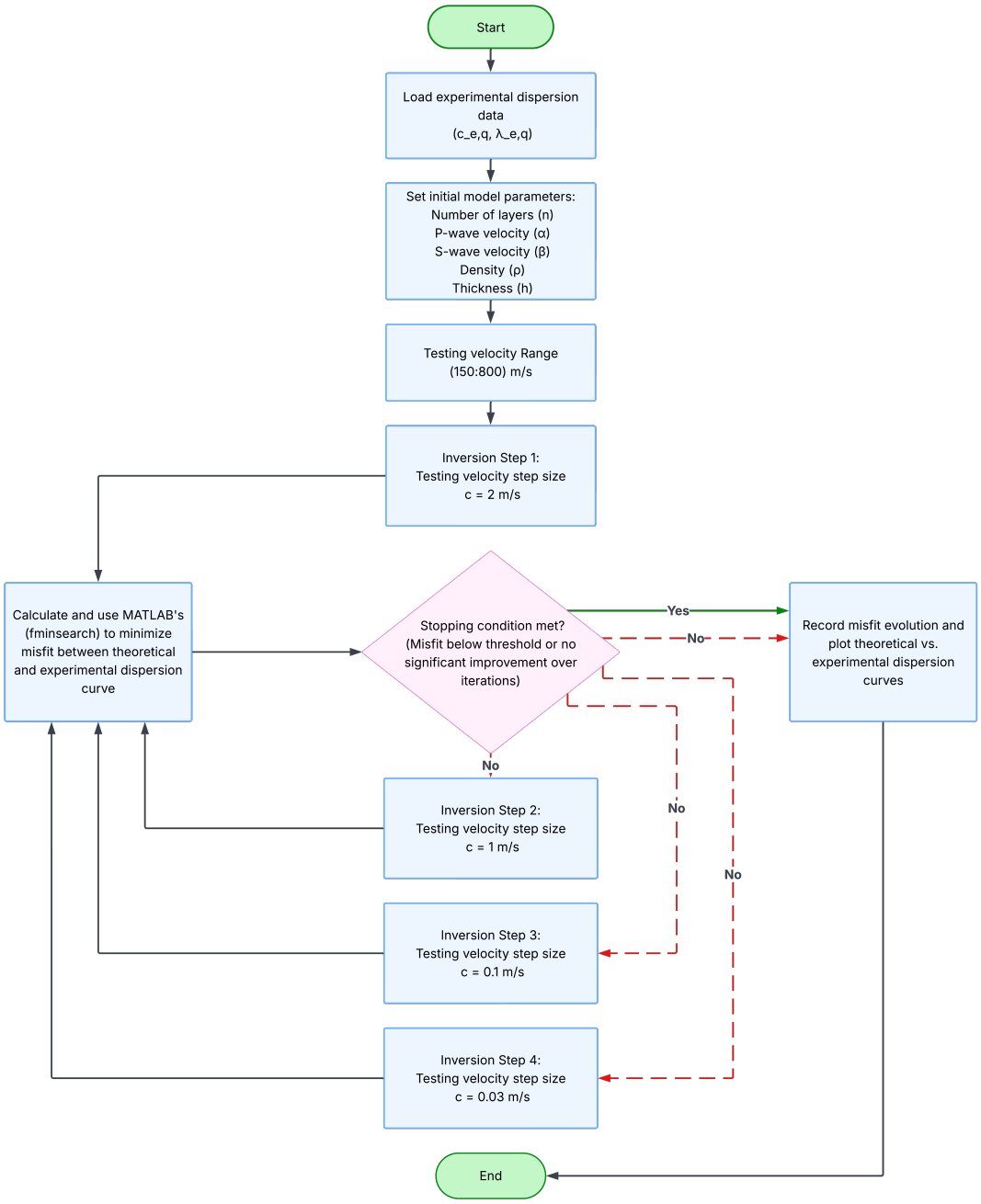


Figure 3.6: *Overview of automatic inversion algorithm.*

Chapter 4

Site description and field acquisition

In this chapter, the Herrenknecht UVT test site is introduced, and a preliminary understanding of its geological structure is presented. The primary geophysical parameter of interest—shear-wave velocity—is examined, and site-specific challenges likely to affect data acquisition and interpretation are identified. The first step of MASW method is outlined, including the design and layout of the field survey. The instruments and equipments employed in the survey are described. Finally, all available information is synthesized to construct an initial model, which is used as a start model for the subsequent inversion process.

4.1 Geological structure and subsurface conditions

The test site was selected from multiple alternatives due to its advantageous proximity to the company premises and its relatively homogeneous subsurface conditions, which, as currently understood, have not yet been disproven. Since the site lies within company-owned land, the presence of anthropogenic fill material in the shallow subsurface layers is anticipated. On the southern side of the test site, a seepage trench has been identified; it is filled with large-sized rock (Fig. 4.5).

Preliminary geological insights were obtained through a 30 cm deep borehole and a side trench excavated at the test site. These observations revealed three distinct layers. The uppermost layer consists of a reddish, gravelly fill (loose gravel) ranging from small to medium grain sizes. Drilling into this layer proved difficult. While the borehole indicated a thickness of approximately 0.1 m, the side trench revealed a thickness of up to 0.3 m. The discrepancy is likely due to excavation effects during trenching.

Beneath the top layer lies a silty sand soil that contains fewer stones than the upper stratum. Based on geotechnical properties determined in the laboratory (Kramer, 1996), the upper layer is expected to exhibit a higher shear-wave velocity than the underlying silty sand unit. However, it is important to note that grain size and confining pressure significantly affect the shear-wave velocity of the gravelly, loose layer. The third layer, identified through visual inspection, consists of a dark brown sandy clay deposit. This layer is denser and is presumed to have a higher shear-wave velocity than the overlying strata. The groundwater table was encountered at a depth of approximately 2 meters.

One notable challenge of MASW method is the accurate resolution of shear-wave velocity in the very shallow upper layer, which ranges in thickness from approximately 10 to 30 cm.

Table 4.1: *Soil stratigraphy and initial shear-wave velocity estimates at the test site*

Depth (m)	Layer	Soil composition	Shear-wave velocity (m/s)
0–0.3	Top	Gravelly soil with small to medium-sized rocks	200–600
0.3–1.1	Middle	Silty sand with a few stones	180–360
1.1–2.0+	Bottom	Sandy clay with fine-grained rocks	250–600



Figure 4.1: *Side trench excavated at the Herrenknecht test site (Photograph by Thomas Hertweck).*



Figure 4.2: *Shallow borehole, approximately 30 cm deep, at the Herrenknecht test site (Photograph by the author).*

4.2 MASW field acquisition and survey design

The objective of this study is to construct a one-dimensional shear-wave velocity model using MASW under the assumption of lateral homogeneity in the subsurface at the test site. For this purpose, a near-surface seismic survey was designed, consisting of two perpendicular MASW profiles (Fig. 4.3). Each profile employed a geophone spread length of $L = 71\,\text{m}$, which defines the maximum observable wavelength as $\lambda_{\max} = 71\,\text{m}$. Based on Eq. 3.2, the corresponding maximum investigation depth is approximately $Z_{\max} \approx 35\,\text{m}$. The investigation aimed to characterize subsurface layers shallower than 30 m.

Each survey line included 72 vertical geophones with a natural frequency of 4.5 Hz and a uniform spacing interval of $dx = 1\,\text{m}$ (Fig. 4.4), yielding a minimum investigation thickness based on Equation 3.5 of 1 m. In the second profile, the presence of the seepage trench resulted in a slight displacement of the geophones. The geophone, originally positioned at 7 meters, underwent a shift to 7.70 meters. The geophone at 8 meters was located directly within the trench, while the subsequent geophone, originally placed at 9 meters, was effectively situated at 10.30 meters, Fig. 4.5. To ensure firm coupling with the ground, especially given the hard surface conditions, pre-drilled holes of 6 cm depth were used to install the geophones securely.

The seismic source employed in this study was a sledgehammer struck against a metal plate, with each impact repeated ten times and subsequently stacked. Sources were activated at regular intervals of 4 m, beginning from an offset of $-1\,\text{m}$ behind the first geophone. The final shot of the first profile, shot 20, was acquired at zero offset directly adjacent to the last geophon. In contrast, the final shot of the second profile, shot 47, had a 4 m source offset from the last geophone. Shots 15 and 16 were repeated at the same position; however, they were treated as two separate shots. A total of 40 shots were acquired—20 along each profile. This study focuses on the shots corresponding to each seismic profile: shots 1 through 20 pertain to the first profile, whereas shots 28 through 47 correspond to the second profile. A summary of the primary parameters related to the field measurements is presented in Table 4.2.

Table 4.2: *Overview of MASW configuration at the Herrenknecht test site.*

Site characteristics	
Location of groundwater table	At 2 m depth
Mass density, ρ (kg/m^3)	1850
Field measurements	
Month/year of MASW field test	06/2024
Number of profiles	2
Number of geophones, N	72
Receiver spacing, dx (m)	1
Number of shots in profile	20
Shot number	First profile (1-20)
	Second profile (28-47)
First Source offset, x_1 (m)	-1
Shot interval, (m)	4
Sampling rate, f_s (Hz)	8000
Recording time, T (s)	0.5

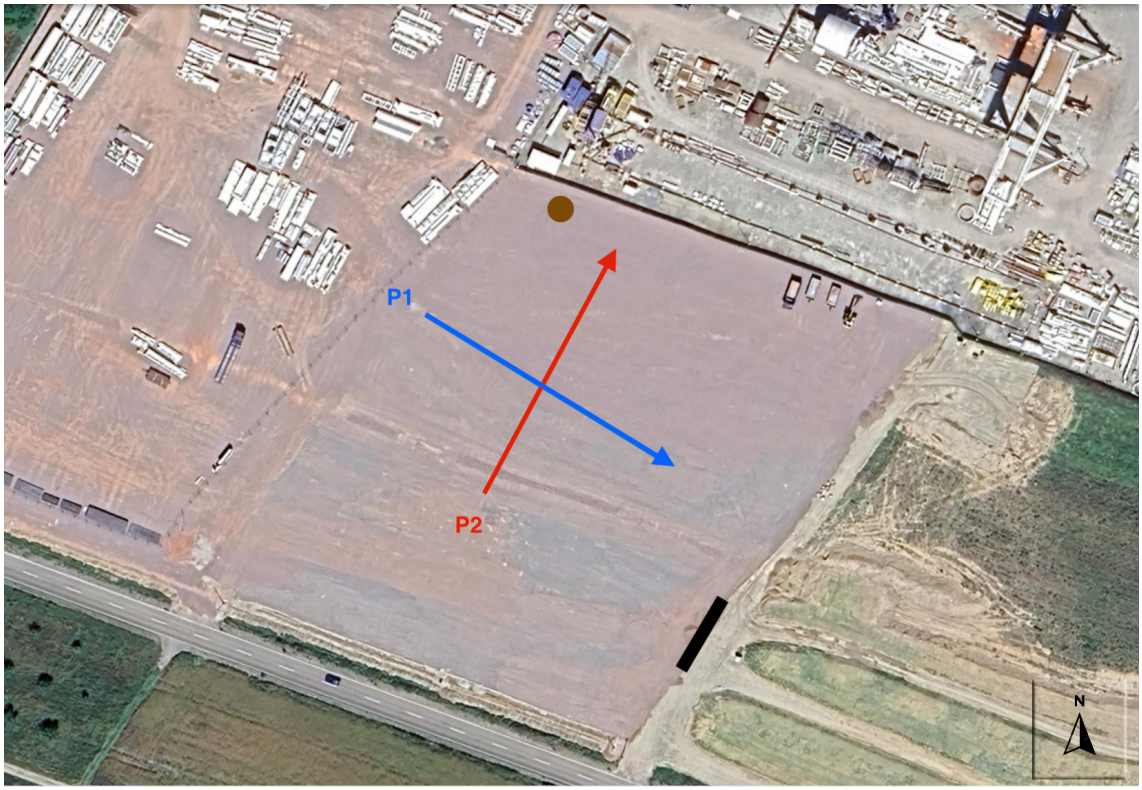


Figure 4.3: *Herrenknecht test site. The blue and red lines indicate the locations and directions of the first and second profiles, respectively. The brown circle marks the location of the shallow borehole, and the black line shows the position of the side trench (source: Google Maps).*

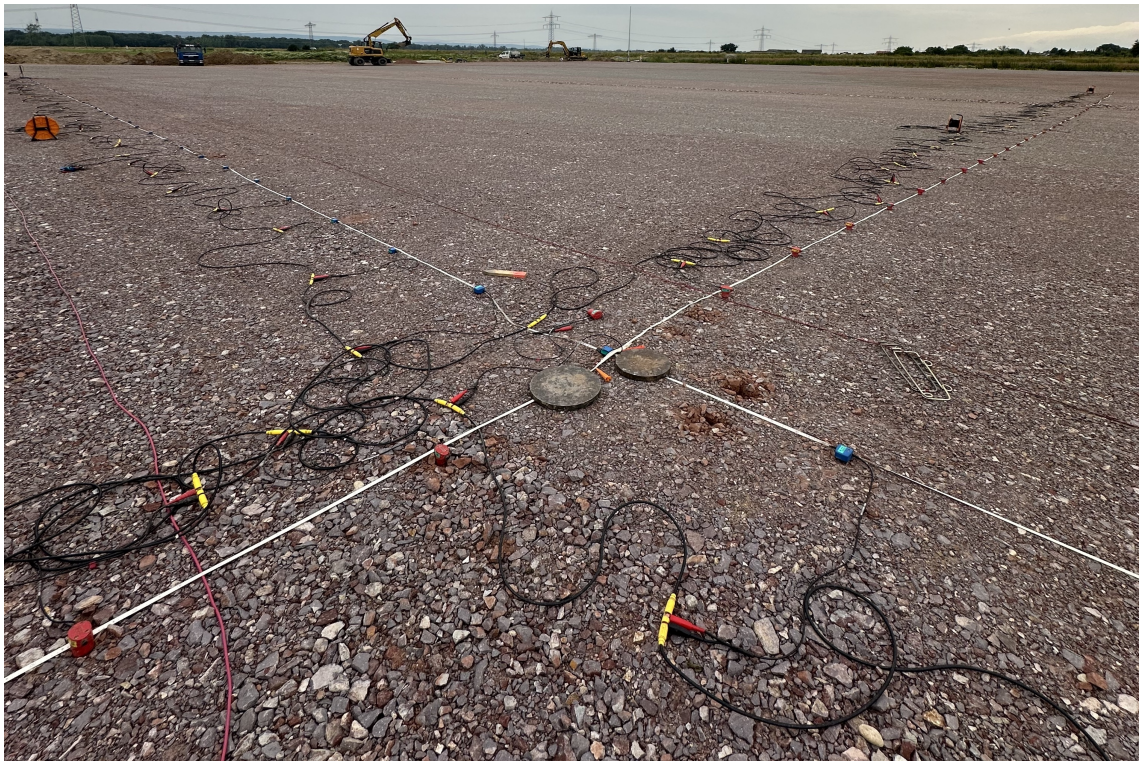


Figure 4.4: *MASW field acquisition configuration at the Herrenknecht test site (Photograph by the author).*



Figure 4.5: *Seepage trench and displacement of the geophones (Photograph by the author).*

Chapter 5

Multichannel analysis of surface waves applied to field data

In this chapter, selected data acquired during the first step of the MASW method at the test site are presented. The analysis begins with the differentiation of various wave phases, the identification of the dominant phase, and the characterization of the overall behavior of the seismic wavefield. This is followed by dispersion analysis, which encompasses both the imaging of dispersion curves and the semi-manual picking process. Subsequently, inversion analysis is performed on all selected dispersion curves obtained from each shot along the first and second profiles. From these analyses, the corresponding one-dimensional shear-wave velocity models are derived. The process concludes with the calculation of the median and the overall median of the resulting models. Finally, the chapter validates the inversion results through a comparison of synthetic data, generated from the inversion models, with the actual observed data.

5.1 Field data and dispersion analysis

In this section, field data are presented, and dispersion curve imaging is applied to all shots using the `MASWaves` software. For the imaging process, the velocity range defined in Eq. 3.6 was used, specifying a minimum test phase velocity of 100 m/s, a maximum of 800 m/s, and a test velocity step of 2 m/s. The frequency range was defined from 0 to 200 Hz. This range was selected after an initial inspection of the dispersion images revealed that the fundamental mode did not extend beyond 200 Hz.

Since each profile consists of 20 shots, the presentation and discussion are limited to selected shots in order to maintain clarity. The focus is placed on the first and last shots of each profile. For the first profile, these are shot 1 and shot 20. For the second profile, they are shot 28 and shot 47. In addition, the analysis includes shots acquired at the center of each profile, namely shot 10 for the first profile and shot 37 for the second profile.

Fig. 5.1 displays shot 1, 10, and 20 from the first profile, recorded at the test site. All traces were normalized to enhance visibility and to allow for better differentiation among seismic phases. Shot 1, shown in Fig. 5.1a, exhibits a low-amplitude direct wave at short offsets and a weak refracted wave whose amplitude decreases with offset. Due to the weakness of the refracted wave, it was not possible to apply refracted wave analysis to estimate the number of layers and their respective P-wave velocities.

The Rayleigh surface wave dominates the shot gather. The seismogram shows pronounced dispersion beginning around 0.1 s at an offset of 10 m. The widening of the seismic wavelet

with offset reflects strong dispersion characteristics, indicating that the shallow subsurface comprises layers with varying velocities. This dominance aligns with expectations, as the acquisition setup—with a vertically oriented sledgehammer source and vertical geophones—was optimized for Rayleigh wave analysis.

Shot 10, recorded at the center of the first profile (Fig. 5.1c), shows an asymmetrical wavelet between the left and right sides of the shot gather. It is evident that the left side exhibits stronger dispersion compared to the right, suggesting a variation in subsurface properties along the first profile.

Fig. 5.1e presents the seismogram from shot 20, the last shot of the first profile. Surface waves again dominate the seismogram, but the dispersion is noticeably weaker. Dispersion begins at approximately −18 m offset and becomes more pronounced with increasing offset.

The dispersion images derived from the data reveal only the fundamental mode of the dispersion curves for surface waves. In Fig. 5.1b, the dispersion curve of shot 1 begins at a frequency of 10 Hz with a high velocity of 450 m/s. As the frequency increases, the velocity decreases, then rises again above 200 m/s before declining once more. Interruptions in the curve appear near 55 Hz and 100 Hz. Overall, the curve exhibits an irregular shape and reaches up to 145 Hz, where the amplitude becomes weak. The pronounced dispersion observed in the shot gather (Fig. 5.1a) is reflected in the corresponding dispersion image.

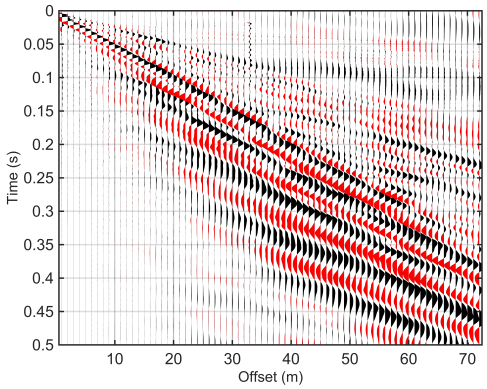
In contrast, Fig. 5.1f displays a less complex dispersion pattern. The highest amplitude occurs at low frequencies, with a corresponding velocity of approximately 450 m/s. The velocity decreases smoothly without interruption, increases near 60 Hz, and then declines again. The maximum observed frequency is 90 Hz.

The dispersion image of shot 10 (Fig. 5.1d) exhibits a distinctly broader dispersion curve with low amplitudes between 20 and 50 Hz. This characteristic is likely due to the asymmetry between the left and right sides of the shot gather. Notable variations in both waveform and corresponding dispersion images are observed from one shot to the next along the first profile (see Fig. 5.1d).

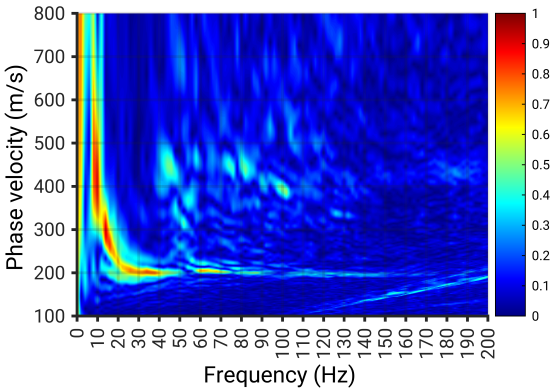
Fig. 5.2 presents the first, middle, and last shots (28, 37, and 47) of the second profile. Surface-wave dominance is clearly evident, and dispersion related to the widening of the seismic wavelet is readily observable. The waveforms exhibit symmetrical behavior along the profile, in contrast to those observed in shots 1, 10, and 20 of the first profile. Shot 37 displays better symmetry between the left and right sides. However, shot 47 (Fig. 5.2e) exhibits slightly reduced dispersion.

The dispersion images of shot 28 (Fig. 5.2b), shot 37 (Fig. 5.2d), and shot 47 (Fig. 5.2f) display a consistently smooth shape, with a maximum frequency of approximately 70 Hz.

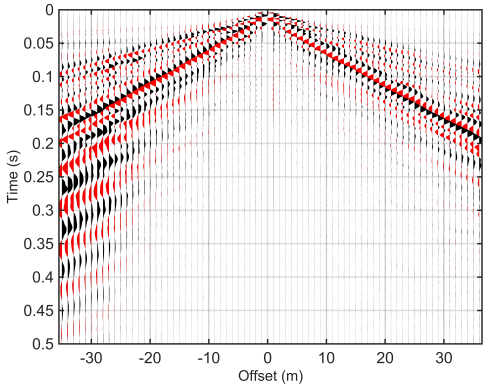
This preliminary assessment suggests that the second profile might exhibit lower heterogeneity compared to the first profile.



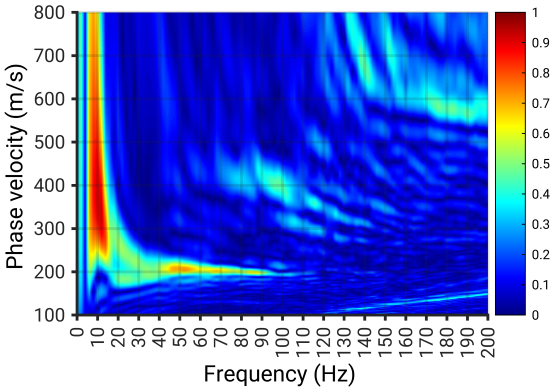
(a) *Observed shot 1*



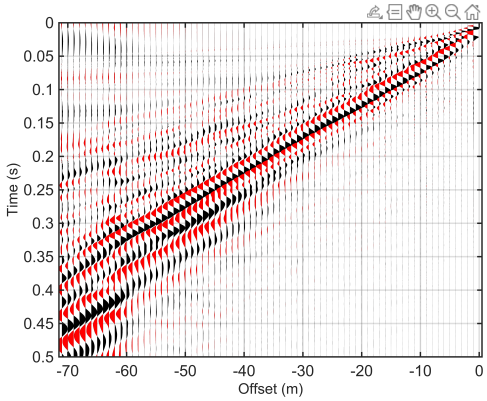
(b) *Dispersion image shot 1*



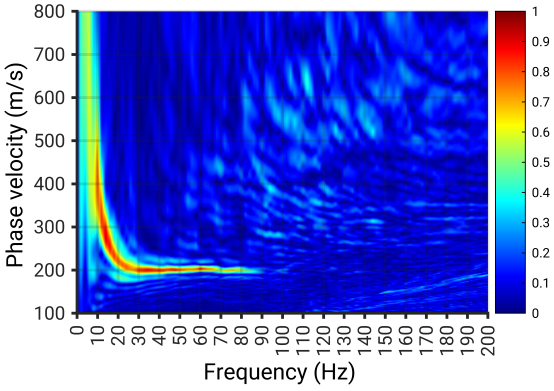
(c) *Observed shot 10*



(d) *Dispersion image shot 10*

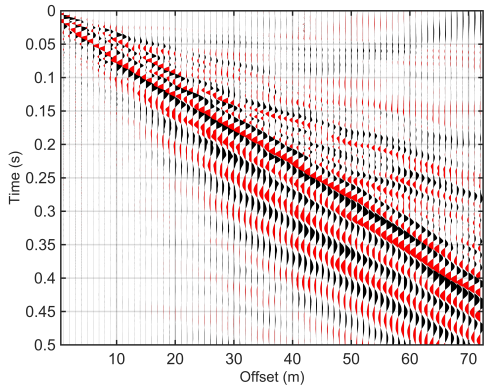


(e) *Observed shot 20*

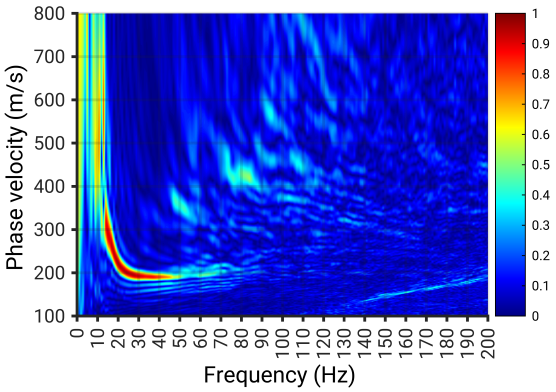


(f) *Dispersion image shot 20*

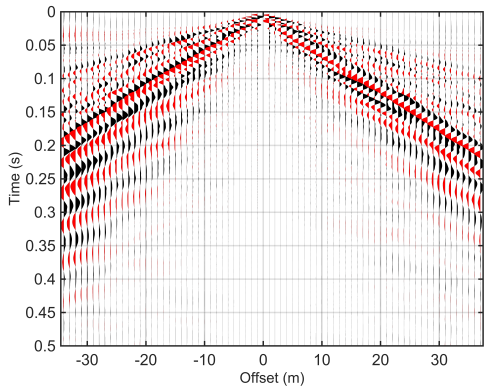
Figure 5.1: *Seismograms from shot 1 (a), shot 10 (c), and shot 20 (e), along with their corresponding dispersion images (b, d, and f).*



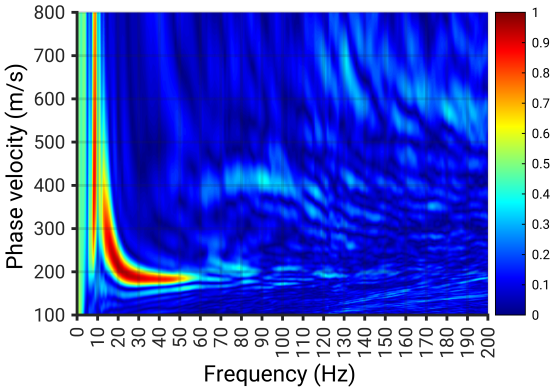
(a) Observed shot 28



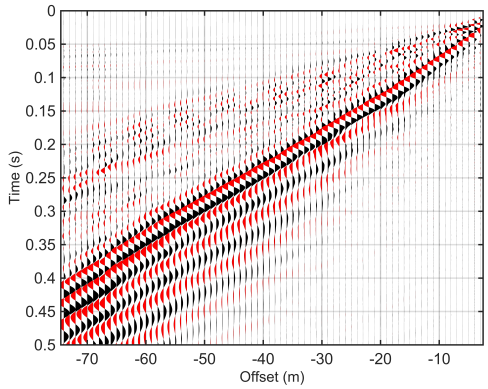
(b) Dispersion image shot 28



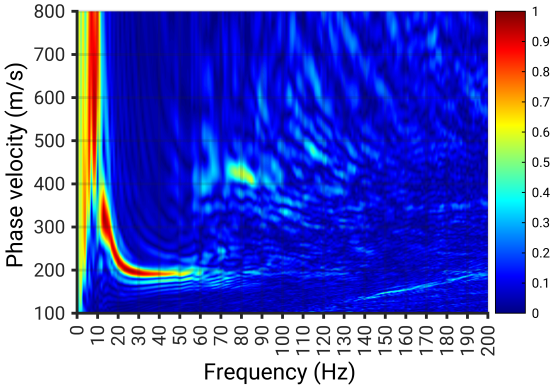
(c) Observed shot 37



(d) Dispersion image shot 37



(e) Observed shot 48

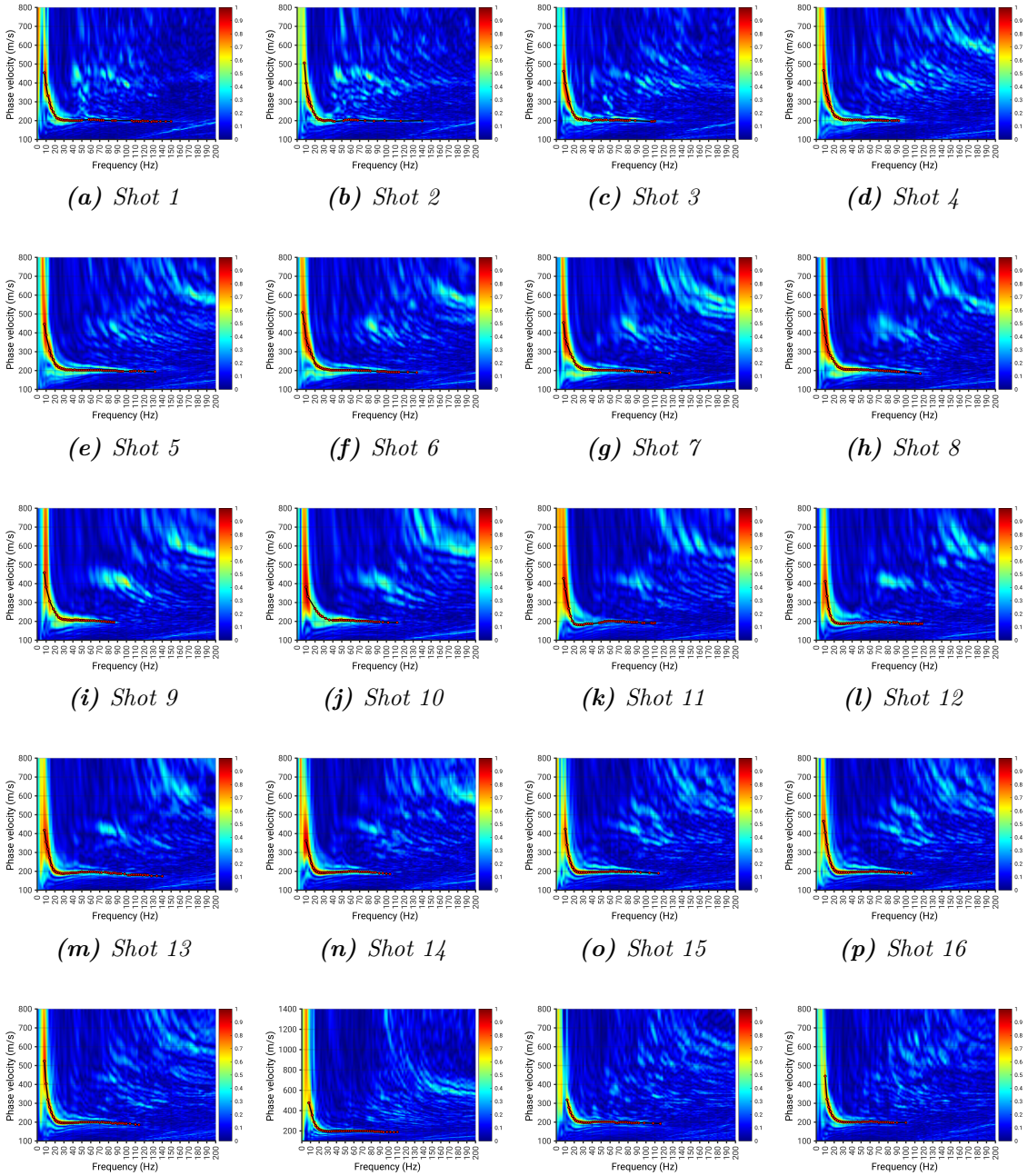


(f) Dispersion image shot 48

Figure 5.2: *Seismograms from shot 28 (a), shot 37 (c), and shot 47 (e), along with their corresponding dispersion images (b, d and f).*

The dispersion curves were extracted through a semi-manual process: initial picks made by the software were refined by manually removing points unrelated to the fundamental mode. This approach ensured a smooth and continuous curve, avoiding abrupt jumps and thereby facilitating the subsequent inversion analysis, which aims to minimize the misfit between the theoretical and calculated dispersion curves.

Every point associated with the fundamental mode at higher frequencies was deliberately picked, even when the corresponding amplitude was relatively low. This was done to ensure accurate resolution of the very shallow subsurface layers during inversion analysis. The maximum frequency in the picked dispersion curves varied from shot to shot, generally ranging between 70 and 120 Hz. Some shots extended up to 150 Hz (see Fig. 5.3 and Fig. 5.4).



(a) Shot 1 *(b) Shot 2* *(c) Shot 3* *(d) Shot 4*

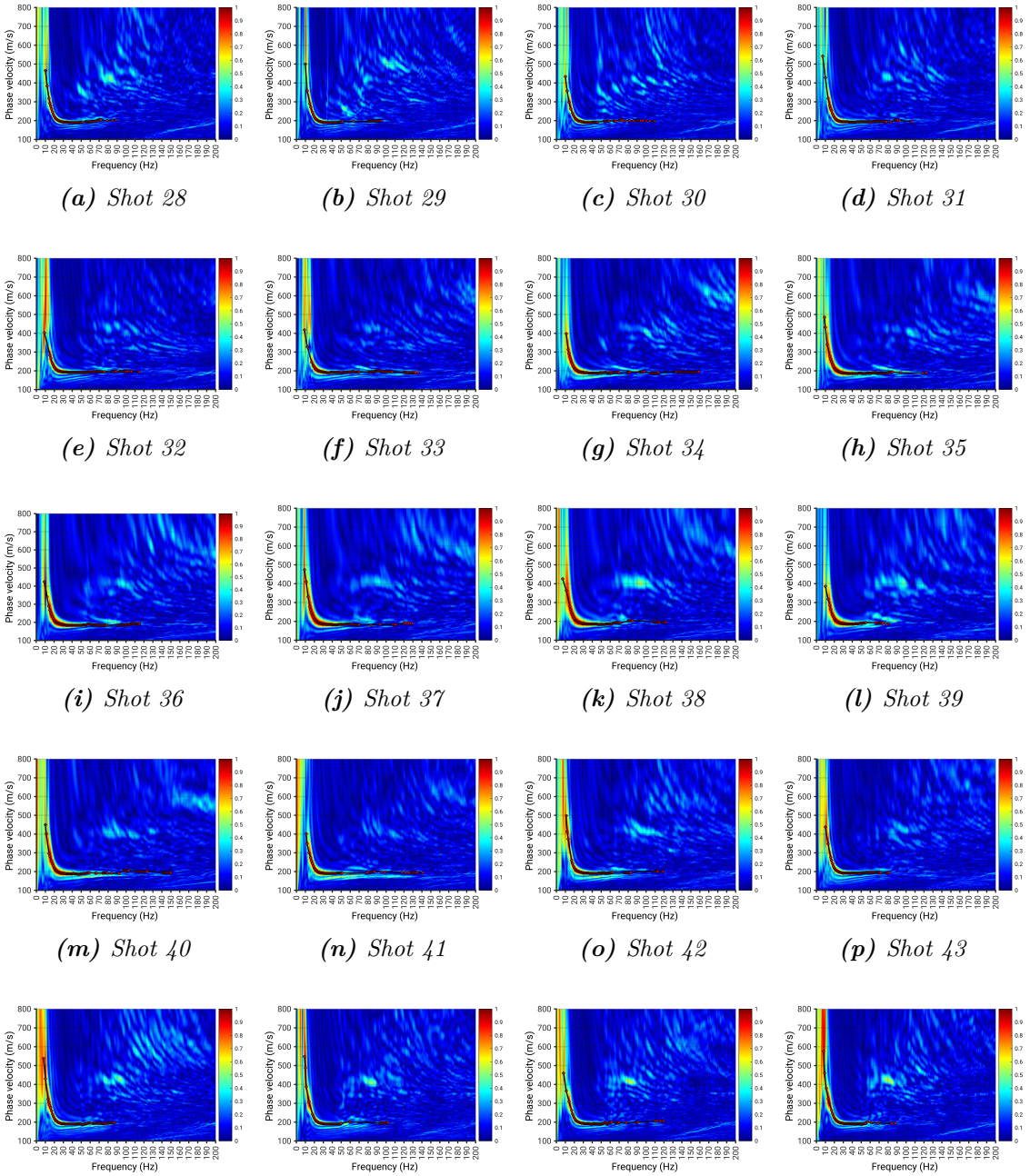
(e) Shot 5 *(f) Shot 6* *(g) Shot 7* *(h) Shot 8*

(i) Shot 9 *(j) Shot 10* *(k) Shot 11* *(l) Shot 12*

(m) Shot 13 *(n) Shot 14* *(o) Shot 15* *(p) Shot 16*

(q) Shot 17 *(r) Shot 18* *(s) Shot 19* *(t) Shot 20*

Figure 5.3: *Dispersion images for shots 1 through 20, with the corresponding picked dispersion curve indicated by red points.*



(a) *Shot 28* ***(b)*** *Shot 29* ***(c)*** *Shot 30* ***(d)*** *Shot 31*

(e) *Shot 32* ***(f)*** *Shot 33* ***(g)*** *Shot 34* ***(h)*** *Shot 35*

(i) *Shot 36* ***(j)*** *Shot 37* ***(k)*** *Shot 38* ***(l)*** *Shot 39*

(m) *Shot 40* ***(n)*** *Shot 41* ***(o)*** *Shot 42* ***(p)*** *Shot 43*

(q) *Shot 44* ***(r)*** *Shot 45* ***(s)*** *Shot 46* ***(t)*** *Shot 47*

Figure 5.4: *Dispersion images for shots 28 through 47, with the corresponding picked dispersion curve indicated by red points.*

5.2 Inversion analysis

As mentioned in section 3.2.1, all shots from both the first and second profiles are used for inversion. The picked dispersion curves for each shot (5.3 and 5.4) will be inverted using the global inversion workflow described in section 3.2.4 to obtain individual 1D shear-velocity profiles (V_S). Each inverted model from both profiles will be plotted to assess whether there is significant variation between the shots of the same profile. In addition, the median and standard deviation of the models are calculated and presented.

The initial model parameters for inversion (Fig. 3.5)—specifically, the layer thickness h and shear-wave velocity β—were established through visual inspection, assessment of soil characteristics (Table 4.1), preliminary evaluation of the theoretical dispersion curve, and a series of initial inversion tests performed on the first shot.

These procedures were undertaken to optimize the starting model, thereby reducing the misfit, shortening the inversion processing time, and minimizing the likelihood of failure due to significant discrepancies between the initial and actual subsurface models. The parameters employed are presented in Table 5.1.

The initial model assumes five layers $n = 5$ above a half-space. The P-wave velocity α and density ρ are assumed to be constant, as surface waves are relatively less sensitive to variations in these parameters. The P-wave velocity α was set to 1440 m/s, reflecting the assumption of a partially consolidated but saturated soil—specifically, silty sand or soft clay. The corresponding density was set to $\rho = 1850$ kg/m^3.

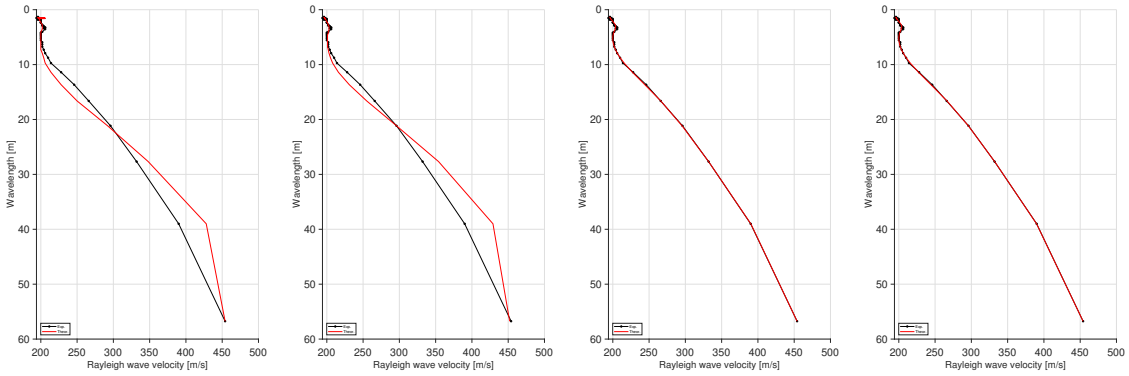
Table 5.1: *Initial model parameters used for the inversion analysis.*

Layer	h (m)	β (m/s)	α (m/s)	ρ (kg/m^3)
1	0.1	300.0	1440	1850
2	0.3	230.0	1440	1850
3	2.0	211.0	1440	1850
4	4.0	205.0	1440	1850
5	5.0	430.0	1440	1850
6	∞	519.0	1440	1850

Fig. 5.5 presents the results of the global inversion process applied to shot 1 as a representative example. Due to the impracticality of displaying the results for all 40 shots, only the complete inversion process for this single shot is presented.

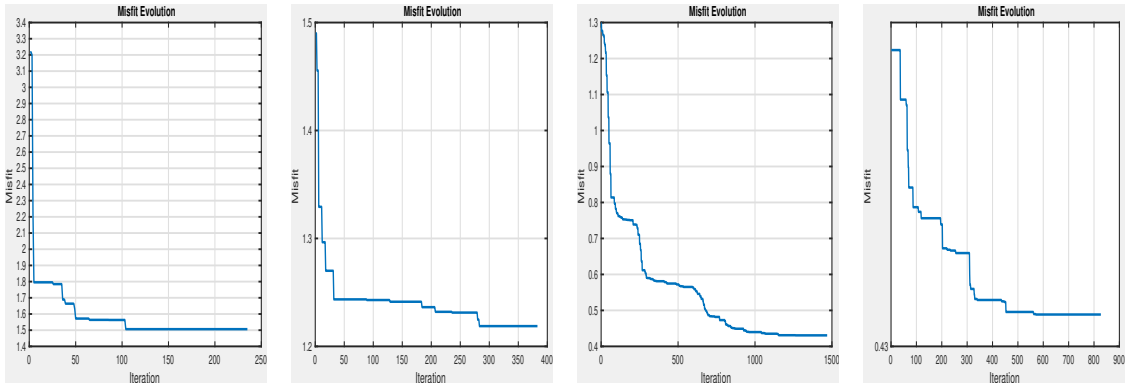
Each inversion step employed a different testing velocity, c_T, and is accompanied by a comparison between theoretical and experimental dispersion curves, plotted as wavelength versus Rayleigh-wave velocity. The misfit evolution throughout the inversion and the corresponding 1D shear-wave velocity V_S profile are also shown for each step.

The misfit was significantly reduced from 3.2 % to 1.5 % by using $c_T = 2$ m/s in the first step. A minor improvement was observed in the second step, followed by a substantial reduction in misfit—from 1.5 % to below 0.5 %—in the third step. This reduction is reflected in the increased agreement between theoretical and experimental dispersion curves. In the final step, the misfit improved slightly further. Although the numerical improvement was small, it had a notable impact on minimizing discrepancies between the curves, particularly at short wavelengths and low velocities.



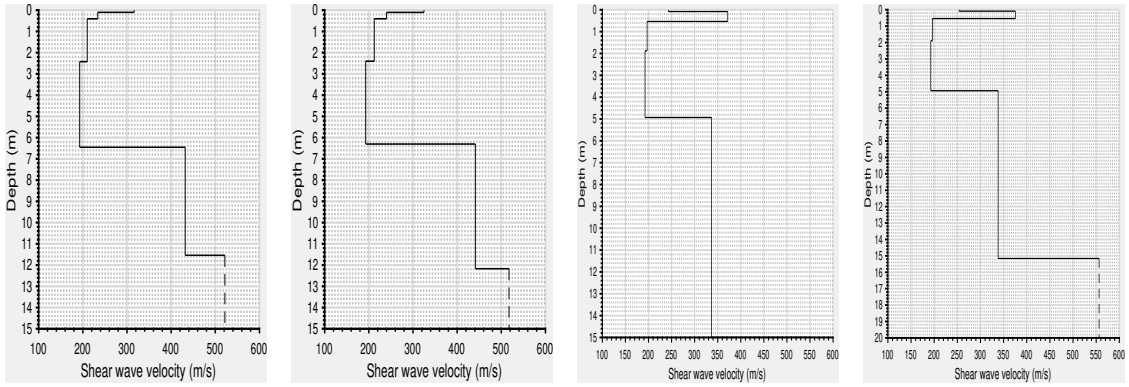
(a) $c_T = 2.0\ m/s$ ***(b)*** $c_T = 1.0\ m/s$ ***(c)*** $c_T = 0.1\ m/s$ ***(d)*** $c_T = 0.03\ m/s$

Theoretical vs experimental dispersion curves



(e) $c_T = 2.0\ m/s$ ***(f)*** $c_T = 1.0\ m/s$ ***(g)*** $c_T = 0.1\ m/s$ ***(h)*** $c_T = 0.03\ m/s$

Misfit history for different values of c_T



(i) $c_T = 2.0\ m/s$ ***(j)*** $c_T = 1.0\ m/s$ ***(k)*** $c_T = 0.1\ m/s$ ***(l)*** $c_T = 0.03\ m/s$

shear-wave velocity profiles

Figure 5.5: *Comparison of inversion results for shot 1 with* $c_T = 2,\ 1,\ 0.1,$ *and* $0.03\ m/s$*: (top) dispersion curves; (middle) misfit histories; and (bottom) shear-wave velocity profiles.*

First profile:

The same procedure was applied to all shots in both the first and second profiles. Fig. 5.6a presents the calculated dispersion curves for each shot, displayed as frequency versus Rayleigh-wave velocity. All curves exhibit the same general shape, with some shots showing low velocities—below 200 m/s—at low frequencies (25–40 Hz). As the frequency increases, the phase velocity rises to 200 m/s and above, before decreasing again at higher frequencies (see shot 13).

A similar pattern can be observed in the Rayleigh-wave velocity versus wavelength plot (Fig. 5.6b). At low frequencies or longer wavelengths, where the velocity is higher, the dispersion curves differ significantly between shots, especially in the wavelength range of 35 to 56 m and 5 to 20 m. These variations at specific frequency or wavelength intervals are reflected in the 1D shear-velocity profiles V_S for each shot (Fig. 5.7a).

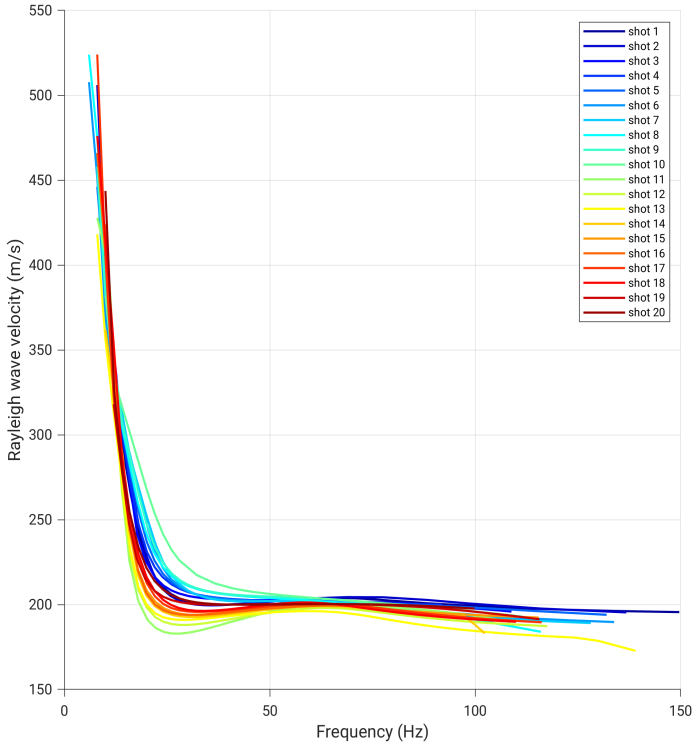
Fig. 5.7b displays the median shear-wave velocity profile (black line) and the standard deviation (in gray). At shallow depths up to 2 m, there is significant variability in velocity and thickness between shots. Between 2 and 12 m depth, the variation becomes minimal and remains within acceptable limits. However, at greater depths 14 to 19 m, the thickness of the fifth layer and velocity of the half space below vary noticeably among shots. This variability may be attributed to experimental dispersion curves for some shots that show higher amplitudes at low frequencies and correspondingly high velocities, thereby increasing the inferred depth of the fifth layer in certain shots.

Second profile:

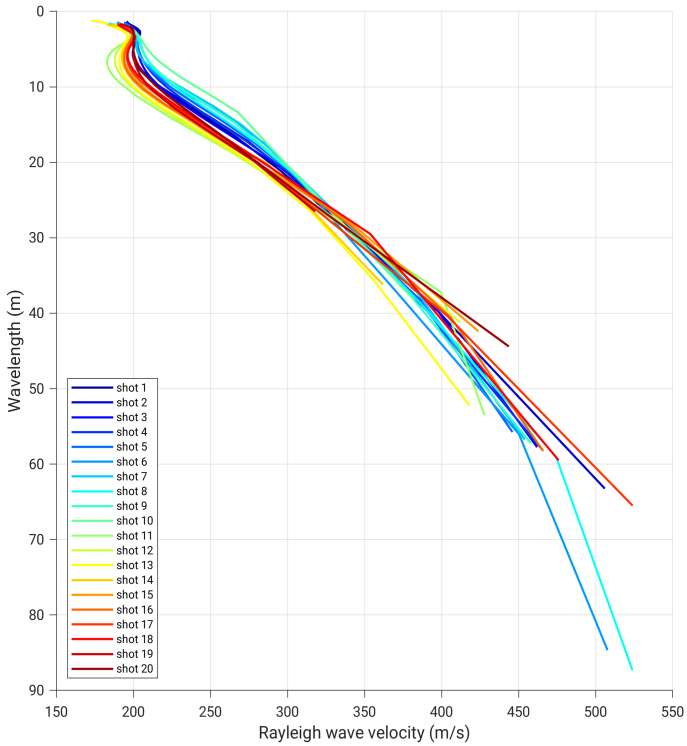
The calculated dispersion curves in Fig. 5.8a and Fig. 5.8b exhibit high similarity and consistency across all shots over all frequencies. These curves display less variation compared to the dispersion curves calculated from the shots of the first profile. Only in the low-frequency, long-wavelength range does the variation increase, which may be attributed to the same factors described for the first profile.

The 1D shear-velocity profiles for all shots (Fig. 5.9a) reveal similar structural characteristics: a thin, low-velocity shallow layer overlying a relatively higher-velocity layer, which is thicker than the first. This is followed by a lower-velocity layer with velocities below 200 m/s. The velocity difference between the third and fourth layers is minimal, suggesting that these layers could be merged, thereby reducing the model to a four-layer representation instead of five.

The standard deviation is significantly smaller than that observed in the first profile (see Fig. 5.9b).

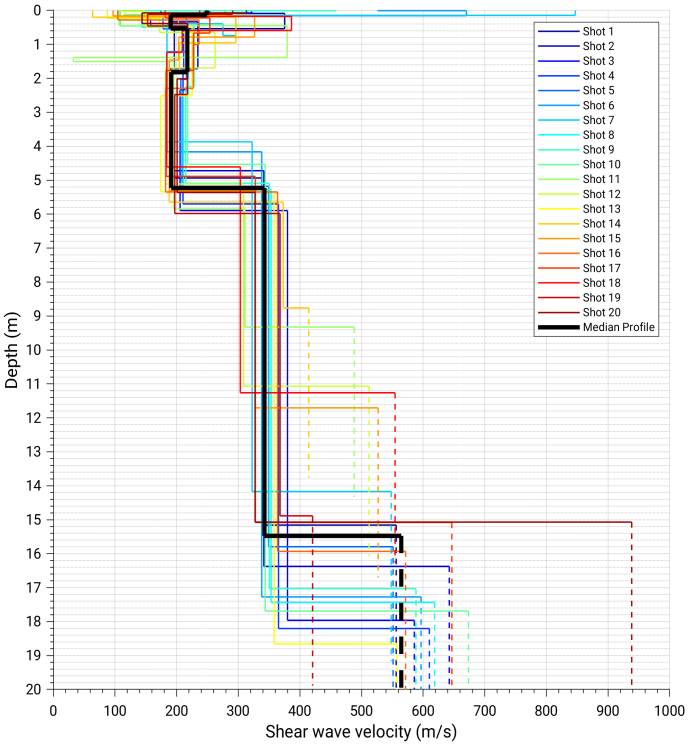


(a) *Freguency vs. Rayleigh-velocity.*

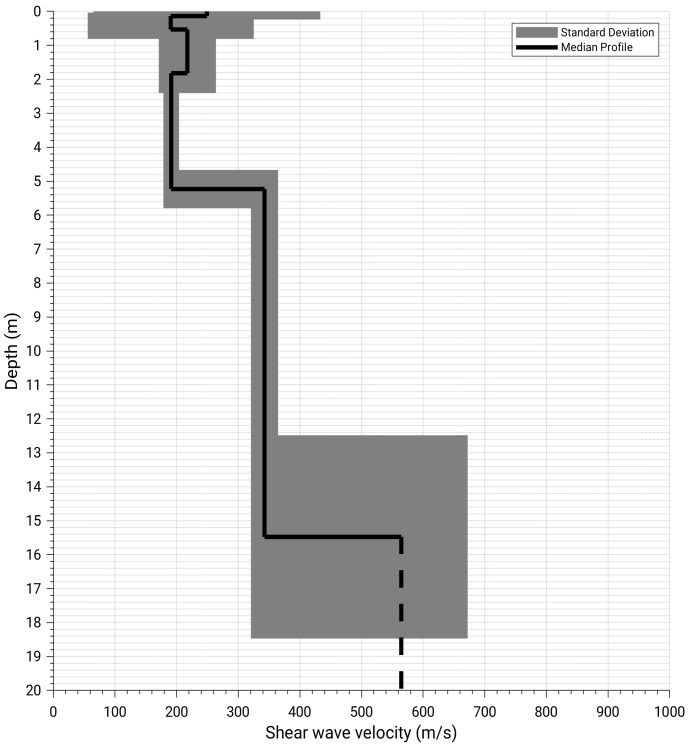


(b) *Rayleigh-velocity vs. wavelength.*

Figure 5.6: *Inversion results from all shots along the first profile: (a) theoretical dispersion curves—frequency versus Rayleigh-wave velocity; (b) theoretical dispersion curves—Rayleigh-wave velocity versus wavelength.*

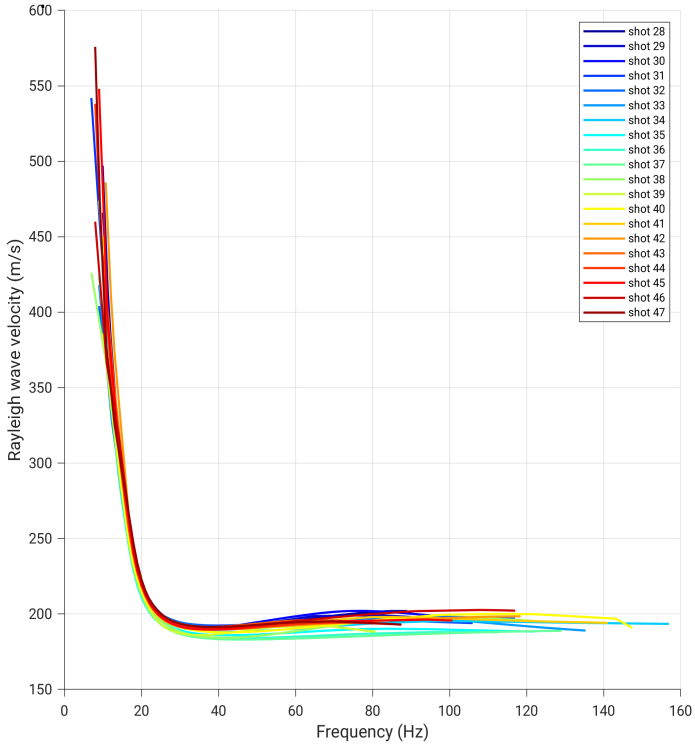


(a) *Shear-velocity profiles of the first profile.*

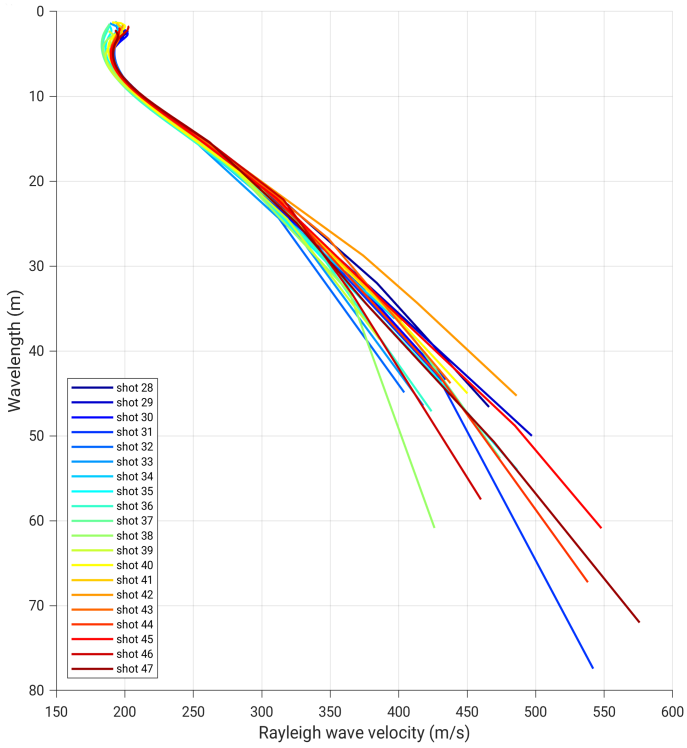


(b) *Median shear-velocity profile and its standard deviation.*

Figure 5.7: *Inversion results from all shots along the first profile: (a) shear-wave velocity profiles; and (b) the median shear-wave velocity profile with its standard deviation.*

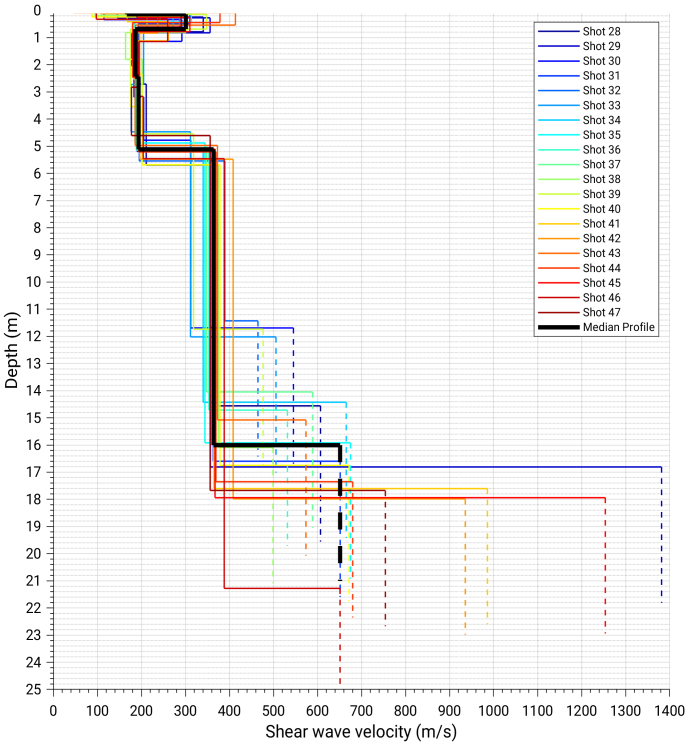


(a) *Shear-velocity profiles of the first profile.*

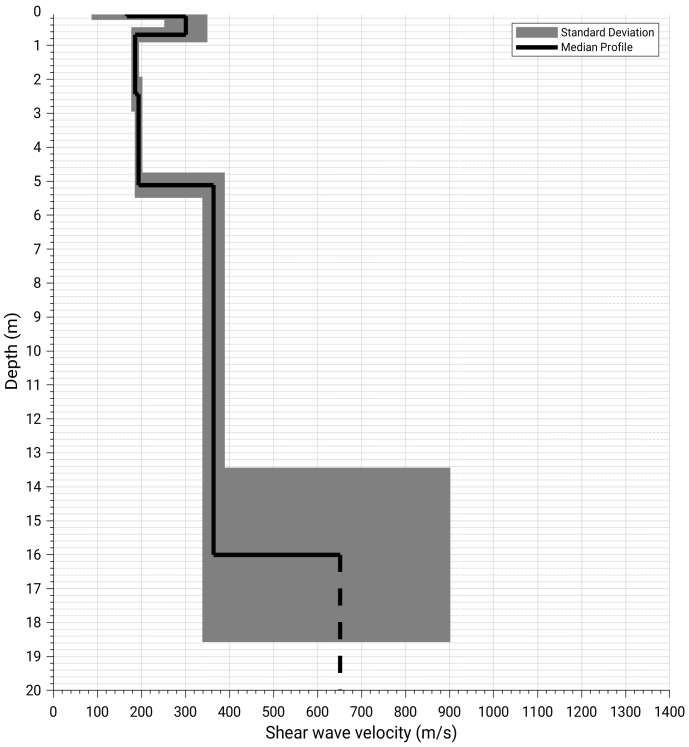


(b) *Rayleigh-velocity vs. wavelength.*

Figure 5.8: *Inversion results from all shots along the second profile: (a) theoretical dispersion curves—frequency versus Rayleigh-wave velocity; (b) theoretical dispersion curves—Rayleigh-wave velocity versus wavelength.*



(a) *Shear-velocity profiles of the second profile.*



(b) *Median shear-velocity profile and its standard deviation.*

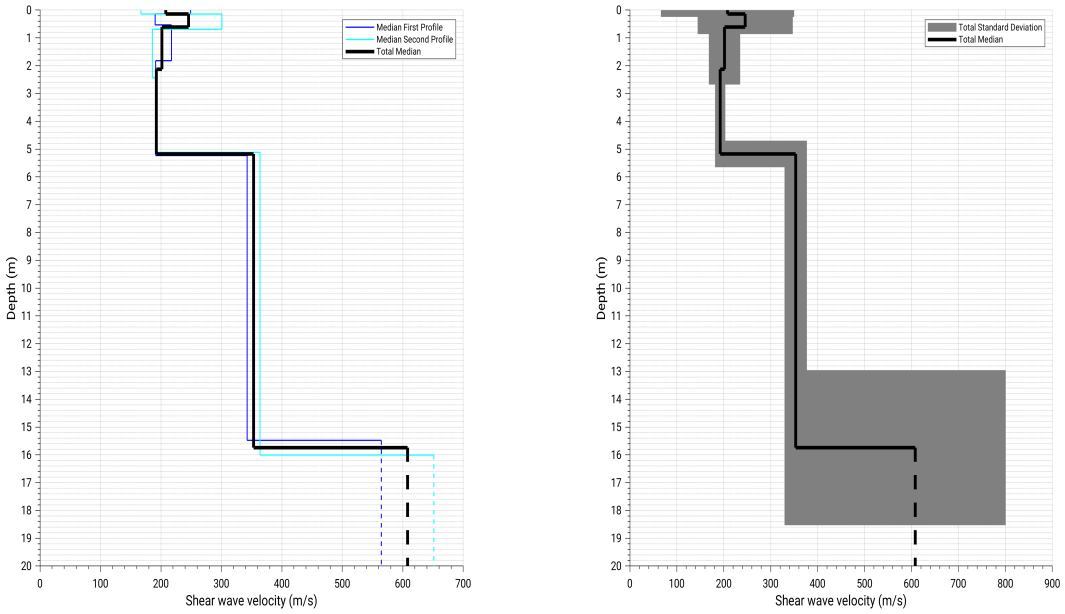
Figure 5.9: *Inversion results from all shots along the second profile: (a) shear-wave velocity profiles; and (b) the median shear-wave velocity profile with its standard deviation.*

Total median:

The 1D dimensional median shear-velocity profile for the first and second profiles, as well as the total median profile, are shown in Fig. 5.10a. These results support the earlier discussion: the top 2 m of the profiles differ markedly, whereas the sections below 2 m—particularly in the fourth and fifth layers—exhibit a high degree of similarity and agreement between the two profiles, which is encouraging. The slight variation observed in the shear-velocity of the fifth layer is very small.

Moreover, the total standard deviation of the total median profile, illustrated in Fig. 5.10b, reveals that the greatest deviations occur near the surface, specifically within the top three thin layers and at the half-space boundary.

Table 5.2 presents all inversion model parameters and their deviations (in percent), which emphasize the strong variability in the shallow subsurface.



(a) *(b)*

Figure 5.10: *Inversion results for both profiles: (a) median shear-wave velocity profiles of the first and second profiles; and (b) the total median shear-wave velocity profile, including its standard deviation.*

Table 5.2: *Inversion model parameters for the first and second profiles, along with the total median values and their associated uncertainties.*

First profile		**Second profile**		**Total median**	
z (m)	β (m/s)	z (m)	β (m/s)	z (m)	β (m/s)
0.1 ± 100.0%	249.1 ± 73.8%	0.1 ± 100.0%	166.9 ± 48.0%	0.1 ± 100.0%	208.0 ± 68.2%
0.5 ± 40.0%	190.4 ± 70.8%	0.6 ± 33.3%	300.9 ± 16.3%	0.6 ± 33.3%	245.6 ± 41.2%
1.8 ± 27.8%	217.4 ± 21.3%	2.4 ± 20.8%	185.8 ± 4.7%	2.1 ± 23.8%	201.6 ± 16.5%
5.2 ± 9.6%	191.2 ± 6.6%	5.1 ± 5.9%	193.6 ± 4.5%	5.1 ± 7.8%	192.4 ± 5.7%
15.4 ± 18.8%	342.6 ± 6.4%	16.0 ± 15.6%	363.9 ± 7.0%	15.7 ± 17.2%	353.2 ± 6.7%
∞ ± 0.0%	564.5 ± 19.1%	∞ ± 0.0%	651.4 ± 38.4%	∞ ± 0.0%	607.9 ± 31.7%

V_P = 1440 m/s, ρ = 1850 kg/m^3

5.3 Model validation through synthetic and observed data comparison

In this section, the inversion results of the first and second profiles are verified by means of a comparison between the synthetic modeled seismograms and dispersion curves, derived from the inversion results, and their corresponding field counterparts. Forward modeling is performed using the software `SOFI2D` (Bohlen et al., 2016), in which the viscoelastic wave equation is solved. A quality factor of $Q = 15$ is applied, and the relaxation time τ and the five relaxation frequencies are computed.

A two-dimensional model comprising 1000 grid points in the x-direction and 200 grid points in the y-direction, with a uniform spacing of 0.1 m between each grid point, defines a model domain measuring 100 m in width and 20 m in depth. The surface is treated as a free surface. An absorbing frame with a width of 40 grid points is applied to minimize boundary reflections.

The acquisition parameters—including shot locations, receiver spread, and receiver spacing intervals—are identical to those employed during the field acquisition. The model parameters used in `SOFI2D` are presented in Table 5.2.

The comparison is conducted solely on the first and last shots, without the application of any signal processing. Consequently, the noise present in the observed data must be taken into account.

Table 5.3: *`SOFI2D` model parameter; Depth (z), S-wave velocity (β), P-wave velocity (V_P), density (ρ), quality factors (Q_S, Q_P), number relaxation mechanisms (L), relaxiation of frequencies (f) and relaxation time (τ).*

	First profile		**Second profile**		**Total median**					
Layer	z (m)	β (m/s)	z (m)	β (m/s)	z (m)	β (m/s)	V_P (m/s)	ρ (kg/m^3)	Q_S	Q_P
1	0.1	249.1	0.1	166.9	0.1	208.0	500	1850	15	15
2	0.5	190.4	0.6	300.9	0.6	245.6	450	1850	15	15
3	1.8	217.4	2.4	185.8	2.1	201.6	400	1850	15	15
4	5.2	191.2	5.1	193.6	5.1	192.4	450	1850	15	15
5	15.4	342.6	16.0	363.9	15.7	353.2	2000	2000	15	15
6	∞	564.5	∞	651.4	∞	607.9	2200	2000	15	15

$L = 5$, $f = 1.8$, 5.5, 20.6, 81.8, 130.1 Hz, $\tau = 0.06$ s

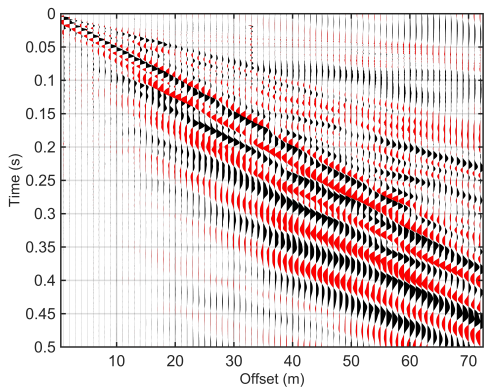
First profile:

The assumed model is laterally homogeneous, and thus, the first and last shots appear identical in both the seismogram and the dispersion curve. When comparing observed shot 1 (Fig. 5.11) to its modeled counterpart, significant differences are evident; the observed shot exhibits a strong dispersion signature. In contrast, both the observed and modeled shot 20 display a closer match in waveform characteristics. The dispersion curve of the modeled data aligns well with that of observed shot 20, particularly in the frequency range of 15 to 60 Hz.

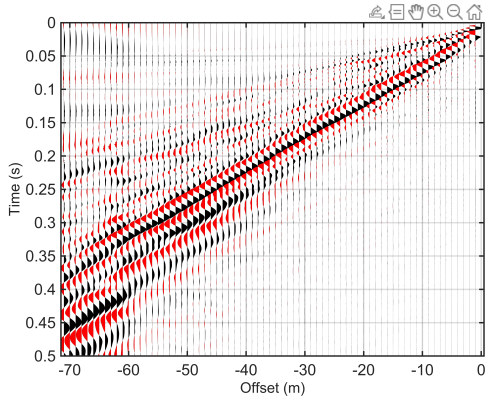
Both observed shots 1 and 20 contain high amplitudes at low frequencies and high velocities. However, the dispersion curve of shot 1 matches the modeled data only within the 15 to 40 Hz frequency range with slightly higher velocity.

Second profile:

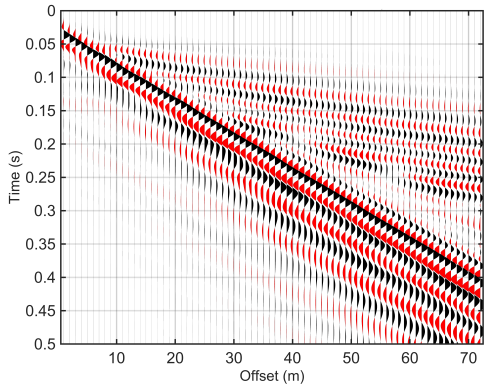
In Fig. 5.12 observed shot 28 exhibits greater waveform dispersion and noise compared to the modeled counterpart. In contrast, shot 47 appears more promising, with a waveform that closely resembles the modeled version. Dispersion images of all observed and synthetic data display a consistent pattern within the frequency range of 15 to 50 Hz. The observed dispersion image shows higher amplitude at lower frequencies. This discrepancy may be addressed by increasing the number of layers in the initial inversion model, thereby extending the depth of investigation and enhancing the resolution of higher-velocity structures.



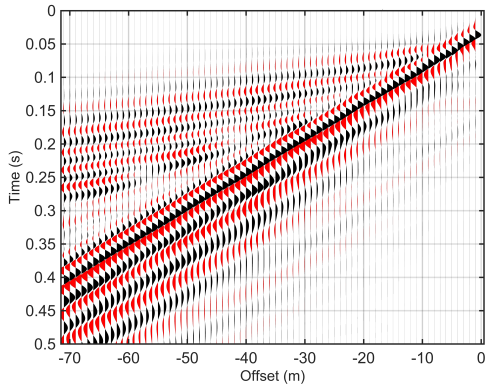
(a) Observed shot 1



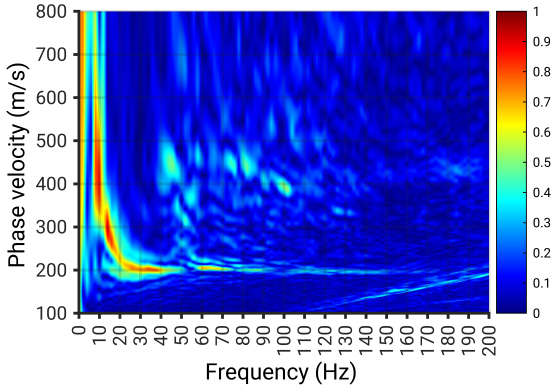
(b) Observed shot 20



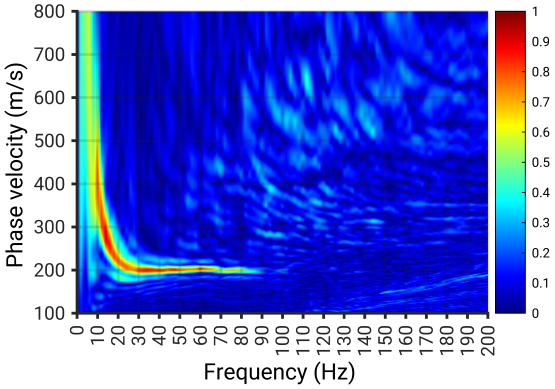
(c) Synthetic shot 1



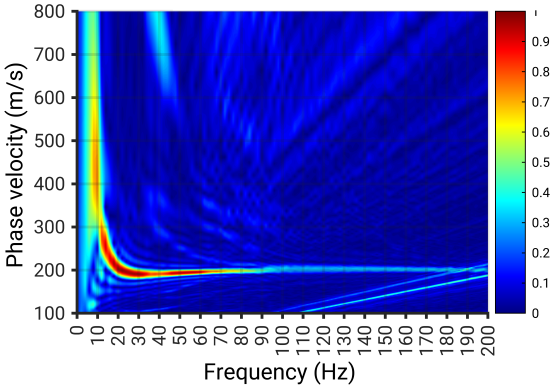
(d) Synthetic shot 20



(e) Dispersion image shot 1

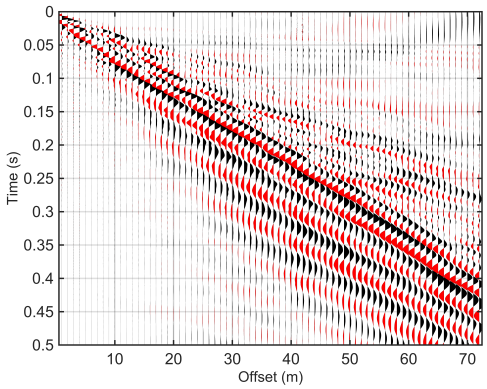


(f) Dispersion image shot 20

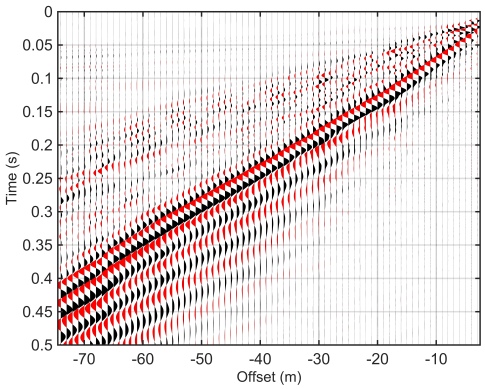


(g) Dispersion image synthetic

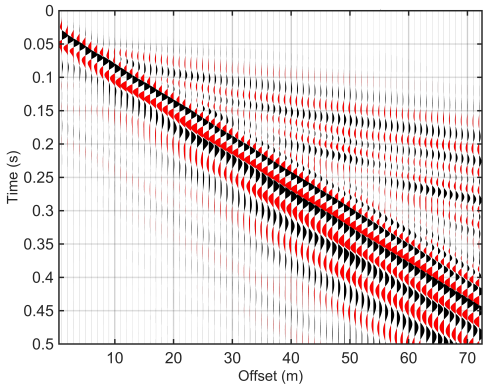
Figure 5.11: *Comparison between the observed real data from shots 1 and 20 of the first profile and the synthetic viscoelastic modeled data, calculated using an approximate quality factor of* $Q = 15$.



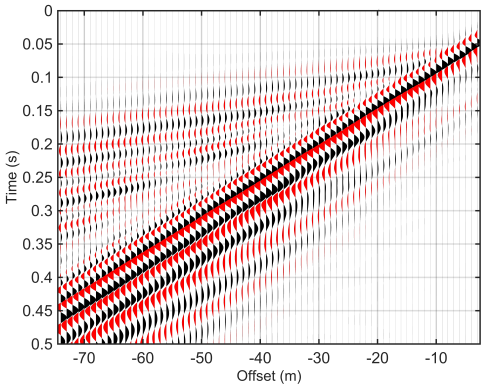
(a) Observed shot 28



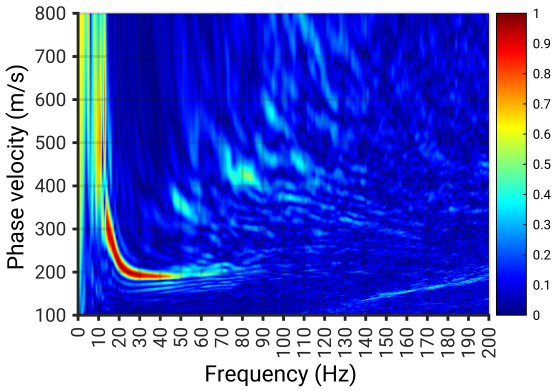
(b) Observed shot 47



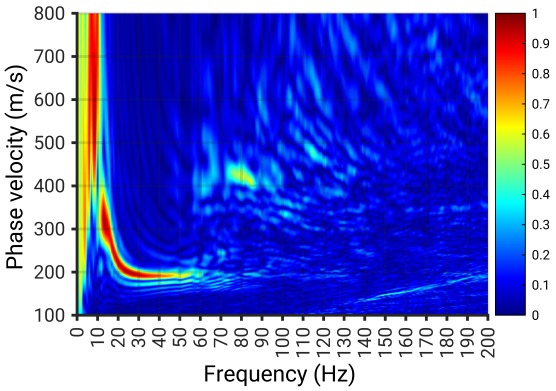
(c) Synthetic shot 28



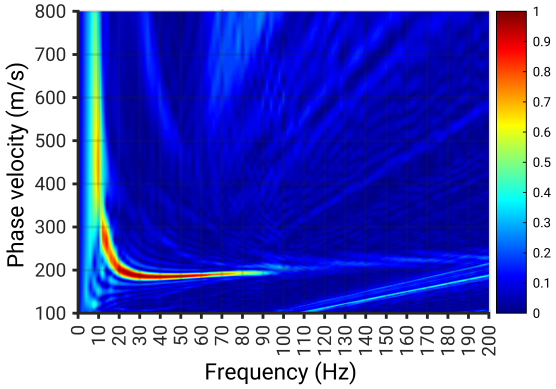
(d) Synthetic shot 47



(e) Dispersion shot 28



(f) Dispersion shot 47



(g) Dispersion synthetic

Figure 5.12: *Comparison between the observed real data from shots 28 and 47 of the second profile and the synthetic viscoelastic modeled data, calculated using an approximate quality factor of* $Q = 15$.

5.4 Discussion

The inversion based on the assumption of a five-layer model significantly reduces the misfit between the theoretical and experimental dispersion curves, particularly at higher frequencies and at low-velocity picked points. This result indicates that the five-layer model is the minimum required to describe the test site adequately down to an investigation depth of approximately 16 m. Adding more layers primarily increases the investigation depth.

Under the assumption of lateral homogeneity, it is essential to differentiate between the first and second profiles. The first profile—derived from seismograms of all shots and their corresponding dispersion images—exhibits considerable variation along the profile. This assertion is supported by the shear-wave velocity profiles and the inversion model parameters, which reveal pronounced variation in both depth and velocity in the shallow subsurface, particularly within the upper 2 m (see Table 5.2). In contrast, the second profile demonstrates greater consistency in both the seismograms and the shape of the dispersion images, with less variation in the shallow subsurface compared to the first profile.

Variation in the thickness and velocity of the shallow subsurface along the measured profiles—particularly along the first profile—can be attributed to two primary factors. First, the test site comprises engineered fill soils in the upper two layers, suggesting potential variability in both the thickness of the anthropogenic layer and the seismic velocity, owing to differences in the materials used. Specifically, variations in composition and grain size along the profile—especially between the red gravel and the underlying layer—contribute to this heterogeneity (see Fig. 3.3).

This factor is supported by the image taken at the test site (Fig. 4.5 on page 37) and the satellite image of the same location (Fig. 4.3), which reveal a change in material distribution from one position to another. This observation also explains why the left side of the seismogram for shot 10 (Fig. 5.1c) and shot 37 (Fig. 5.2c) differs from the right side along the profile.

The second factor is technically related to the acquisition parameters and the equipment used, which impose limitations on the MASW method. The minimum investigation depth is governed by the minimum wavelength $\lambda_{\min}$, the minimum observed velocity $c_{\min}$, and the maximum frequency $f_{\max}$, as expressed in Eq. 3.4.

The sledgehammer source employed in this study generates frequencies ranging from 10 to 50 Hz, while the maximum frequency $f_{\max}$ observed ranges between 80 and 120 Hz. The lowest recorded shear-wave velocity is approximately 190 m/s. Applying these values to the equation yields the best minimum observable thickness:

$$H_{min} \geq 0.5 \, \frac{190 \text{ m/s}}{120 \text{ Hz}} = 0.7 \text{ m} \tag{5.1}$$

In addition, the receiver spacing interval dx influences the value of $\lambda_{\min}$, as outlined in Eq. 3.5. Consequently, the minimum resolvable layer thickness H_{min} in our acquisition setup is approximately 1 m, which corresponds to the receiver spacing dx.

This configuration makes it difficult for the MASW method—given the applied acquisition parameters and the source used—to accurately resolve the uppermost shallow layers. For these reasons, the deviation is very high at such small thicknesses (see Table 5.2). Both factors should be considered jointly rather than separately, even though the first factor better explains the difference between the results of the two profiles.

Chapter 6

Estimation of quality factor (Q)

In this chapter, a new workflow for estimating the quality factor (Q), or in other words, the attenuation of near-surface seismic wave propagation, is presented using the spectral ratio method applied to multiple pairs of seismic traces with different distances between them (trace division). First, the method will be tested and validated on an analytical solution of wave propagation (an analytical shot gather) with a constant Q value. Then, it will be tested on a viscoelastic modeled shot gather using our inverted five-layer model, modeled using `SOFI2D` software. Finally, it will be evaluated whether the method yields reliable results when applied to real data acquired at the Herrenknecht test site, using all shots from the first and second profiles. We conclude the chapter with a discussion of the method's limitations and considerations necessary for achieving better results.

6.1 Application of spectral ratio method

Workflow for estimating Q value:

1. **Amplitude spectrum calculation:**
   - Compute the amplitude spectrum for each seismic trace.
   - Analyze the amplitude spectrum to identify dominant frequency components.
2. **Log-spectral ratio calculation:**
   - Select trace number 10 as the reference trace.
   - Calculate the log-spectral ratio for offsets of 10, 20, 30, 40, 50, 60, and 70 m.
   - Observe the decay of the amplitude spectra with increasing offset.
3. **Linear regression analysis:**
   - Perform a linear regression on the computed log-spectral ratios for $x_1 = (5,\ 10,\ 40)$ m and $x_2 = 70$ m.
   - Determine the slope, its confidence bounds, and the associated uncertainty.
   - Calculate the quality factor Q using Eq. 2.60 and its associated error .
4. **Extension to multiple trace pairs:**
   - Select trace number 5 as the new reference trace.
   - For each trace with a larger offset than the reference, calculate the log-spectral ratio.
   - Perform linear regression for each trace pair and estimate the corresponding Q and associated error.
   - Finally, compute the median of the obtained Q values and the median of their corresponding errors.
5. **Global Q estimation from all reference traces:**
   - Use each trace from 1 to 72 as a reference .

- For each reference trace, apply the same multiple-offset pairwise comparison as described in step 4.
- For each reference trace, calculate the median Q and the median error.
- Finally, compute the overall median value of Q, denoted as Q_{Global}, from all median Q values, and the overall median error.

6.1.1 Applications on analytical solution of acoustic seismic wave

Fig. 6.1 displays the shot gather with a constant quality factor, $Q = 20$, calculated using the 3D solution of the inhomogeneous acoustic wave equation (Eq. 2.68). A Ricker wavelet with a center frequency of $f_c = 40$ Hz was used as the source time function. The recording time and number of traces match those of the real acquisition: 72 traces with one-meter spacing intervals and a total recording time of 0.5 s (see Appendix A). Since this shot results from solving the acoustic wave equation, only a single phase, the P-wave, is observed.

To test the spectral ratio method for determining the Q factor and to compare it with the constant value used in the analytical solution $Q = 20$, the previously mentioned workflow will be adopted.

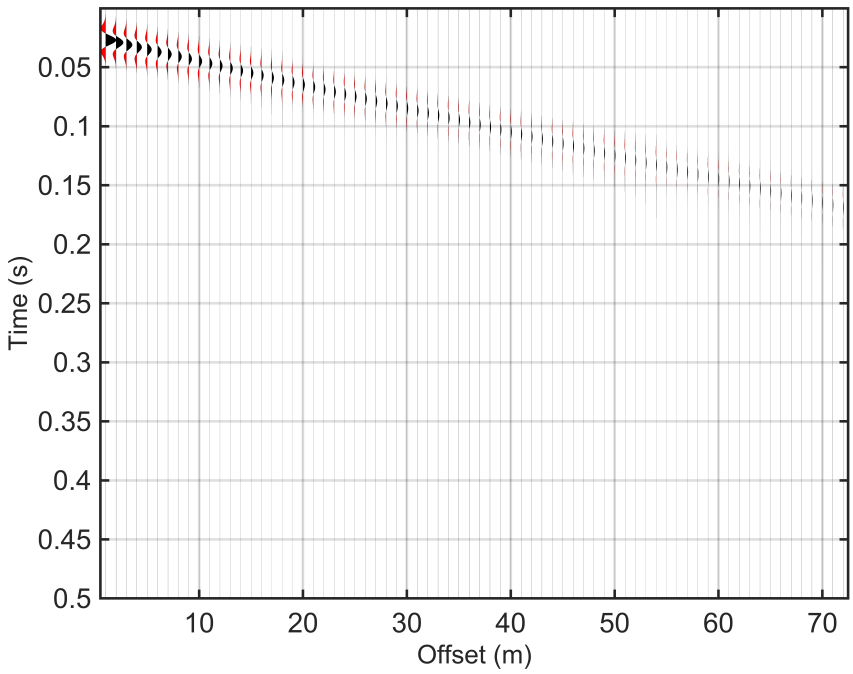


Figure 6.1: *3D analytical shot gather with a constant quality factor of $Q = 20$.*

The amplitude spectra of the analytical shot gather (Fig. 6.2a) identifies the dominant frequency of each trace and indicates a significant decrease in amplitude with increasing offset. The frequency band surrounding the dominant frequency is used to compute spectral ratios between various trace pairs, using the trace at a 10-meter offset as the reference (Fig. 6.2b). These amplitude spectral ratios decrease linearly, a behavior attributed to the use of a constant quality factor, Q.

To quantify this relationship, linear regression is applied to the spectral ratio between reference traces $x_1 = 5,\ 10,\ 40$ m and $x_2 = 70$ m offset, corresponding to a 65, 60, and 30 m distance (Fig. 6.2c, 6.2d, and 6.2e). The slope and its associated confidence bounds indicate highly consistent behavior, with an exceptionally low standard deviation. The Q

value estimated from the slope using (Eq. 2.60) in three cases with different distances between traces closely matches the constant Q used in the analytical solution, exhibiting a relative error of approximately 1.75% and minimal uncertainty in determining the slope 2.5 e^{-03}. The assumption that velocity c (Eq. 2.67) remains constant with frequency leads to this error.

This procedure is extended to multiple trace pairs using the 5-meter offset trace as a reference (Fig. 6.2f). For each pair, the Q value is calculated, and the median of these values is used to characterize attenuation across the shot gather. The results demonstrate consistent Q estimates across all pairs, yielding a median value of $Q = 20.3$ with a minimal standard deviation.

In a final test (workflow step 5), the analysis is repeated with every trace (1–72) serving sequentially as the reference trace. Again, the median Q values converge to $Q = 20.3$ for all reference traces. This uniformity leads to the definition of a global quality factor, $Q_{\text{Global}} = 20.3$, with negligible variance and uncertainty. The consistency of the results across all trace combinations reinforces the validity of the proposed method. Any observed discrepancies may stem from the omission of frequency-dependent velocity effects in the model, as suggested in (Eq. 2.67).

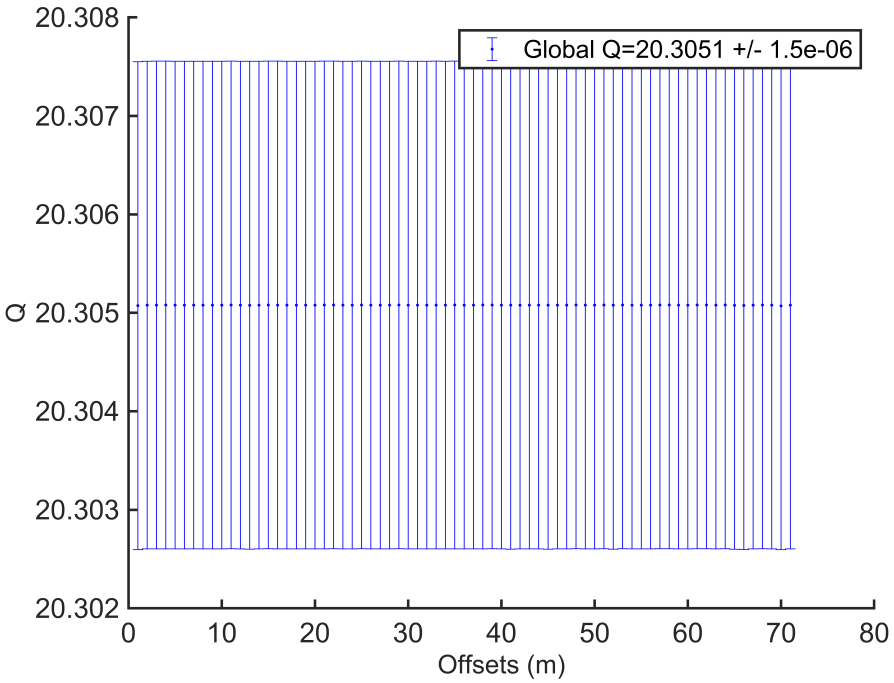
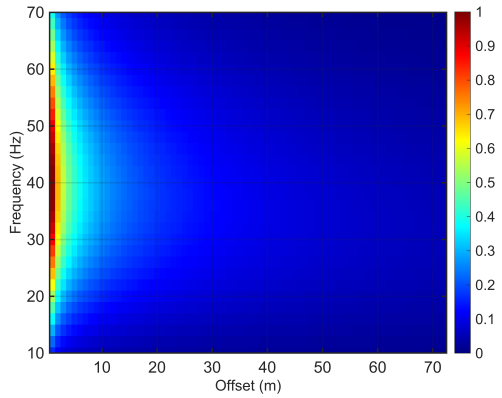
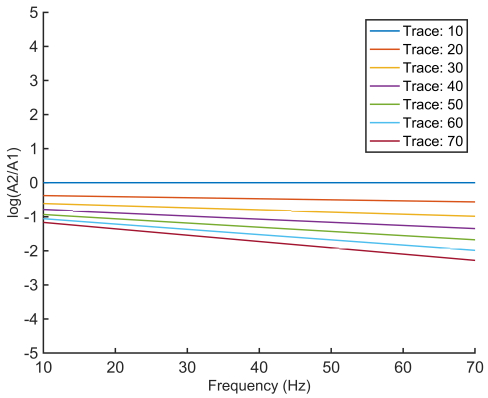


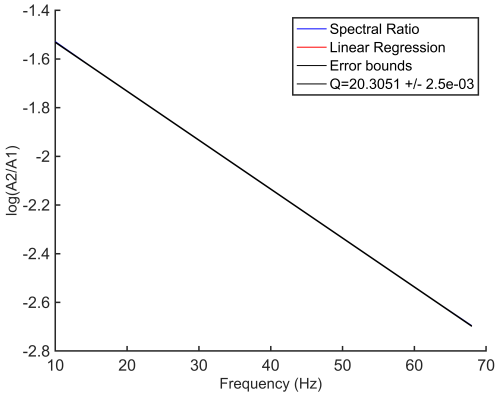
Figure 6.3: *Global Q value computed from all traces of the 3D analytical shot gather.*



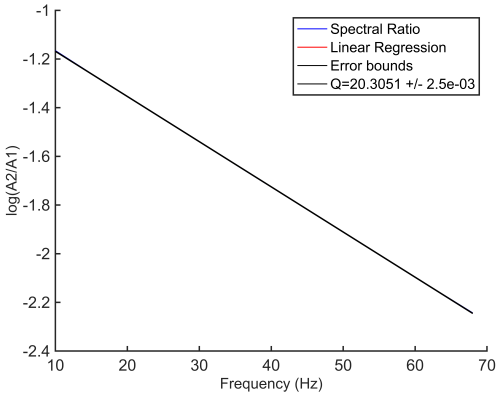
(a) Amplitude spectra



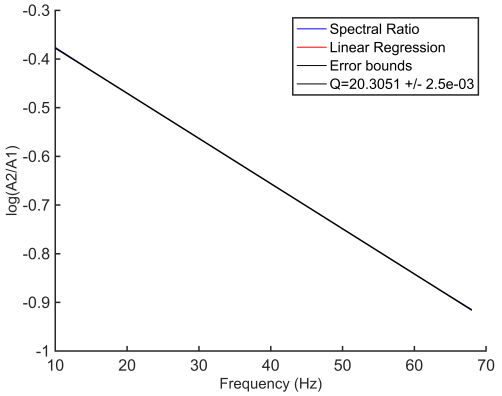
(b) Log-spectral ratios



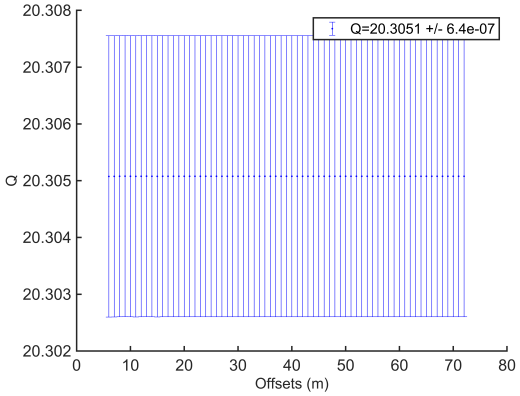
(c) Linear regressions x_1=5 m and x_2=70 m



(d) Linear regressions x_1=10 m and x_2=70 m



(e) Linear regressions x_1=40 m and x_2=70 m



(f) Q value using multiple trace pairs

Figure 6.2: *Results of the spectral ratio method applied to the 3D analytical solution of the acoustic wave equation with a constant quality factor ($Q = 20$): (a) amplitude spectra within the frequency range of 10–70 Hz; (b) log-spectral ratios for offsets of 10, 20, 30, 40, 50, 60, and 70 m; (c), (d), and (e) linear regressions applied to the log-spectral ratios corresponding to trace pairs for $x_1 = 5, 10, 40$ m and $x_2 = 70$ m; and (f) median Q values and associated median errors derived from multiple trace pairs using trace 5 as a reference.*

6.1.2 Applications on viscoelastic FD-modeled shot gather

Further testing on the workflow is presented in this section, applied to a viscoelastic finite-difference modeled shot gather using the inverted five-layer shear-velocity model from the Herrenknecht test site. The simulation assumes a homogeneous quality factor of $Q = 20$.

Viscoelastic modeling of seismic wave propagation in attenuative media captures the frequency-dependent amplitude decay and dispersion of seismic waves, consistent with their interaction in real rock formations. To model this behavior accurately, the quality factor Q must be treated as frequency-dependent. Therefore, a frequency-dependent Q approximation using varying numbers of relaxation mechanisms L was applied. Increasing L enhances the accuracy of the frequency-dependent approximation of Q.

For the Q approximation, an improved τ-method was employed (Blanch, 1996). The method is described in detail in Bohlen (1998).

Fig. 6.4 presents the results of the $Q = 20$ approximation derived using the τ-method with five relaxation mechanisms L, including their corresponding relaxation frequencies and τ values. These parameters are applied in the `SOFI2D` software to model viscoelastic shot gathers (see Fig. 6.5a). The relevant input parameters for `SOFI2D` are provided in Appendix A.

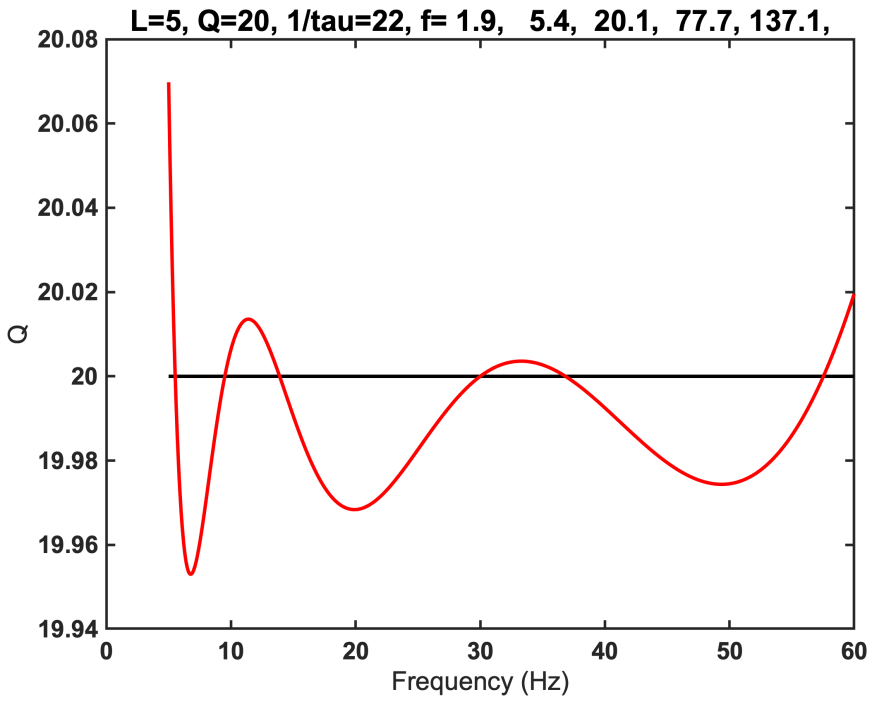


Figure 6.4: *Approximation of $Q = 20$ using five L-relaxation mechanisms and the corresponding relaxation frequencies.*

Fig. 6.5a shows the viscoelastic modeled shot gather generated using `SOFI2D`, assuming a homogeneous medium with an approximated quality factor of $Q = 20$ and five relaxation mechanisms. This modeled shot gather differs from the analytical one, exhibiting a more complex wavefield with distinct phases, including direct waves, P- and S-waves, as well as refracted and surface waves. To accurately estimate the Q value of surface (Rayleigh) wave, it is necessary to isolate them from other phases using a time-space window.

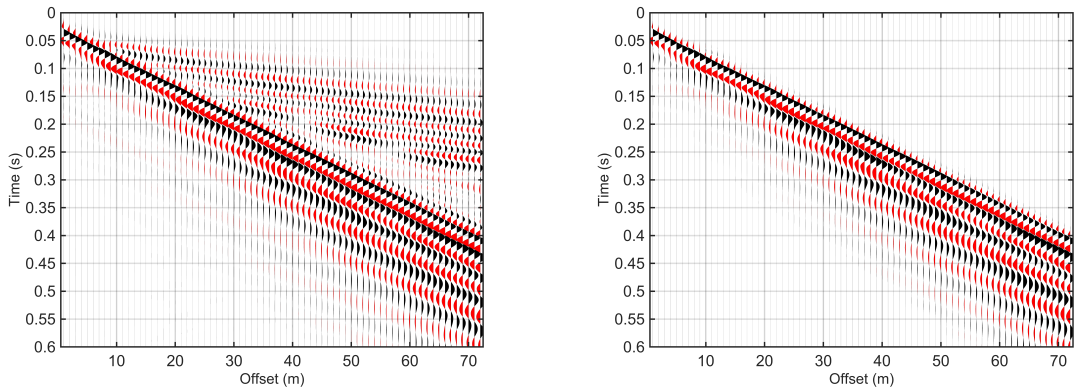
The same workflow described in section 6.1 is applied to the viscoelastic shot gather, now using the windowed data depicted in Fig. 6.5b. The amplitude spectra shown in Fig. 6.6a illustrates the dominant frequency content across the offset, which is concentrated in the 5–45 Hz range. This frequency band is used for subsequent analysis.

The spectral ratios shown in Fig. 6.6b illustrates behavior across the selected trace pairs. Linear regression is applied to the calculated spectral ratios between the chosen traces (Fig. 6.6c, 6.6d, and 6.6e). It is found that the reference trace with the longer offset yields results that more closely approximate the constant Q value used. The estimated Q value, illustrated in Fig. 6.6e, is determined to be 23.7, aligning more closely with the input value.

The multiple trace pairs were calculated using the 30 m reference trace instead of the 5 m trace, as traces with offsets close to the source exhibited high values. The calculated median Q value was 20.3 with a standard deviation of 12.03 (Fig. 6.6f). It is clear that Q values increase with increasing offset. However, this trend was neither linear nor exponential, displaying instead an oscillatory behavior. Traces in the 60–72 m range yielded $Q \approx 20$, which was consistent with the modeled input.

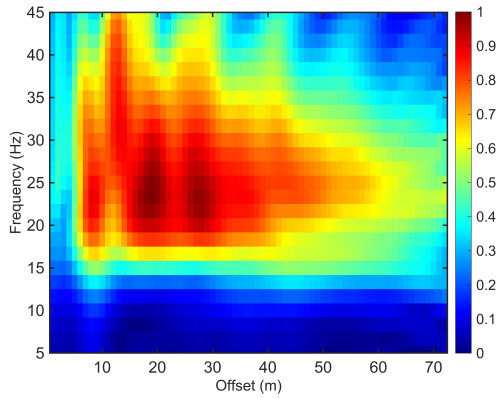
The global quality factor Q_{Global}, computed using all traces of winnowed data (Fig. 6.7a), is 20.8, with a 4% error and standard deviation of 10.94. Q_{Global} of non-windowed shot gather shows a higher value equal to 25.0 with a higher error of 25% (Fig. 6.7a). These results suggest that using a reference trace with a greater offset improves estimation accuracy, likely due to minimized near-field interference. Overall, the global Q value supports the reliability of the spectral ratio method and its applicability to real seismic data.

When all traces were used as references, the method performed well, and the global Q values exhibited high consistency, despite the poor quality of short-offset traces and the slightly high deviation observed for each trace used as a reference. Furthermore, the application of a window enhanced the accuracy of the estimation.

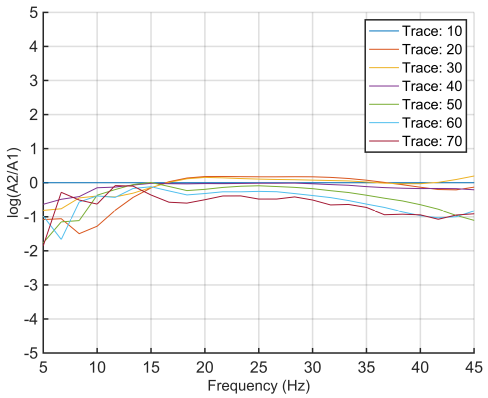


(a) *Without window* ***(b)*** *With window*

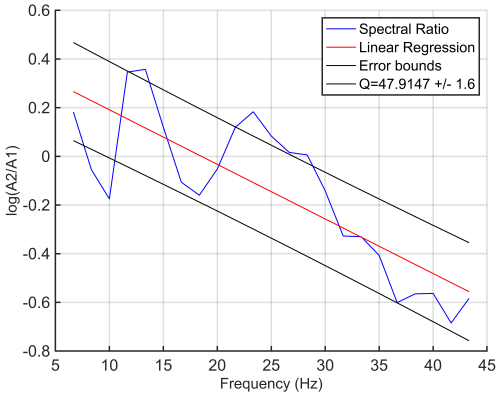
Figure 6.5: *Viscoelastic modeled shot gather with an approximated $Q = 20$: (a) without applying a window and (b) with a window applied to isolate the Rayleigh wave from other wave phases.*



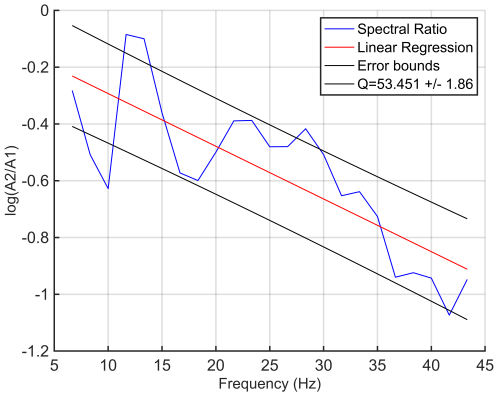
(a) *Amplitude spectra*



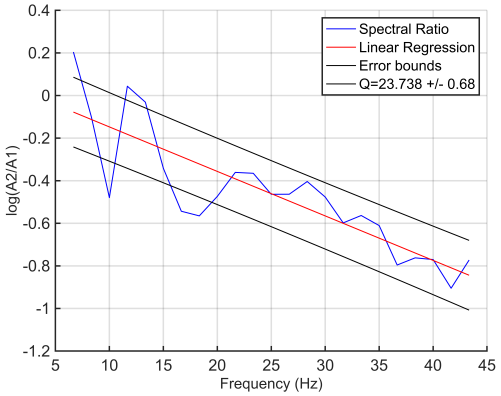
(b) *Log-spectral ratios.*



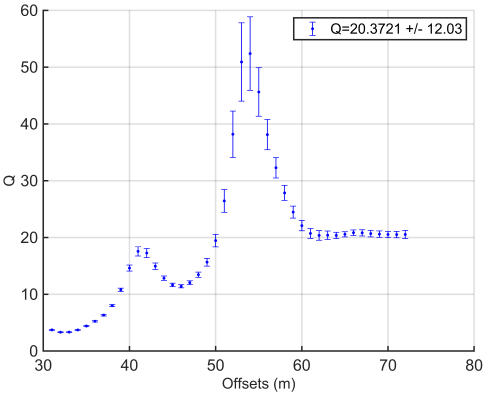
(c) *Linear regressions x1=5 m and x2=70 m.*



(d) *Linear regressions x1=10 m and x2=70 m.*

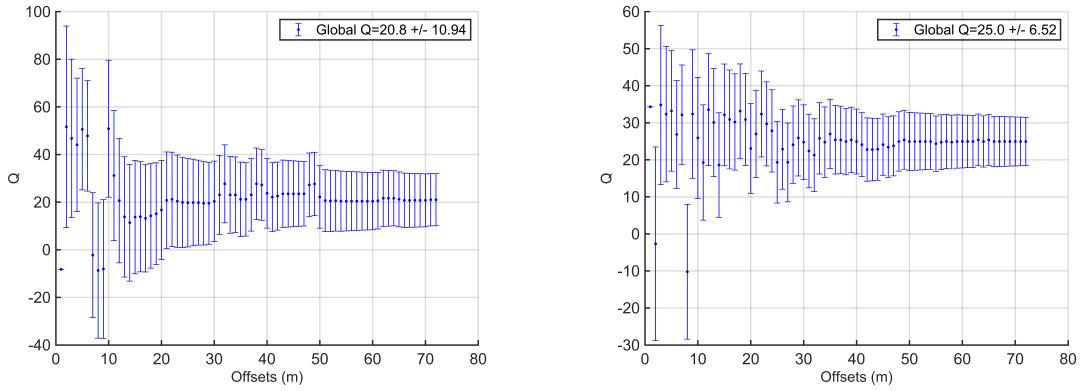


(e) *Linear regressions x1=40 m and x2=70 m.*



(f) *Q values using multiple trace pairs*

Figure 6.6: *Results of the spectral ratio method applied to windowed viscoelastic modeled shot gather with a homogeneous approximated quality factor ($Q = 20$). (a) amplitude spectra within the frequency range of 5–45 Hz; (b) log-spectral ratios for offsets of 10, 20, 30, 40, 50, 60, and 70 m; (c), (d), and (e) linear regressions applied to the log-spectral ratios corresponding to trace pairs for $x_1 = 5, 10, 40$ m and $x_2 = 70$ m; and (f) median Q values and associated median error derived from multiple trace pairs using trace 30 as reference.*



(a) With window *(b) Without window*

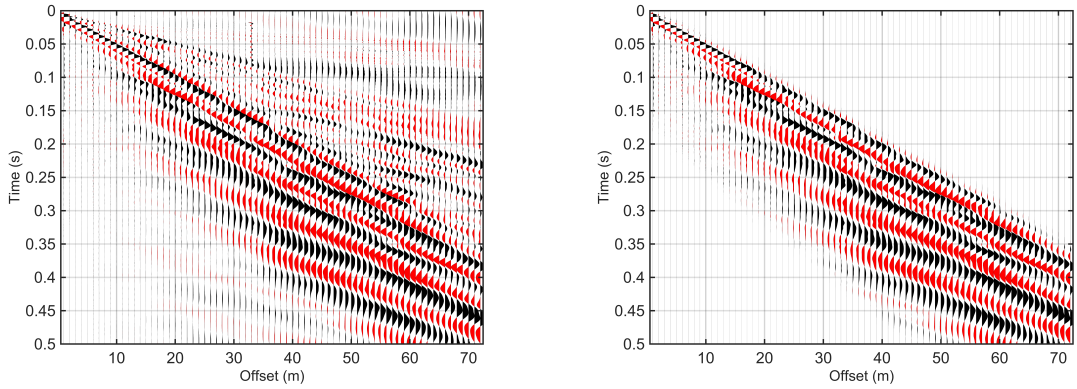
Figure 6.7: *Global Q value computed using all traces of viscoelastic modeled shot gather. (a) with applying a window; (b) without applying a window.*

6.1.3 Application on real data

In this section, the previously validated workflow (section 6.1 on page 59) is applied to field data acquired at the Herrenknecht test site, with the objective of estimating the Q factor of surface waves (Rayleigh). In the case with multiple trace pairs, traces on both sides of the reference trace are used, as it has been demonstrated that incorporating all traces yields acceptable results. An additional step is incorporated to compute the global Q value for each shot—using the first and second profiles individually—and to subsequently determine their respective global medians.

It is important to highlight that, unlike analytical or numerically simulated (viscoelastic) shot gathers, real seismic data exhibit substantially greater complexity. These datasets encompass multiple wave phases and are affected by ambient and instrumental noise, which significantly impacts the performance and reliability of the spectral ratio method.

Fig. 6.8 presents shot 1 before and after the application of a selective time window. This windowing is based on a constant phase velocity of $c = 200$ m/s—estimated from the dispersion image—and is applied independently of frequency to isolate the Rayleigh wave.



(a) Without window *(b) With window*

Figure 6.8: *Shot 1 from field data. (a) shows the data without applying a window; (b) displays the result after applying a window to isolate the Rayleigh wave from other seismic phases.*

Fig. 6.9a displays the amplitude spectra within the analyzed frequency range. Higher amplitudes are observed between 40 Hz and 120 Hz at short offsets, while a dominant low-frequency component around 15 Hz is evident across nearly the entire offset range. Fig. 6.9b illustrates significant fluctuations in the spectral ratio across trace pairs over the frequency range; however, the data generally exhibit a decreasing trend.

Fig. 6.6c, 6.6d, and 6.6e present the result of linear regression: the slope decreases and the quality factor increases with increasing the offset, opposite what is observed in the modeled case. Fig. 6.9f shows the results obtained using multiple traces with trace at 30 m offset as the reference. At short offsets, the estimated Q values are consistent. However, at longer offsets, the Q values vary significantly, in some cases reaching values as high as 400. The median Q value obtained from multiple traces is $Q = 17.9$, with a high standard deviation of 78.04 due to some high values.

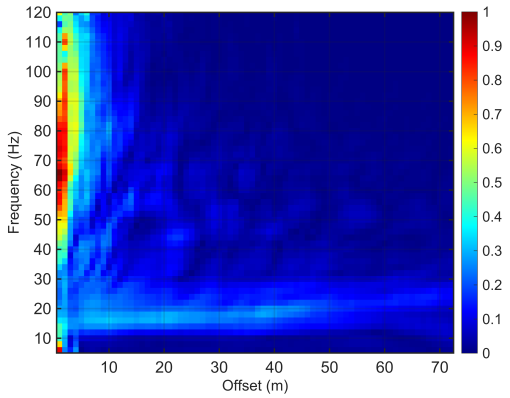
Fig. 6.10a summarizes the Q values derived from all traces of shot 1. Although several traces exhibit high deviations, the Q values remain generally consistent; these strong deviations may be attributed to noise and wave interference. The global Q value for shot 1 is $Q_{\text{Global}} = 17.7$, with standard deviation of 5.38. Without applying a window, it leads to slightly increase in the Q values and their deviation (Fig. 6.10b).

Fig. 6.10c presents the Q values for shot 10, computed using all traces at both positive and negative offsets. The Q values at negative offsets exhibit low variability and deviation, whereas those at positive offsets show higher values and greater deviation. This discrepancy may suggest that the left side of the first profile experiences higher and more uniform attenuation, while the right side is characterized by lower attenuation and more pronounced variability in the Q values. The global quality factor calculated across both sides is $Q_{\text{Global}} = 11.8$. Without applying a window, it leads also to slightly increase in the Q value (Fig. 6.10d).

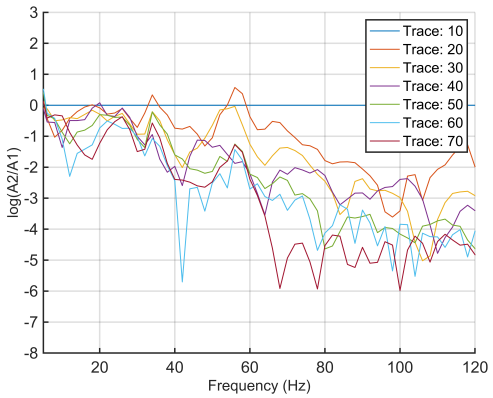
To estimate the global Q values in the first and second profiles, the global Q was calculated for each shot, and the median and associated deviation were then determined. As shown in Fig. 6.11a, the Q values from shots 1 to 20 in the first profile lie between 11 and 24. Notably, the shot acquired near the center of the profile exhibits a slightly lower Q value compared to those acquired at the edges. Shot 2 exhibited a significantly higher deviation compared to the other shots. Interestingly, the first and last shots (1 and 20) yield nearly identical global Q values, supporting the validity and robustness of the applied method. The global median Q for the first profile is 14.9, with standard deviation of 3.59.

The global Q values for the second profile, as shown in Fig. 6.11b, exhibit a similar pattern and nearly identical range, between 11 and 20. The global median Q is 13, with standard deviation of 2.89.

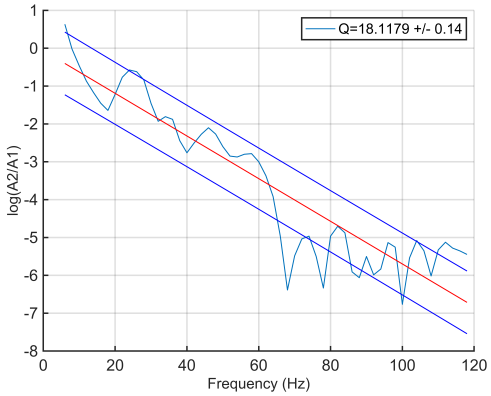
Using the empirical relations described in section 2.4, the shear-wave quality factor (Q_S) and the compressional-wave quality factor (Q_P) were estimated. Table 6.1 summarizes the results of the seismic investigation, including the 1D V_S profiles and the quality factors estimated at the Herrenknecht test site.



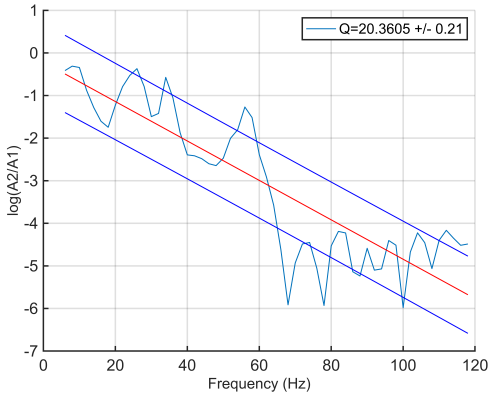
(a) Amplitude spectra



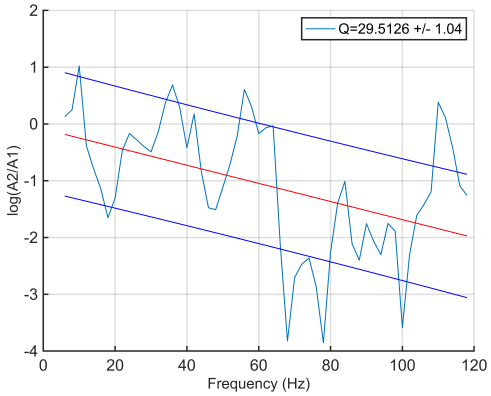
(b) Log-spectral ratios



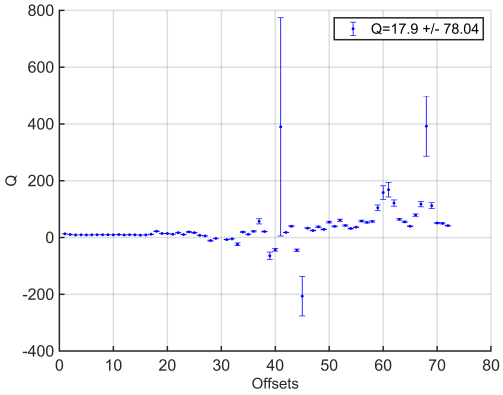
(c) Linear regressions x1=5 m and x2=70 m.



(d) Linear regressions x1=10 m and x2=70 m.

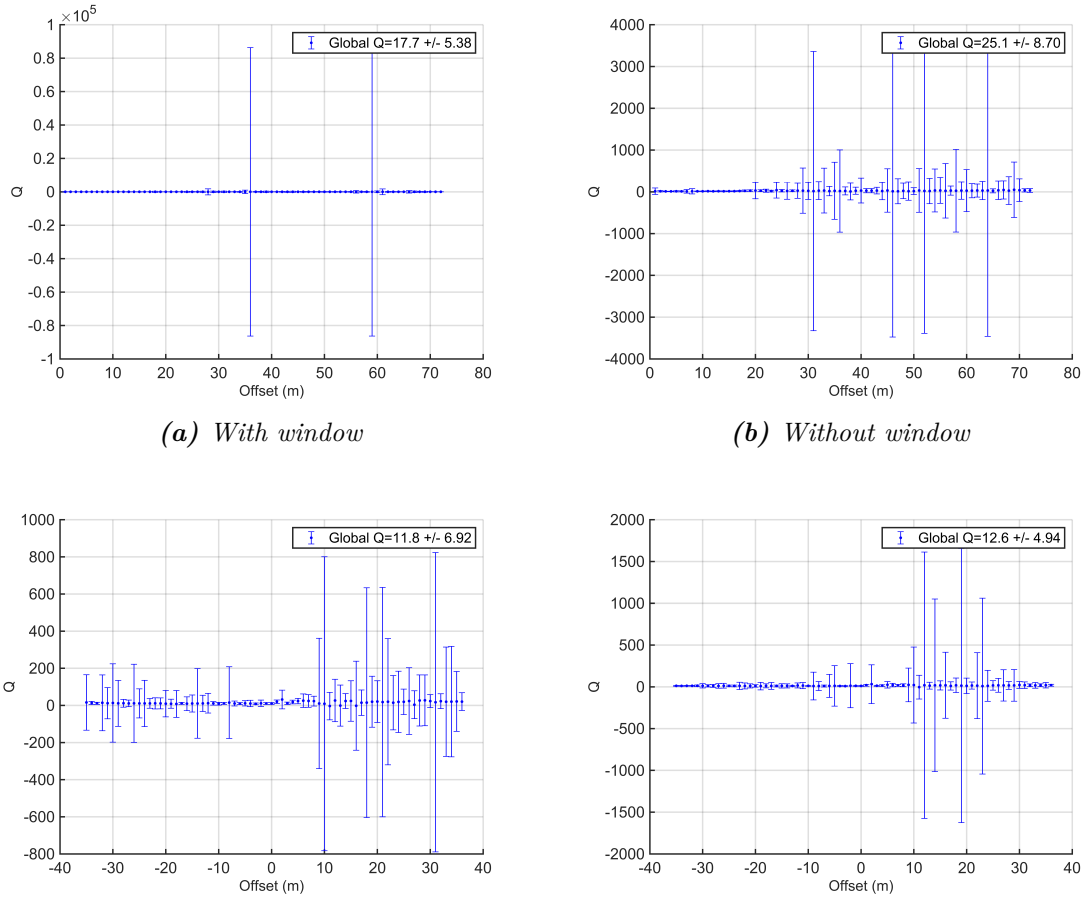


(e) Linear regressions x1=40 m and x2=70 m.



(f) Q value using multiple trace pairs

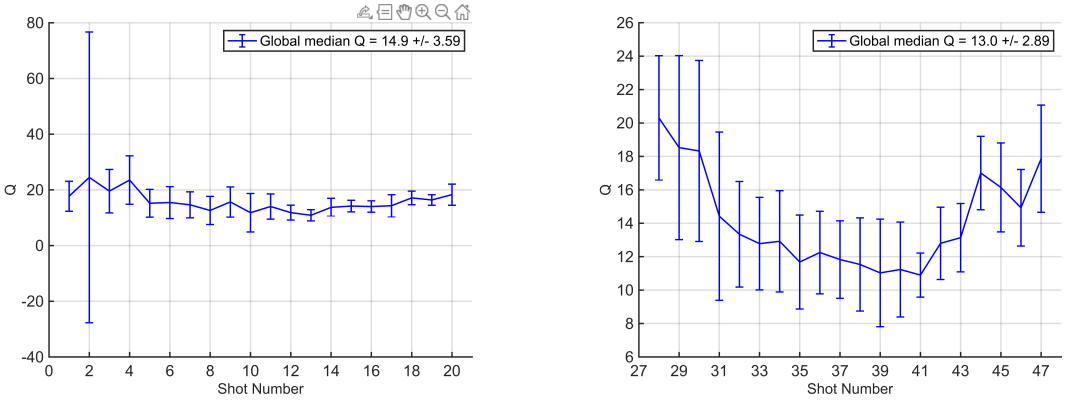
Figure 6.9: *Results of the spectral ratio method applied to field data shot 1, with a source offset of 1 m: (a) amplitude spectra within the frequency range of 5–120 Hz; (b) log-spectral ratios computed for offsets of 10, 20, 30, 40, 50, 60, and 70 m; (c), (d), and (e) linear regressions applied to the log-spectral ratios corresponding to trace pairs for* $x_1 = 5, 10, 40$ *m and* $x_2 = 70$ *m; and (f) median Q values and associated median error derived from multiple trace pairs using trace 30 as reference.*



(a) *With window* ***(b)*** *Without window*

(c) *With window* ***(d)*** *Without window*

Figure 6.10: *Global Q values computed from field data using all traces for: (a) windowed shot 1; (b) non-windowed shot 1; (c) windowed shot 10; and (d) non-windowed shot 10.*



(a) *First profile.* ***(b)*** *Second profile.*

Figure 6.11: *Global Q value for the first and second profiles.*

Table 6.1: *Inversion model parameters for the first and second profiles (P1 and P2), along with the estimated quality factors of Rayleigh wave (Q), S-wave (Q_S), and P-wave (Q_P).*

	First profile		**Second profile**		**Total median**	
Layer	z (m)	β (m/s)	z (m)	β (m/s)	z (m)	β (m/s)
1	0.1	249.1	0.1	166.9	0.1	208.0
2	0.5	190.4	0.6	300.9	0.6	245.6
3	1.8	217.4	2.4	185.8	2.1	201.6
4	5.2	191.2	5.1	193.6	5.1	192.4
5	15.4	342.6	16.0	363.9	15.7	353.2
6	∞	564.5	∞	651.4	∞	607.9

P1: $Q_S \approx Q = 14.9$, $Q_P = 29.8$; P2: $Q_S \approx Q = 13$, $Q_P = 26$

6.2 Discussion

The spectral ratio method has been tested and confirmed using analytical solutions for both single trace pairs and all traces together, showing very little error. This minimal error arises from the assumption that the phase velocity c is constant over frequency; however, in practice, its value is frequency-dependent. Synthetic data modeled with a constant Q value have produced reliable results, provided certain conditions are met.

A temporal window has been applied to isolate the Rayleigh phase from other interfering phases, thereby minimizing their influence and allowing the attenuation of a single phase to be observed. The optimal frequency range—within which the log-spectral ratio exhibits a monotonic decrease—has been identified.

When a single trace pair is utilized, it is preferable for the reference trace to be located at a far offset from the source to mitigate near-field effects. In general, the use of all available traces has yielded favorable outcomes, despite variations in the short-offset values and a high standard deviation in some traces. The approach can be extended to field data.

Real seismic data have been found to introduce additional complexities due to the non-ideal behavior of wave phases, which deviate from those modeled synthetically as a result of assumptions in the homogeneous, linear elastic model. Moreover, noise present in real data affects the accuracy of the spectral ratio method, and wave interference can lead to significant deviations in some traces; however, the estimated Q values generally exhibit high consistency. Nevertheless, the same guidelines—particularly those concerning the appropriate frequency range—must be adhered to to avoid intervals contaminated by background noise, where the amplitude in the log-spectral ratio increases.

Measurements from the first and last shots of the first profile produced nearly identical values, providing strong evidence that the method is functioning correctly.

Chapter 7

Summary

In this thesis, the objective is seismic investigation of the subsurface structure at the Herrenknecht test site, where the signal of an urban vibration truck, developed by the Herrenknecht company, is to be validated. For the validation process, the test site must be as laterally homogeneous as possible to isolate the subsurface's effects on the signal from other influences generated by the vibrator.

As a first step, a 1D shear-wave velocity profile V_S is constructed. To build the profile, multichannel analysis of surface waves (MASW) is employed. MASW exploits the dispersion characteristics of Rayleigh waves, which are sensitive to shear-wave velocity and depth.

For data processing, the open-source software `MASWaves` is utilized. The MASW procedure involves three steps: First, data acquisition was carried out along two perpendicular profiles, each consisting of 20 shots at 4 m intervals, with a receiver spread length of 72 m and 1 m receiver spacing. Second, dispersion curves were extracted from all shot records. Third, inversion was applied to all picked dispersion curves under the assumption of a five-layer, linear-elastic, homogeneous model to derive the V_S profile for each shot. Subsequently, the median shear-wave velocity for each profile and the overall median were calculated.

The 1D V_S profiles derived from the first profile's shots show strong variation in the shallow subsurface (up to 2 m), in contrast to the second profile, which exhibits less variation in shear-wave velocity along its length. The seismograms from the first profile also display significant waveform variability from shot to shot. Below 2 m, however, both median V_S profiles from the first and second profiles demonstrate high similarity in velocity and layer thickness.

The assumption of a laterally homogeneous test site is invalidated for the first 2 m due to variations in fill material, as confirmed by site photographs and the known limitations of MASW in accurately resolving very shallow layers. The shallow subsurface, up to a depth of 2 m, could better investigated and more accurately characterized using other geophysical methods, such as ground-penetrating radar (GPR). A comparison between observed and synthetic data—generated using the inverted shear-wave velocity profiles—reveals non-identical waveforms in the left-side shots of both profiles. However, greater similarity is observed in the final shots of each profile, and the dispersion images exhibit consistent patterns in the low-frequency range.

The second part of the investigation involved estimating the seismic quality factor Q (attenuation) of the test site using all traces from each shot along both profiles. A global Q value was determined for each profile using the spectral ratio method. Initially, the method was validated through the analytical solution of an acoustic wave. Subsequently,

the test was extended to synthetic shot gather generated from the inverted shear-wave velocity profile. These results showed agreement under appropriate conditions, including the correct frequency range and the application of time windows to isolate desired seismic phases.

Application of the method to real data produced favorable results, although it posed challenges due to noise and wave interference.

Appendix A

Software

A.1 MASWaves [Version 1, 07.2017]

- **MASWaves Dispersion**
  - MASWaves_read_data.m
  - MASWaves_plot_data.m
  - MASWaves_dispersion_imaging.m
  - MASWaves_plot_dispersion_image_2D.m
  - MASWaves_plot_dispersion_image_3D.m
  - MASWaves_extract_dispersion_curve.m
  - MASWaves_plot_dispersion_curve.m

- **MASWaves Inversion**
  - MASWaves_Ke_layer.m
  - MASWaves_Ke_halfspace.m
  - MASWaves_stiffness_matrix.m
  - MASWaves_theoretical_dispersion_curve.m
  - MASWaves_misfit.m
  - MASWaves_plot_theor_exp_dispersion_curves.m
  - MASWaves_inversion.m

- **Own Functions**
  - Dispersion_Imaging_Picking.m
  - Inversion_Script.m
  - Myfun_misfit.m

A.2 Q__estimation

- Q_approximation.m
- analytical_shotgather.m
- Q_Analysis_of_Field_Data.m

```
%% Q-approximation using the improved tau-method (Blanch et al., 1995)

close all          % Close all figure windows
clear all          % Clear all variables from the workspace

global L w Qf1     % Declare global variables used across main script and function

%-------------------------INPUT PARAMETERS----------------------------

Q = [20.0];         % Target constant Q-value to approximate
Q0 = Q(1);          % Initial Q value

fp1 = 5.0;          % Lower frequency bound [Hz]
fp2 = 60;           % Upper frequency bound [Hz]
df = 0.1;           % Frequency resolution [Hz]

f0 = 30;            % Reference frequency [Hz]

% Define the number of relaxation mechanisms (L) and their characteristic frequencies (fl)
% Uncomment one of the following as needed:
% L=1; fl=[f0];
% L=2; fl=[f0/5 2*f0];
% L=3; fl=[f0/100 f0/5 2*f0];
% L=4; fl=[f0/10 f0/2 2*f0 6*f0];
L = 5; fl = [f0/20 f0/10 f0/2 2*f0 6*f0];  % 5-term approximation used

tau_st = 1.0 / Q0;  % Initial guess for tau (1/Q)

optim = 1;          % Flag to enable optimization (1 = optimize tau and fl)

%-------------------------END INPUT PARAMETERS-----------------------

f = fp1:df:fp2;         % Frequency array
w = 2 * pi * f;         % Angular frequency array

Qf1 = Q(1) + f*0;       % Define target Q as constant over frequency (Q(f) = Q0)

% Save initial guess values
fl_st = fl;
x0 = [fl_st tau_st];  % Initial vector for optimization: [frequencies, tau]

% Perform optimization using nonlinear least squares
if optim
    [x] = lsqnonlin('qflt', x0);  % Optimize fl and tau to fit Q
    fl_opt = x(1:L);              % Optimized relaxation frequencies
    tau_opt = x(L+1);             % Optimized tau
else
    fl_opt = fl_st;               % Use initial guesses if optimization disabled
    tau_opt = tau_st;
    x = x0;
end

% Analytical computation for new tau using optimized relaxation frequencies
a = f0 ./ fl_opt;
B = sum(a ./ (1 + a.^2));
A = sum((a.^2) ./ (1 + a.^2));
tau_new = 1.0 ./ (Q * B - A);     % Updated tau after fitting

% Compute approximated Q using the Generalized Standard Linear Solid model
for nQ = 1:length(Q)
    ts = 1 ./ (2 * pi * fl_opt);  % Relaxation times from optimized frequencies
    t = tau_new(nQ);              % Updated tau

    sumzQ = 0; sumnQ = 0;         % Initialize sums for Q computation

    for l = 1:L
        d = 1 + (w.^2) * ts(l)^2;
        sumnQ = (w * ts(l) ./ d) + sumnQ;
```

```
        sumzQ = ((w.^2) * ts(l)^2 ./ d) + sumzQ;
    end

    Qfa(nQ,:) = (1 + t * sumzQ) ./ (t * sumnQ);  % Approximated Q over frequency
end

%-------------------------PLOTTING RESULTS----------------------------

figure; hold on;

QI = Q;     % Plot constant Q
QfaI = Qfa; % Plot approximated Q

for nQ = 1:length(Q)
    plot(f, QI(nQ) + f*0, 'k-', 'linewidth', 2.0);   % Plot target Q (black line)
    plot(f, QfaI, 'r-', 'linewidth', 2.0);           % Plot fitted Q (red line)
end

xlabel('Frequency [Hz]');
ylabel('Q');
title(['L=',num2str(L),' Q=',num2str(Q),...
       ' 1/tau=',num2str(1.0./tau_new,'%.0f,'),...
       ' f= ',num2str(x(1:L),' %.1f,')]);

% Customize plot appearance
ax = gca;
ax.XAxis.FontSize = 12;
ax.XAxis.FontWeight = 'bold';
ax.YAxis.FontSize = 12;
ax.YAxis.FontWeight = 'bold';
ax.XLabel.FontSize = 12;
ax.YLabel.FontSize = 12;

set(gca, 'Linewidth', 2.0);
set(gca, 'Box', 'on');

% Save figure as JPEG
printfile = ['Fig/QapproxQ8Q20.jpg'];
print(gcf, '-djpeg', printfile);

%---------------------AUXILIARY FUNCTION----------------------------

% This function computes the error between the model Q(f)
% and the target Q(f) for optimization via least squares
function delta = qflt(x)
    global L w Qf1 Qf2

    fl = x(1:L);           % Extract relaxation frequencies
    t = x(L+1);            % Extract tau

    ts = 1 ./ (2 * pi * fl);  % Relaxation times

    sumzQ = 0; sumnQ = 0;
    for l = 1:L
        d = 1 + w.^2 * ts(l)^2;
        sumnQ = (w * ts(l) * t ./ d) + sumnQ;
        sumzQ = (w.^2 * ts(l)^2 * t ./ d) + sumzQ;
    end

    Qf2 = (1 + sumzQ) ./ sumnQ;             % Model Q(f)
    delta = (1 ./ Qf2) - (1 ./ Qf1);        % Objective function: difference in inverse Q
end
```

```
% Create analytic shot gathers in 2D and 3D with attenuation
% Based on constant-Q attenuation (Kjartansson, 1979 model)

close all; clear all;              % Close all figures and clear workspace
addpath ../SegyMAT -begin          % Add path to SegyMAT toolbox for SEG-Y I/O

% Parameters
dt = 0.00002;                      % Sampling interval (s)
ns = 25000;                        % Number of samples per trace
fc = 40.0;                         % Central frequency of Ricker wavelet (Hz)
c0 = 500.0;                        % Reference wave velocity (m/s)
Q0 = 20.0;                         % Constant quality factor Q

%tshift = dt * ns / 3.0;           % Optional time shift (commented out)
```

```
tshift = 0.0;                       % No time shift
offsets = 1:1:72;                   % Receiver offsets (1 to 72 units)

% Output file names
file3D = "su/analytic/3DQ20.su";    % Output 3D SU file
file2D = "su/analytic/2DQ20.su";    % Output 2D SU file
filetmp = "tmp.sgy";                % Temporary SEG-Y file

% Time vector
t = (1:ns) * dt;

% Generate Ricker wavelet
s = ricker(t, fc, 0.0);             % Ricker wavelet with peak at t=0

% Compute Fourier Transform of wavelet
[S, f] = fast_fourier_transform(s, dt, 2);   % FFT and frequency axis
w = 2.0 * pi * f;                   % Angular frequency vector
w0 = 2.0 * pi * fc;                 % Central angular frequency

% Kjartansson (1979) constant-Q model:
% c(w) = c0 * (|w/w0|)^gamma, where gamma = atan(1/Q)/pi
gamma = atan(1.0 / Q0) / pi;
c = c0 * (abs(w / w0)) .^ gamma;    % Frequency-dependent velocity

% Handle Nyquist frequency component to avoid discontinuities
c(ns/2 + 1) = (c(ns/2 + 2) + c(ns/2)) / 2.0;

% Attenuation coefficient alpha(w)
alpha = tan(pi * gamma / 2.0) .* abs(w) ./ c;

% Plot phase velocity as function of frequency
figure;
plot(f, c);
xlim([-100 100]);
title('Phase Velocity c(f) under Kjartansson Q Model');
xlabel('Frequency (Hz)');
ylabel('Velocity (m/s)');

% Compute complex wavenumber: k = w / c(w)
k = w ./ c;

% Loop over offsets to synthesize analytic shot gathers
for n = 1:length(offsets)
    R = offsets(n);                 % Current offset
    I3D = 1.0 / R;                  % Geometric spreading (3D)
    I2D = sqrt(2.0 * pi ./ (k * R));  % Geometric spreading (2D, cylindrical)

    % Correct the Nyquist component for 2D
    I2D(ns/2 + 1) = (I2D(ns/2 + 2) + I2D(ns/2)) / 2.0;

    % Add phase delay: exp(-i*k*R)
    I3D = I3D .* exp(-1i * k * R);
    I2D = I2D .* exp(-1i * k * R) .* exp(-1i * pi / 4);  % 2D extra phase shift

    % Attenuation filter D(w) = exp(-R * alpha(w))
    D = exp(-R * alpha);

    % Apply attenuation to frequency responses
    I3D = I3D .* D;
    I2D = I2D .* D;

    % Apply propagation effects to source spectrum
    S3D = S .* I3D;
    S2D = S .* I2D;

    % Inverse FFT to time domain
    Data3D(:, n) = real(ifft(ifftshift(S3D)));
    Data2D(:, n) = real(ifft(ifftshift(S2D)));
end

% Normalize each trace in 3D gather
for trace = 1:length(offsets)
    Data3Dn(:, trace) = Data3D(:, trace) / max(abs(Data3D(:, trace)));
end

% Normalize each trace in 2D gather
for trace = 1:length(offsets)
```

```
    Data2Dn(:, trace) = Data2D(:, trace) / max(abs(Data2D(:, trace)));
end

% Plot 3D shot gather
figure;
wiggle(offsets, t, Data3Dn, 'VA2', 1);
title('3D Analytic Shot Gather with Attenuation');

% Plot 2D shot gather
figure;
wiggle(offsets, t, Data2Dn, 'VA2', 1);
title('2D Analytic Shot Gather with Attenuation');

% Write 3D data to temporary SEG-Y file
WriteSegy(filetmp, Data3D);

% Read SEG-Y for header manipulation
[Data, SegyTraceHeaders, SegyHeader] = ReadSegy(filetmp);

% Update SEG-Y headers
SegyHeader.dt = dt;
for n = 1:length(offsets)
    SegyTraceHeaders(n).dt = dt * 1.0e6;         % Time step in microseconds
    SegyTraceHeaders(n).offset = offsets(n);     % Store offset
end

% Write SU structures for 3D and 2D gathers
WriteSuStructure(file3D, SegyHeader, SegyTraceHeaders, Data3D);
WriteSuStructure(file2D, SegyHeader, SegyTraceHeaders, Data2D);
```

```
%% --- Q-Analysis of Field Data---
close all; clear all;  % Close all figures and clear workspace
addpath ../SegyMAT -begin  % Add SEG-Y reading tools to the path

% Loop through multiple shot files
for shot_num = 1
    % Construct file name dynamically for each shot
    filesu = sprintf('Path_to Su_Files', shot_num);
    fprintf('Processing Shot %d: %s\n', shot_num, filesu);  % Display shot being processed

    % Generate plot title based on shot number
    [~, name, ~] = fileparts(filesu);
    shot_num = str2double(name);
    titletxt = sprintf('Observed Shot %d', shot_num);

    %% Parameters
    itr = 1:72;                % Selected trace indices
    its = 5;                   % Resample: use every 'its' sample
    tracenorm = 1;             % Normalize individual traces
    xcur = 1.0;                % Amplitude scaling
    plottraces = 1;            % Toggle wiggle plot
    plotamplitudespectrum = 1; % Toggle amplitude spectrum plot
    spreadcorr = 1;            % Apply geometric spreading correction
    fp1 = 5.0; fp2 = 120.0;    % Frequency band
    timewindow = 1; ca = 200.0; t01 = 0.01; tw1 = 0.15; s1 = 0.01; % Tapering window params
    ShowSpectralRatios = 1;    % Toggle spectral ratio plotting
    Showpfspectrum = 0;        % Toggle slowness-frequency spectrum
    LinearRegression = 1;      % Toggle Q-estimation using linear regression
    QMultiOffset = 1;          % Toggle Q estimation across multiple offsets
    Qcall = 1;

    %% Load SU Data
    [Data, SuTraceHeaders, SuHeader] = ReadSu(filesu);
    ns = SuHeader.ns / its;
    dt = its * SuHeader.dt * 1e-6;
    t = linspace(dt, ns * dt, ns);  % Time axis

    num_trace = [SuTraceHeaders.TraceNumber];
    offset = [SuTraceHeaders.offset];
    ntr = length(num_trace);

    %% Select Traces
    if itr > 0
        Dataw = Data(1:its:ns*its, itr);  % Downsample data
        offsetw = offset(itr);            % Corresponding offsets
    end
    Dataw = Dataw / max(max(Dataw));      % Global normalization
```

```
    %% Apply Time Taper
    if timewindow
        maxoffset = abs(max(offsetw));
        for trace = 1:length(offsetw)
            t0 = t01 + abs(offsetw(trace)) / ca;
            tw = tw1 + (tw1 * abs(offsetw(trace)) / maxoffset);
            w = W(t0, tw, s1, t);
            Dataw(:, trace) = Dataw(:, trace) .* w';  % Apply taper window
        end
    end

    %% Spreading Correction
    if spreadcorr
        for trace = 1:length(offsetw)
            Dataw(:, trace) = Dataw(:, trace) .* sqrt(abs(offsetw(trace)));
        end
    end

    %% Trace Normalization
    if tracenorm
        for trace = 1:length(offsetw)
            Datawn(:, trace) = Dataw(:, trace) / max(abs(Dataw(:, trace)));
        end
    else
        Datawn = Dataw;
    end

    %% Wiggle Plot of Traces (Optional)
    if plottraces
        figure()
        wiggle(offsetw, t, Datawn, 'VA2', 1 / xcur)
        xlabel('Offset (m)'); ylabel('Time (s)');
        xlim([min(offsetw)-0.5, max(offsetw)+0.5]); ylim([0, 0.5]);
        grid on
        exportPublicationFigure(sprintf('wiggle_shot%d', shot_num), gcf);
    end

    %% FFT and Amplitude Spectrum
    [DataF, f] = fast_fourier_transform(Dataw, dt, 1);
    for trace = 1:length(offsetw)
        DataA(:, trace) = abs(DataF(:, trace));
        if max(DataA(:, trace)) > 0
            DataAn(:, trace) = DataA(:, trace) / max(DataA(:, trace));
        end
    end
    DataAmean = mean(DataAn, 2);
    DataA = DataA / max(max(DataA));

%% Amplitude Spectrum Plot (Optional)
    if plotamplitudespectrum
        figure()
        imagesc(offsetw, f', DataA);
        axis xy; colormap('jet'); colorbar;
        caxis([0, 1]);
        xlabel('Offset (m)'); ylabel('Frequency (Hz)');
        axis([min(offsetw)-0.5, max(offsetw)+0.5, fp1, fp2])
        grid on
        exportPublicationFigure(sprintf('AmpSpectrum - Real Data shot%d', shot_num));
    end

%% Spectral Ratios
    if ShowSpectralRatios
        SR = zeros(size(DataA));
        traceref = 10;  % Reference trace
        figure; hold on
        n = 1;
        for trace = 10:10:length(offsetw)
            if sign(offsetw(traceref)) == sign(offsetw(trace))
                if abs(offsetw(trace)) > abs(offsetw(traceref))
                    SR(:, trace) = log(DataA(:, trace) ./ DataA(:, traceref));
                else
                    SR(:, trace) = log(DataA(:, traceref) ./ DataA(:, trace));
                end
                plot(f, SR(:, trace), 'linewidth', 1.0);
                l(n) = trace; n = n + 1;
            end
```

```
        end
        xlabel('Frequency (Hz)'); ylabel('log(A2/A1)');
        axis([fp1, fp2, -8, 3]); grid on
        legend(arrayfun(@(x) ['Trace: ', num2str(x)], 1, 'UniformOutput', false));
        hold off
        exportPublicationFigure(sprintf('SpectralRatio - Real Data shot%d', shot_num));
    end

%% Linear Regression to Estimate Q
    if LinearRegression
        % Repeat for multiple trace pairs
        traceref=5; trace2=70;
            if sign(offsetw(traceref)) == sign(offsetw(trace2))
                k = find((f > fp1) & (f < fp2)); fm = f(k);
                if abs(offsetw(trace2)) > abs(offsetw(traceref))
                    SRm = log(DataA(k', trace2) ./ DataA(k', traceref));
                else
                    SRm = log(DataA(k', traceref) ./ DataA(k', trace2));
                end
                figure; hold on
                plot(fm, SRm, 'linewidth', 1.0);
                [p, S] = polyfit(fm, SRm, 1);
                [SRr, delta] = polyval(p, fm, S);
                plot(fm, SRr, 'r-', fm, SRr+delta, 'b-', fm, SRr-delta, 'b-', 'linewidth', 1.0)
                    ;
                slope = p(1);
                residuals_std = std(SRm - (slope * fm + p(2)));
                slope_std_error = residuals_std / sqrt(sum((fm - mean(fm)).^2) * (length(fm) -
                    1));
                dx = abs(offsetw(trace2) - offsetw(traceref));
                Q = -pi * dx / (ca * slope);
                Qerror = slope_std_error * (pi * dx / (ca * slope^2));
                legend(['Q = ', num2str(Q, '%.1f'), ' +/- ', num2str(Qerror, '%.2f')]);
                grid on
                exportPublicationFigure(sprintf('Linearregression - Real Data shot%d_ref%d',
                    shot_num, traceref));
            end
        end

%% Estimate Q at Multiple Offsets
    if QMultiOffset
        traceref = 30;
        k = find((f > fp1) & (f < fp2)); fm = f(k);
        n = 1;
        for trace = 1:length(offsetw)
            if sign(offsetw(traceref)) == sign(offsetw(trace))
                if abs(offsetw(trace)) > abs(offsetw(traceref))
                    SRm = log(DataA(k', trace) ./ DataA(k', traceref));
                    dx = abs(offsetw(trace)) - abs(offsetw(traceref));
                else
                    SRm = log(DataA(k', traceref) ./ DataA(k', trace));
                    dx = abs(offsetw(traceref)) - abs(offsetw(trace));
                end
                [p, S] = polyfit(fm, SRm, 1);
                slope = p(1);
                residuals_std = std(SRm - (slope * fm + p(2)));
                slope_std_error = residuals_std / sqrt(sum((fm - mean(fm)).^2) * (length(fm) -
                    1));
                Q(n) = -pi * dx / (ca * slope);
                Qerror(n) = slope_std_error * (pi * dx / (ca * slope^2));
                offsets(n) = offsetw(trace);
                n = n + 1;
            end
        end
        figure; hold on
        errorbar(offsets, Q, Qerror, 'b.', 'LineWidth', 0.8, 'MarkerSize', 10);
        xlabel('Offsets'); ylabel('Q'); grid on
        Q = Q(~isnan(Q)); Qerror = Qerror(~isnan(Qerror));
        Qmean = median(Q); Qerrormean = std(Q);
        legend(['Q = ', num2str(Qmean, '%.1f'), ' +/- ', num2str(Qerrormean, '%.2f')]);
        exportPublicationFigure(sprintf('Q_MultiOffset_shot%d', shot_num));
    end

%% Estimate Q at using all traces

    if Qcall,
        k=find((f>fp1)&(f<fp2)); fm=f(k); m=1;
```

```
        for traceref=1:length(offsetw),
            n=1;
            for trace=1:1:length(offsetw),

                if sign(offsetw(traceref))==sign(offsetw(trace))
                    if abs(offsetw(trace))>abs(offsetw(traceref))
                        SRm=log(DataA(k',trace)./DataA(k',traceref));
                        dx=abs(offsetw(trace))-abs(offsetw(traceref));
                    else
                        SRm=log(DataA(k',traceref)./DataA(k',trace));
                        dx=abs(offsetw(traceref))-abs(offsetw(trace));
                    end

                    [p,S] = polyfit(fm,SRm,1);

                    slope=p(1); intercept=p(2);

                    %claculate slope error
                    residuals_std = std(SRm - (slope*fm + intercept));
                    fm_mean = mean(fm);
                    fm_var = sum((fm - fm_mean).^2);
                    slope_std_error = residuals_std/sqrt(fm_var*(length(fm) - 1));

                    Q(n)=-pi*dx/(ca*slope);
                    Qerror(n)=slope_std_error*(pi*dx/(ca*slope*slope));


                    offsets(n)=offsetw(trace);
                    n=n+1;
                end
            end
            Q=Q(~isnan(Q'))';
            Qerror=Qerror(~isnan(Qerror'))';
            Qall(m)=median(Q);
            Qallerror(m)=std(Q);
            m=m+1;

        end
        figure; hold on
        errorbar(offsetw, Qall, Qallerror, 'b.', ...
            'LineWidth', 0.8, ...
            'MarkerSize', 10);
        xlabel('Offset (m)');
        ylabel('Q');

        grid on
        Qall=Qall(~isnan(Qall'))';
        Qallerror=Qallerror(~isnan(Qallerror'))';
        Qallmean=median(Qall);
        Qallerrormean=std(Qall);
        legend(['Global Q=',num2str(Qallmean,'%.1f'),' +/- ',num2str(Qallerrormean,'%.2f')],'
            Location', 'northeast');
        exportPublicationFigure(sprintf('All traces Q - Real Data shot%d',shot_num))

    end
    clear all

end
```

A.3 SOFI2D

- JSON file
- Source file

```
#-------------------------------------------------------------------
# JSON PARAMETER FILE FOR SOFI2D
#-------------------------------------------------------------------
# description: example of json input file
#

{
"Domain Decomposition" : "comment",
                         "NPROCX" : "2",
                         "NPROCY" : "2",

"FD order" : "comment",
                         "FDORDER" : "4",
                         "FDORDER_TIME" : "2",
                         "MAXRELERROR" : "0",

"2-D Grid" : "comment",
                         "NX" : "1000",
                         "NY" : "200",
                         "DH" : "0.1",

"Time Stepping" : "comment",
                         "TIME" : "0.6",
                         "DT" : "2.0e-5",

"Wave Equation" : "comment",
                         "WEQ" : "VEL_ISO",
                         "WEQ values : AC_ISO:acoustic isotropic, AC_VTI:acoustic
                             VTI, AC_TTI:acoustic TTI" : "comment",
                         "WEQ values : VAC_ISO:viscoacoustic isotropic, VAC_VTI:
                             viscoacoustic VTI, VAC_TTI:viscoacoustic TTI" : "
                             comment",
                         "WEQ values : EL_ISO:elastic isotropic, EL_VTI:elastic VTI,
                              EL_TTI:elastic TTI" : "comment",
                         "WEQ values : VEL_ISO:viscoelastic isotropic, VEL_VTI:
                             viscoelastic VTI, VEL_TTI:viscoelastic TTI" : "comment
                             ",

"Source" : "comment",

                         "SOURCE_SHAPE" : "1",
                         "SOURCE_SHAPE values: ricker=1;fumue=2;from_SIGNAL_FILE=3;
                             SIN**3=4;Berlage=5;Klauder=6" : "comment",
                         "SIGNAL_FILE" : "signal_mseis.tz",

                         "SIGOUT" : "1",
                         "Output source wavelet: yes=1, no=else" : "comment",
                         "SIGOUT_FILE" : "./seis/P_5_Median/source_signal_P_5_Median
                             ",
                         "SIGOUT_FORMAT" : "1",
                         "Supported output formats for SIGOUT_FORMAT: SU=1, ASCII=2,
                              BINARY=3" : "comment",

                         "SOURCE_TYPE" : "3",
                         "SOURCE_TYPE values (point_source): explosive=1;force_in_x
                             =2;force_in_y=3;custom_force=4" : "comment",

                         "SRCREC" : "1",
                         "SRCREC values :  read from SOURCE_FILE=1, PLANE_WAVE=2 (
                             internal)" : "comment",

                         "SOURCE_FILE" : "./sources/source.dat",
                         "RUN_MULTIPLE_SHOTS" : "1",
```

```
                        "PLANE_WAVE_DEPTH" : "2106.0",
                        "PLANE_WAVE_ANGLE" : "0.0",
                        "TS" : "0.2",

"Model" : "comment",
                        "READMOD" : "1",
                        "MFILE" : "./model/P_5_Median/P_5_Median",
                        "WRITE_MODELFILES" : "0",

"Q-approximation" : "comment",
                        "L" : "5",
                        "F_REF": "30.0",
                        "FL1" : "1.9",
                        "FL2" : "5.4",
                        "FL3" : "20.1",
                        "FL4" : "77.7",
                        "FL5" : "137.1",


"Boundary Conditions" : "comment",
                        "FREE_SURF" : "1",
                        "BOUNDARY" : "0",

                        "FW" : "40",
                        "ABS_TYPE" : "1",
                        "ABS_TYPE values : CPML-Boundary=1; Damping-Boundary=2" : "
                            comment",

                        "Parameter for CPML (ABS_TYPE=1)" : "comment",
                        "NPOWER" : "4.0",
                        "K_MAX_CPML" : "1.0",
                        "VPPML" : "3500.0",
                        "FPML" : "5.0",

                        "Parameter for ABS_TYPE=2" : "comment",
                        "DAMPING" : "8.0",


"Snapshots" : "comment",
                        "SNAP" : "1",
                        "TSNAP1" : "0.02",
                        "TSNAP2" : "0.5",
                        "TSNAPINC" : "0.02",
                        "IDX" : "1",
                        "IDY" : "1",
                        "SNAP_FORMAT" : "3",
                        "SNAP_FILE" : "./snap/P_5_Median/HK5_Median",

"Receiver" : "comment",
                        "SEISMO" : "1",
                        "READREC" : "0",
                        "REC_FILE" : "./receiver/receiver.dat",
                        "REFRECX, REFRECY" : "0.0 , 0.0",
                        "XREC1,YREC1" : "15.0 , 0.1",
                        "XREC2,YREC2" : "86.0 , 0.1",
                        "NGEOPH" : "10",

"Receiver array" : "comment",

                        "REC_ARRAY" : "0",
                        "REC_ARRAY_DEPTH" : "70.0",
                        "REC_ARRAY_DIST" : "40.0",
                        "DRX" : "4",

"Seismograms" : "comment",
                        "NDT" : "1",
                        "SEIS_FORMAT" : "1",
                        "SEIS_FILE" : "./seis/P_5_Median/P_5_Median",
```

```
"Monitoring the simulation" : "comment",
                        "LOG_FILE" : "./log/2layer.log",
                        "LOG" : "0",
                        "LOG_VERBOSITY" : "INFO",
                        "OUT_TIMESTEP_INFO" : "100"
}

#-------------------------------------------------------------------
# SOURCE PARAMETER FILE FOR SOFI2D
#-------------------------------------------------------------------
#
# SOURCE PARAMETERS FIRST PROFILE
# ----------------------------------------------------------
#14.0    0.1    0.0    30.0    1.0
#18.0    0.1    0.0    30.0    1.0
#22.0    0.1    0.0    30.0    1.0
#26.0    0.1    0.0    30.0    1.0
#30.0    0.1    0.0    30.0    1.0
#34.0    0.1    0.0    30.0    1.0
#38.0    0.1    0.0    30.0    1.0
#42.0    0.1    0.0    30.0    1.0
#46.0    0.1    0.0    30.0    1.0
#50.0    0.1    0.0    30.0    1.0
#54.0    0.1    0.0    30.0    1.0
#58.0    0.1    0.0    30.0    1.0
#62.0    0.1    0.0    30.0    1.0
#66.0    0.1    0.0    30.0    1.0
#70.0    0.1    0.0    30.0    1.0
#70.0    0.1    0.0    30.0    1.0
#74.0    0.1    0.0    30.0    1.0
#78.0    0.1    0.0    30.0    1.0
#82.0    0.1    0.0    30.0    1.0
#86.0    0.1    0.0    30.0    1.0


# SOURCE PARAMETERS SECOND PROFILE
# ----------------------------------------------------------
#14.0    0.1    0.0    30.0    1.0
#18.0    0.1    0.0    30.0    1.0
#21.0    0.1    0.0    30.0    1.0
#25.0    0.1    0.0    30.0    1.0
#29.0    0.1    0.0    30.0    1.0
#33.0    0.1    0.0    30.0    1.0
#37.0    0.1    0.0    30.0    1.0
#41.0    0.1    0.0    30.0    1.0
#45.0    0.1    0.0    30.0    1.0
#49.0    0.1    0.0    30.0    1.0
#53.0    0.1    0.0    30.0    1.0
#57.0    0.1    0.0    30.0    1.0
#61.0    0.1    0.0    30.0    1.0
#65.0    0.1    0.0    30.0    1.0
#69.0    0.1    0.0    30.0    1.0
#73.0    0.1    0.0    30.0    1.0
#77.0    0.1    0.0    30.0    1.0
#81.0    0.1    0.0    30.0    1.0
#85.0    0.1    0.0    30.0    1.0
#89.0    0.1    0.0    30.0    1.0

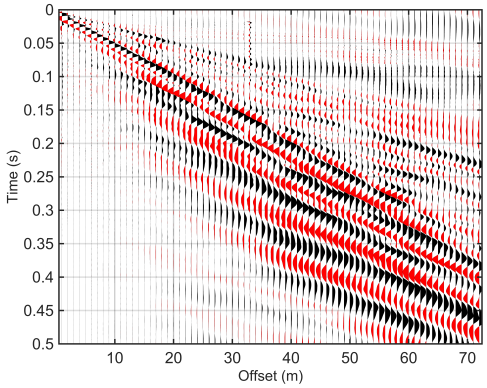
# ----------------------------------------------------------
# Parameters for each source node (one source node per line):
#
# XSRC  YSRC    TD      FC      AMP     [SOURCE_AZIMUTH]        [SOURCE_TYPE]
#
# Definition of (distributed) source positions:
#
# Symbols:
# XSRC= x-coordinate of source point [meter]
# YSRC= y-coordinate of source point [meter] (vertical direction)
# TD= excitation time (time-delay) for source node [s]
# FC= centre frequency of source signal [Hz]
```

```
# AMP= maximum amplitude of source signal
#
# Optional:
# SOURCE_AZIMUTH= if SOURCE_TYPE is 4, source_azimuth is
#                 the angle between the y- and x-direction
# SOURCE_TYPE= if source_type is set here, the value SOURCE_TYPE
#              in the input file is ignored.
#
```

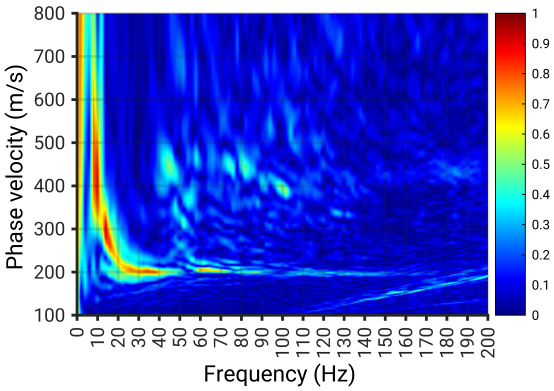
Appendix B

Seismogram/Dispersion images of Herrenknecht test site

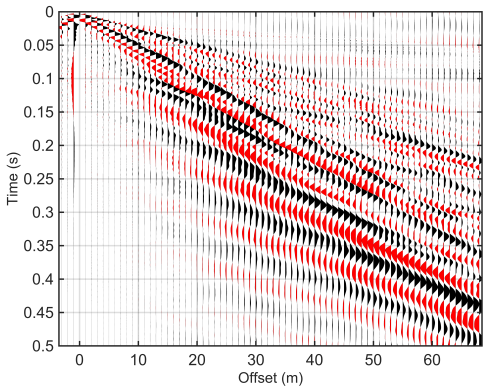
B.1 Profile 1



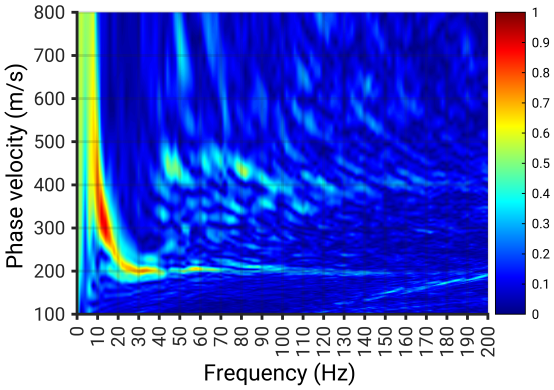
Shot 1



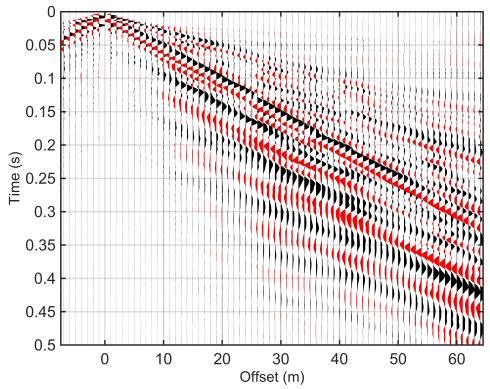
Dispersion image 1



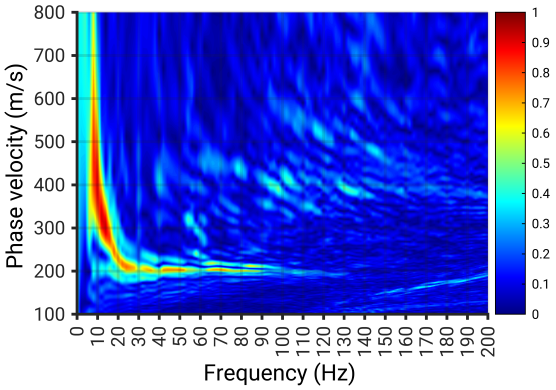
Shot 2



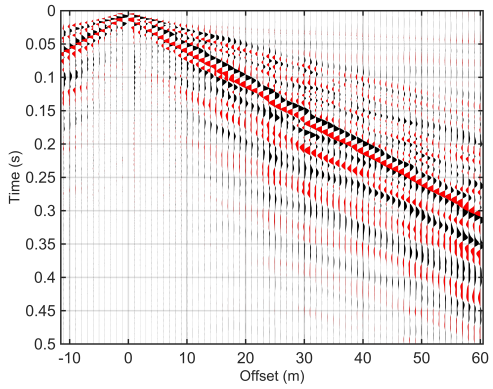
Dispersion image 2



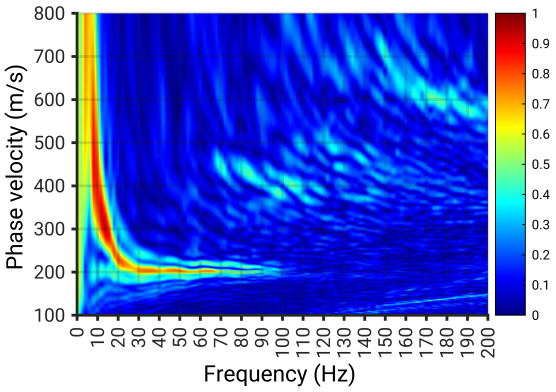
Shot 3



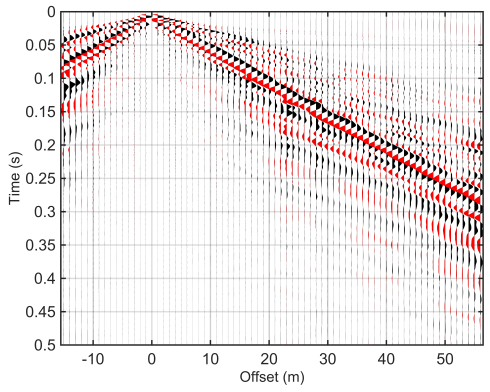
Dispersion image 3



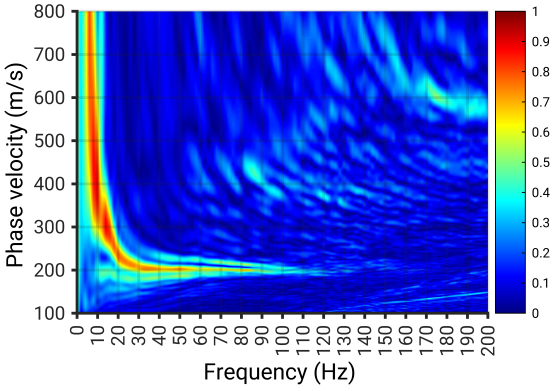
Shot 4



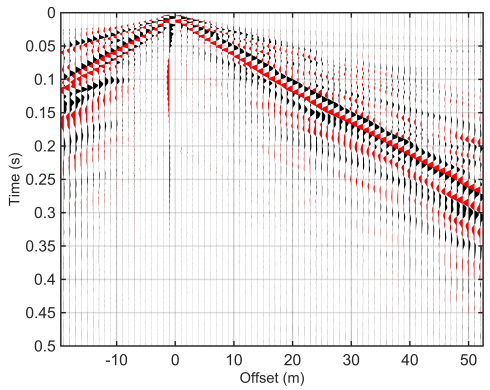
Dispersion image 4



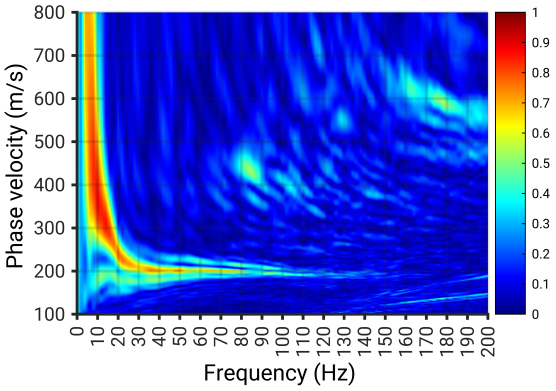
Shot 5



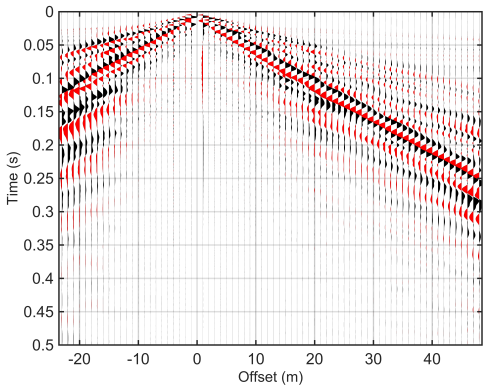
Dispersion image 5



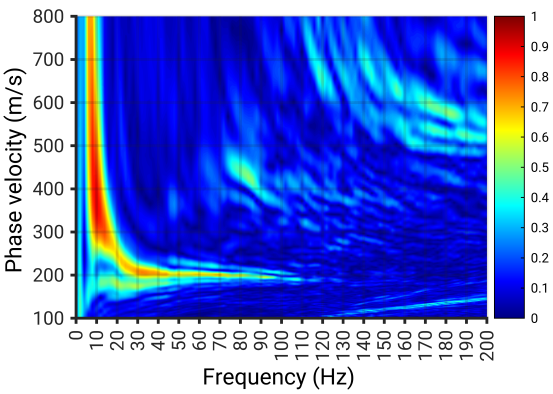
Shot 6



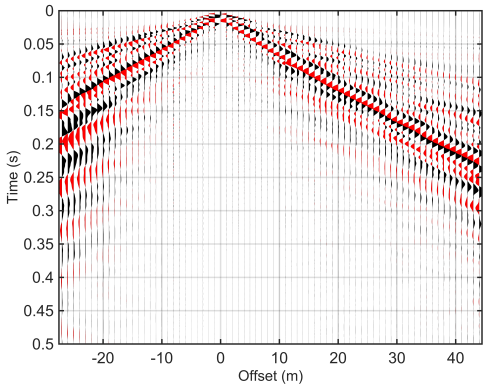
Dispersion image 6



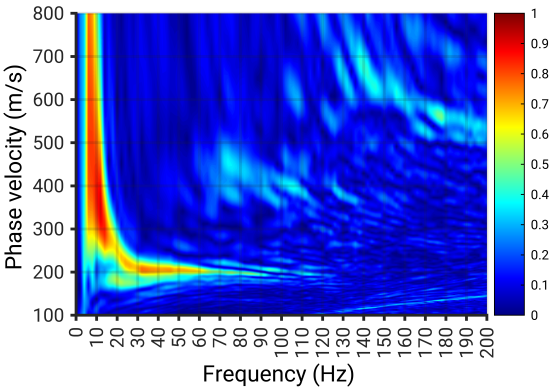
Shot 7



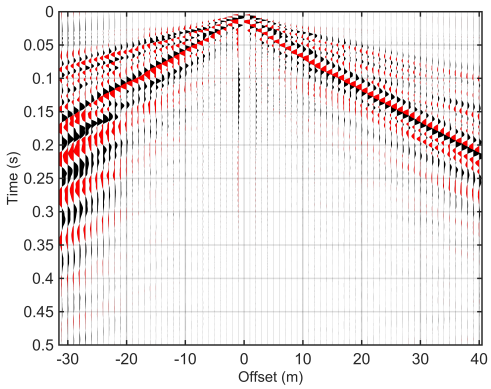
Dispersion image 7



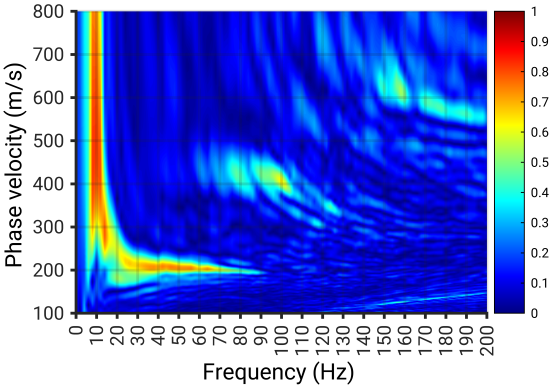
Shot 8



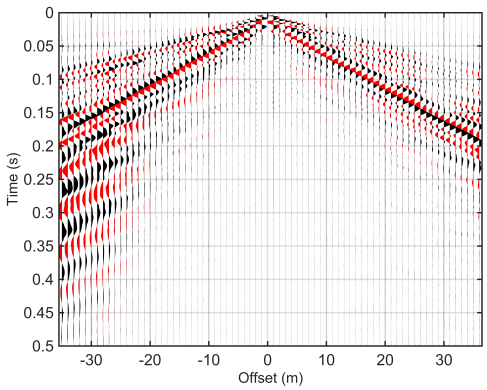
Dispersion image 8



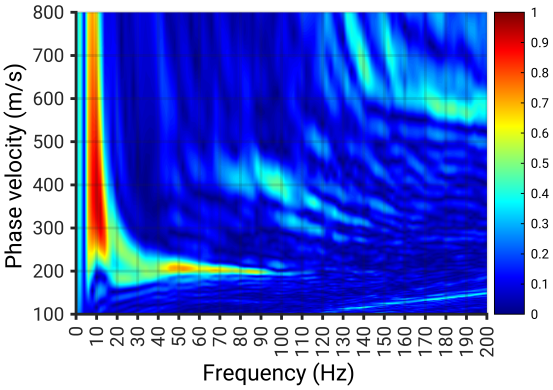
Shot 9



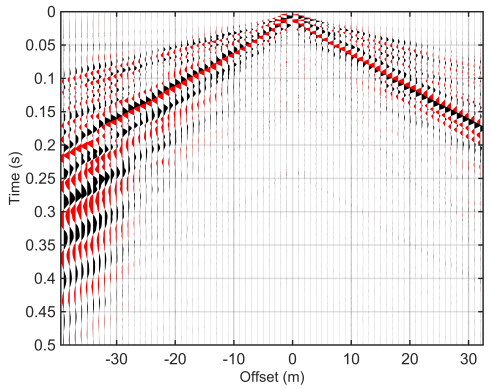
Dispersion image 9



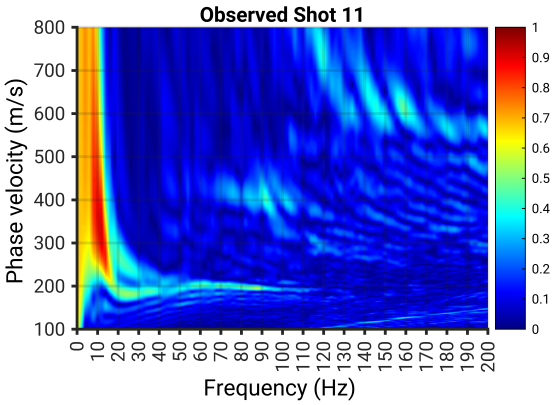
Shot 10



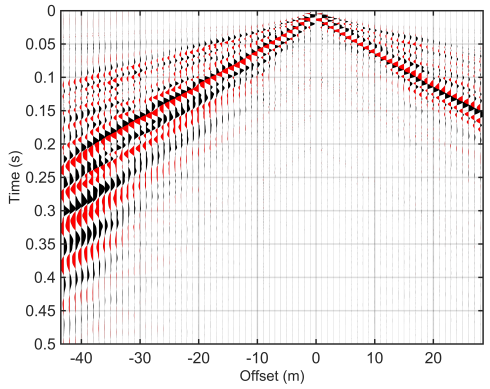
Dispersion image 10



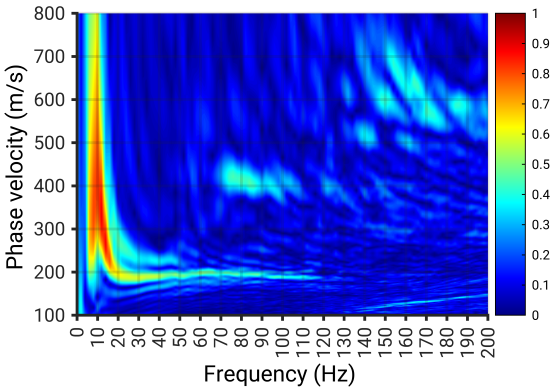
Shot 11



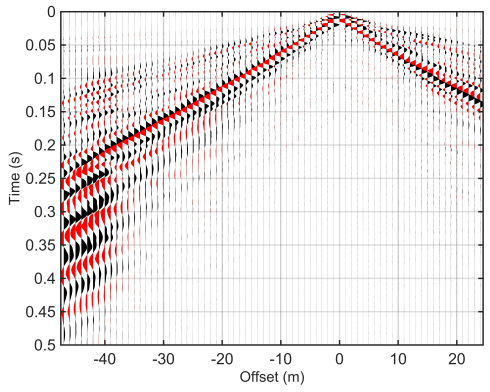
Dispersion image 11



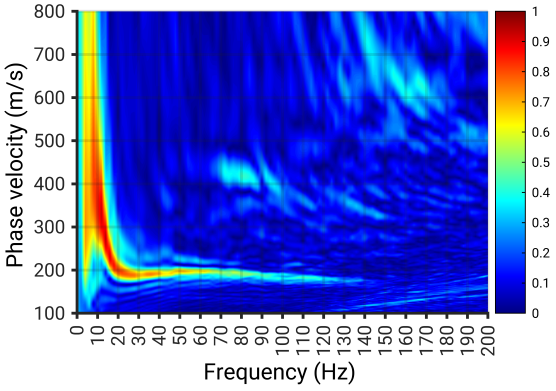
Shot 12



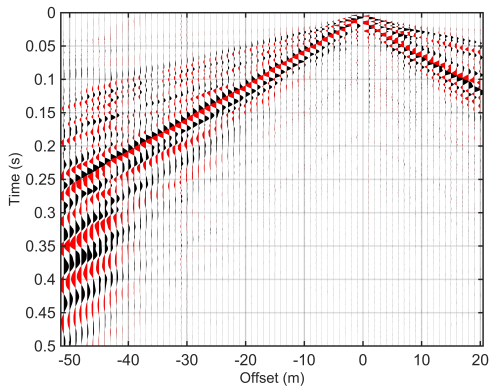
Dispersion image 12



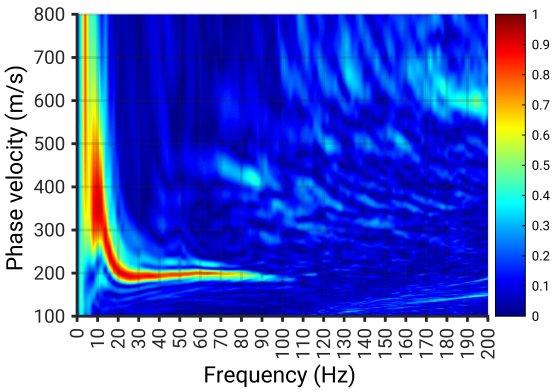
Shot 13



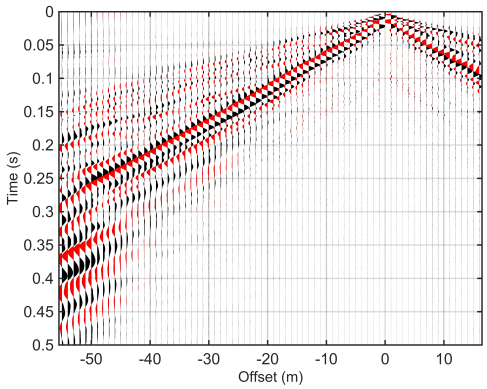
Dispersion image 13



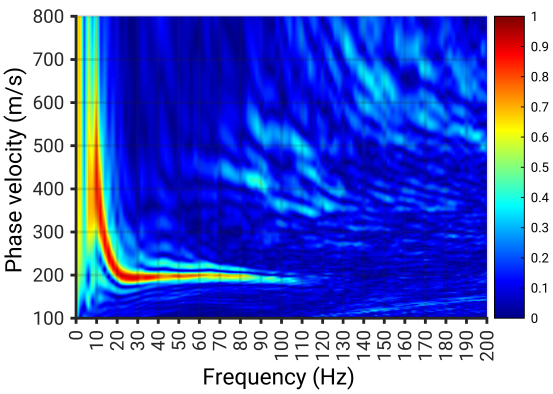
Shot 14



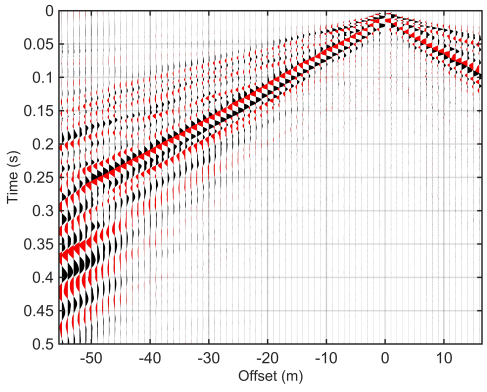
Dispersion image 14



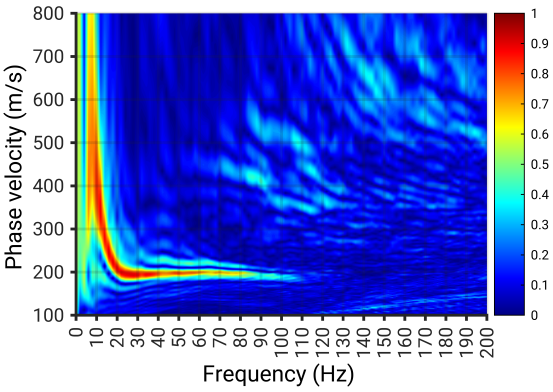
Shot 15



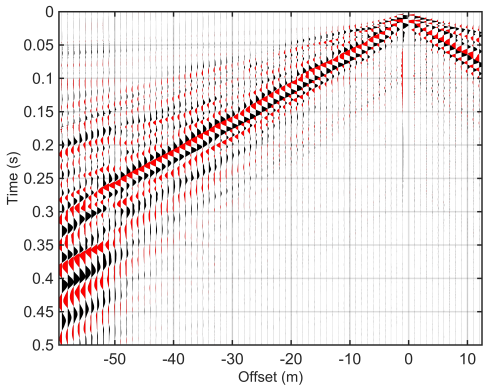
Dispersion image 15



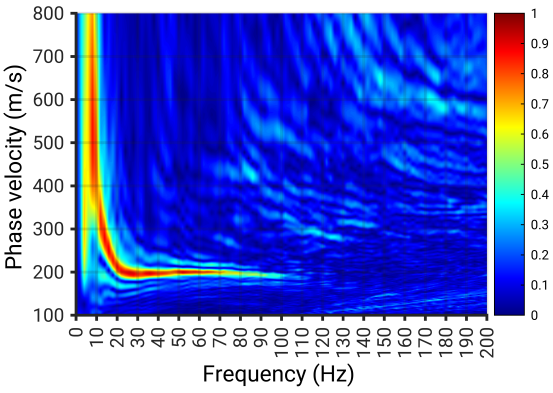
Shot 16



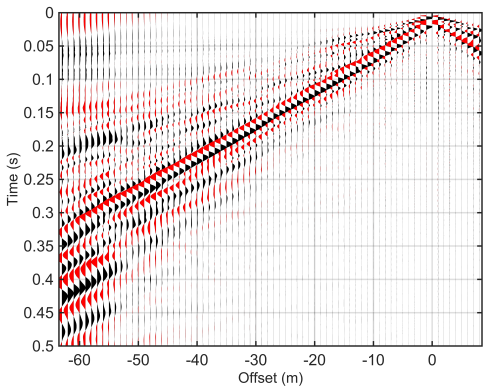
Dispersion image 16



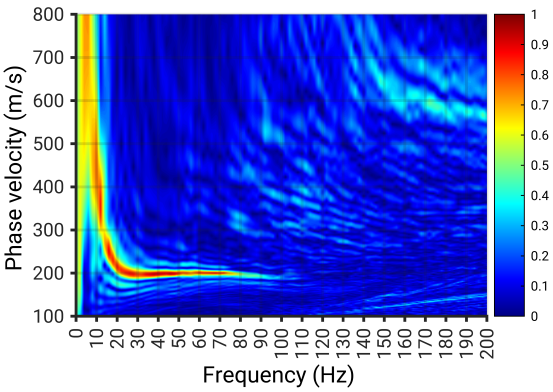
Shot 17



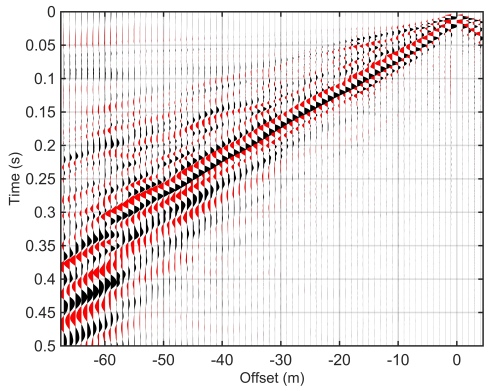
Dispersion image 17



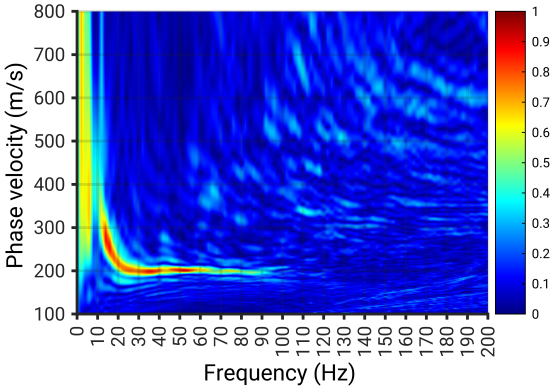
Shot 18



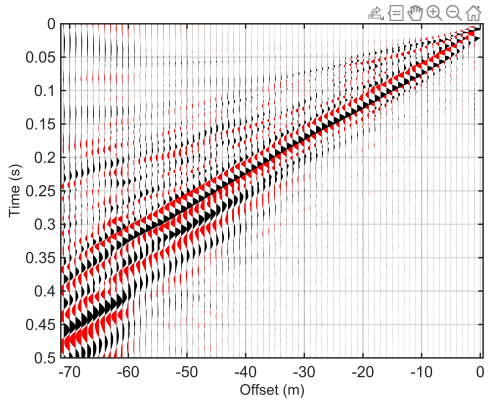
Dispersion image 18



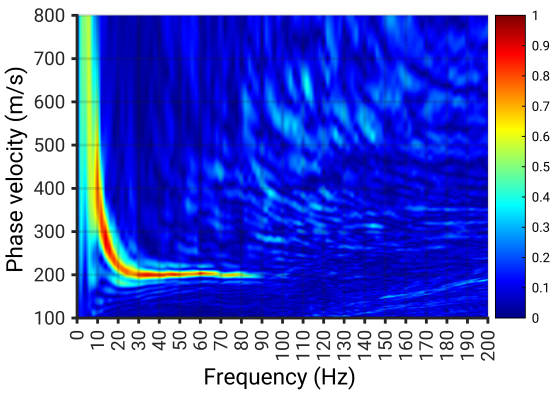
Shot 19



Dispersion image 19

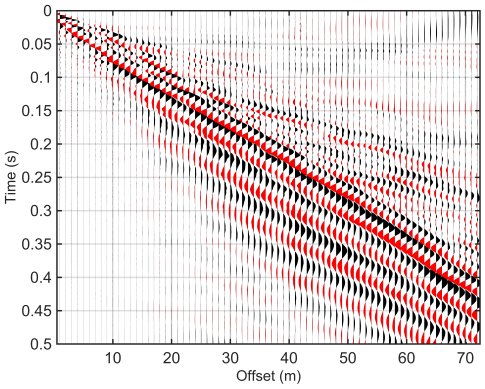


Shot 20

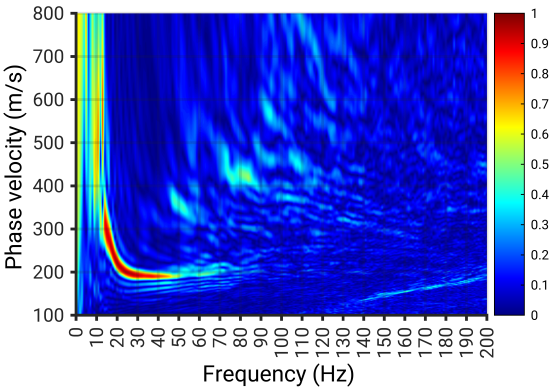


Dispersion image 20

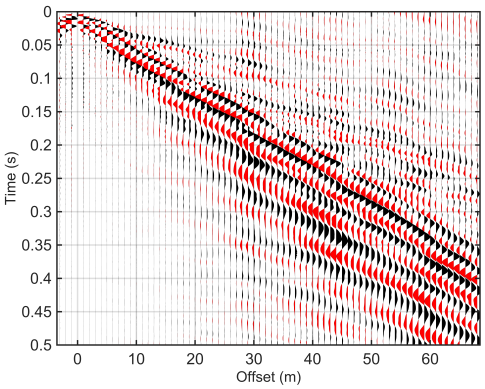
B.2 Profile 2



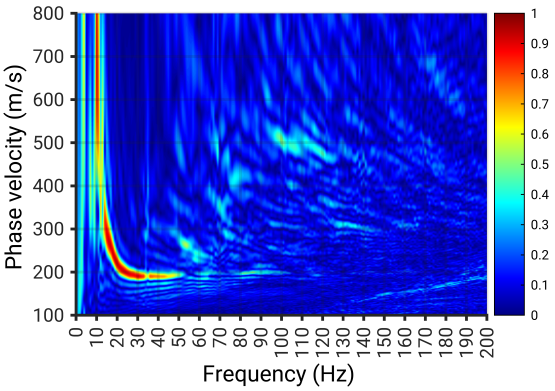
Shot 28



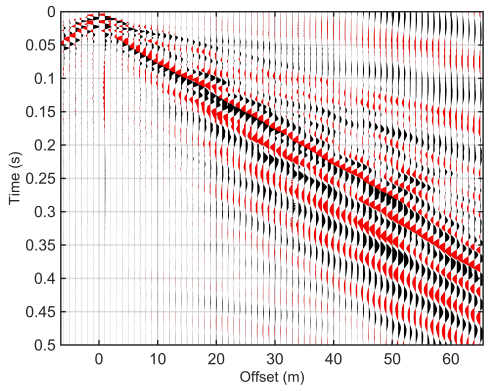
Dispersion image 28



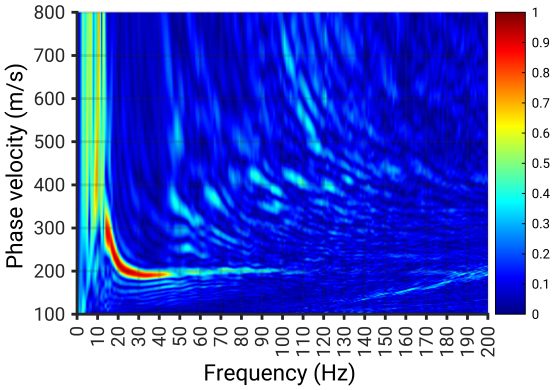
Shot 29



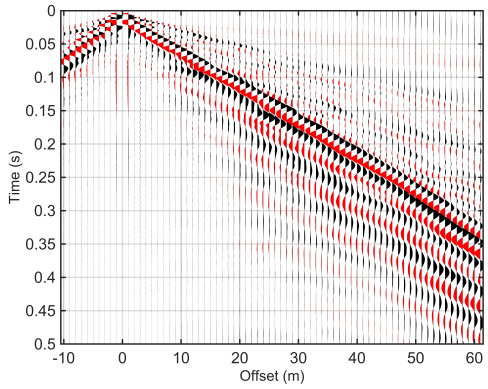
Dispersion image 29



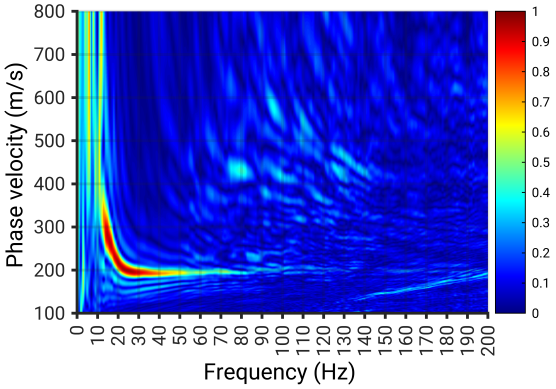
Shot 30



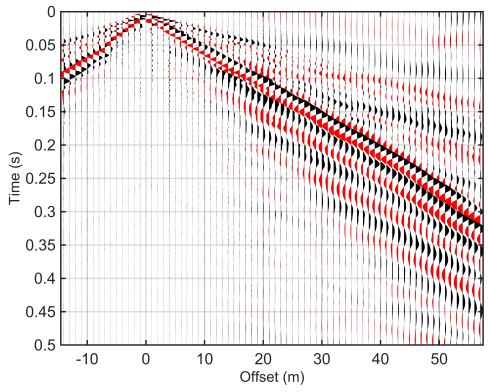
Dispersion image 30



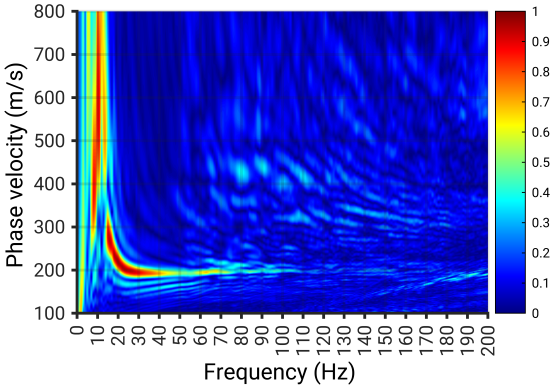
Shot 31



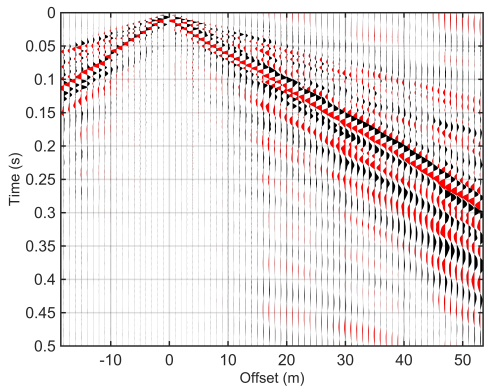
Dispersion image 31



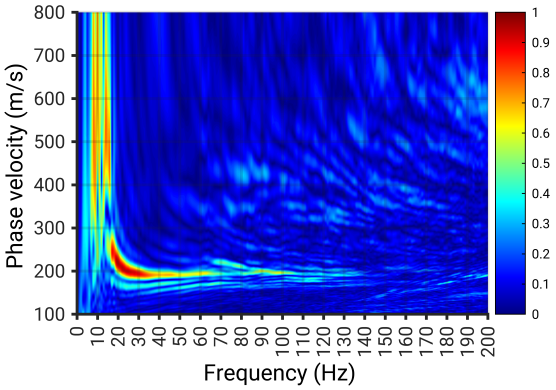
Shot 32



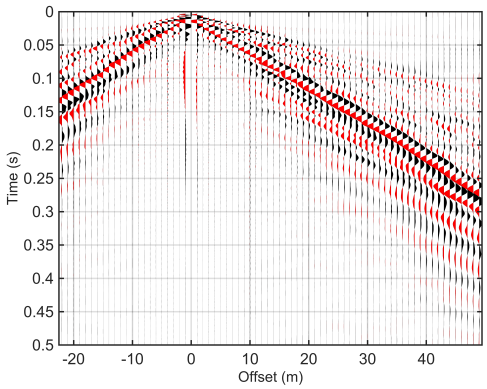
Dispersion image 32



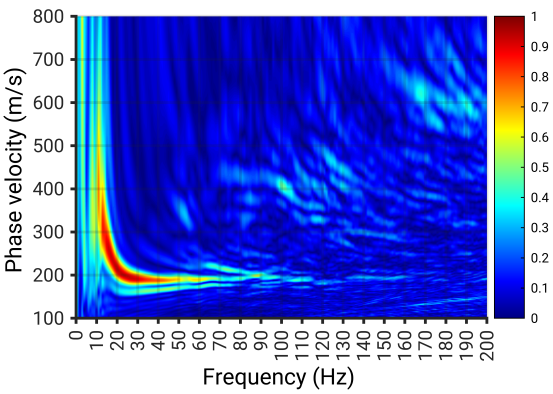
Shot 33



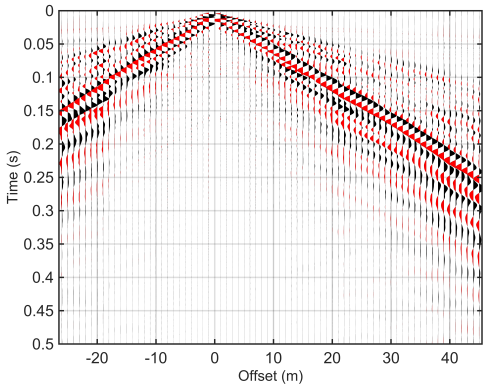
Dispersion image 33



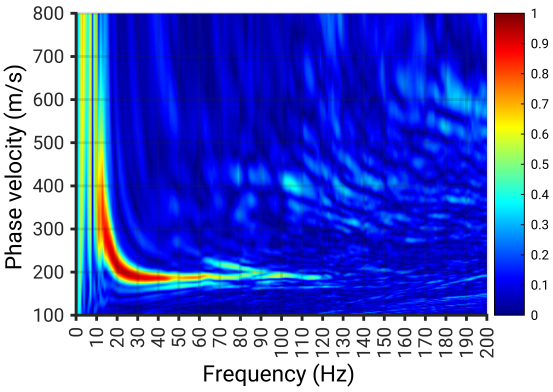
Shot 34



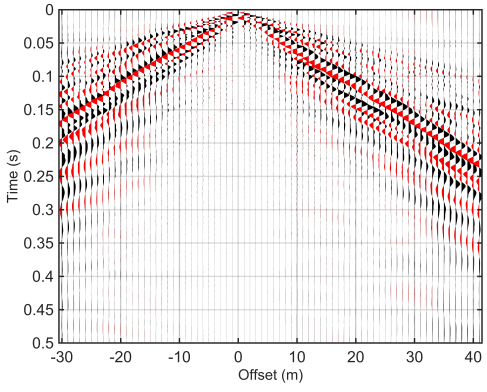
Dispersion image 34



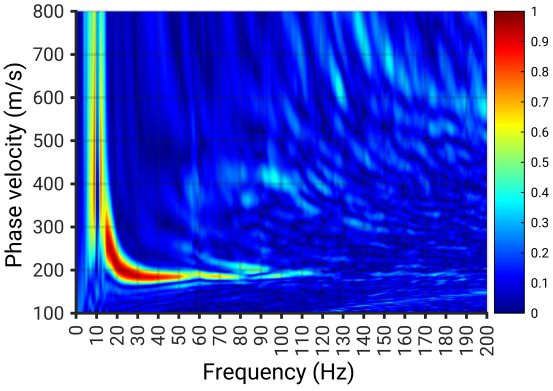
Shot 35



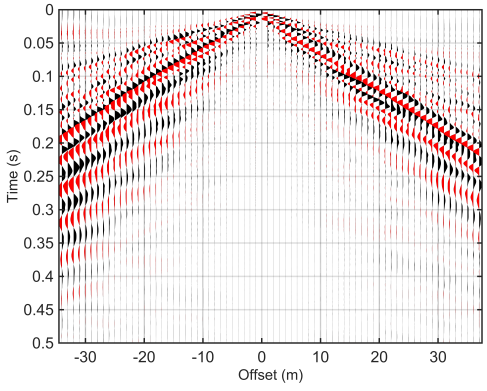
Dispersion image 35



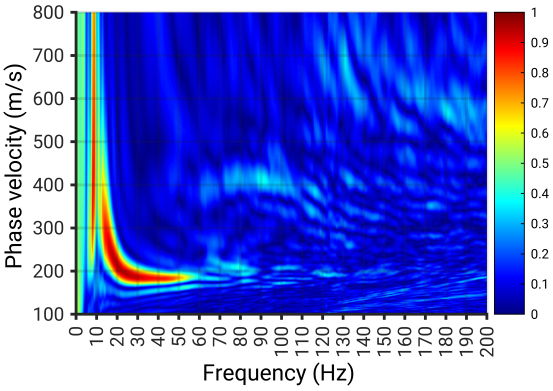
Shot 36



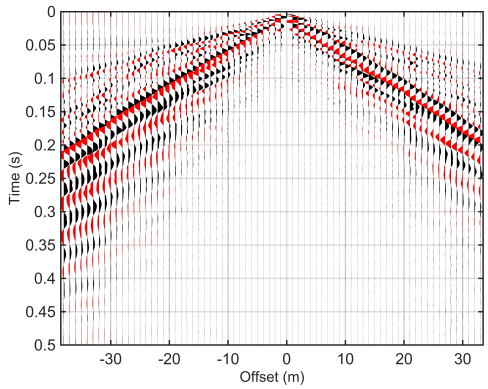
Dispersion image 36



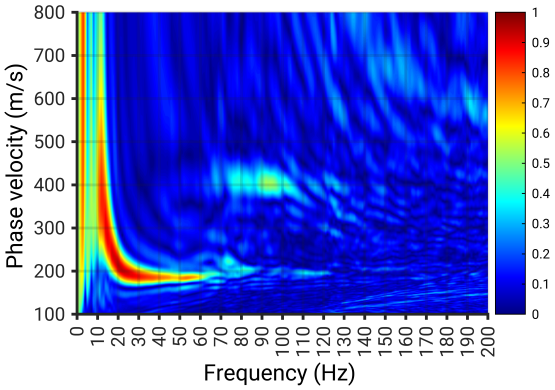
Shot 37



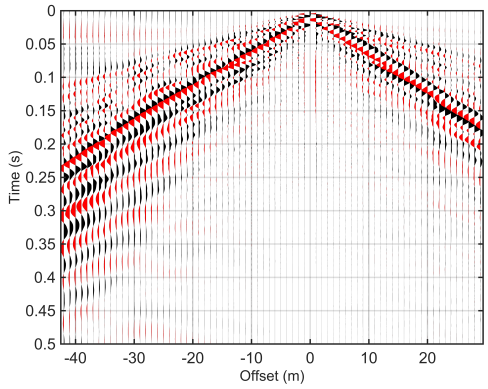
Dispersion image 37



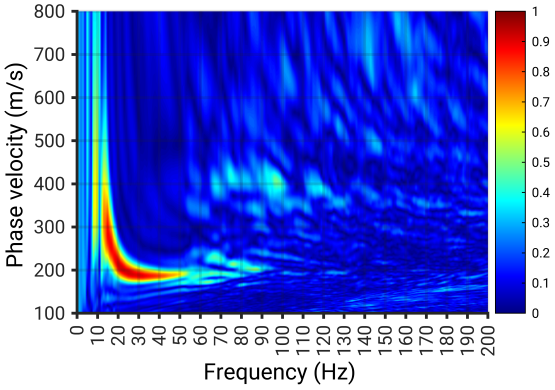
Shot 38



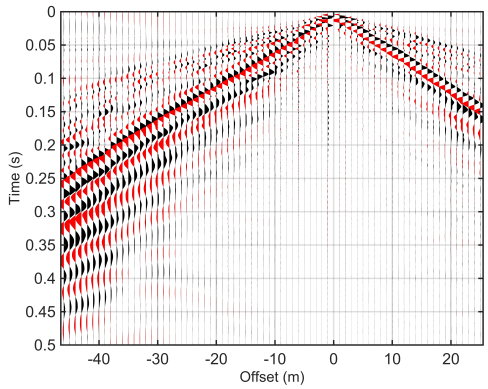
Dispersion image 38



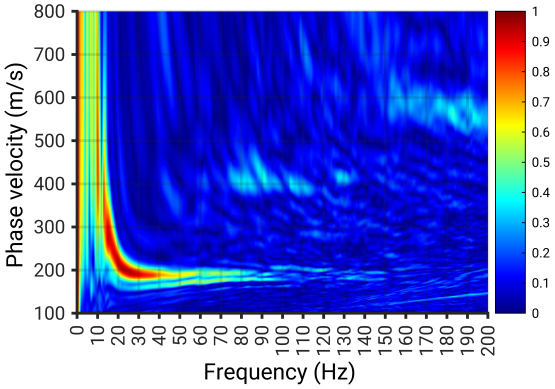
Shot 39



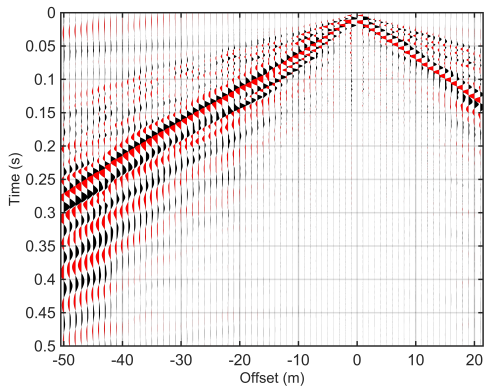
Dispersion image 39



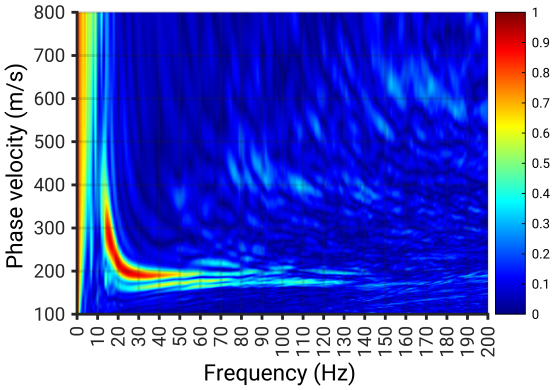
Shot 40



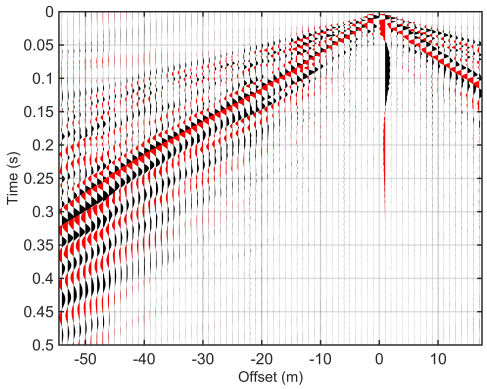
Dispersion image 40



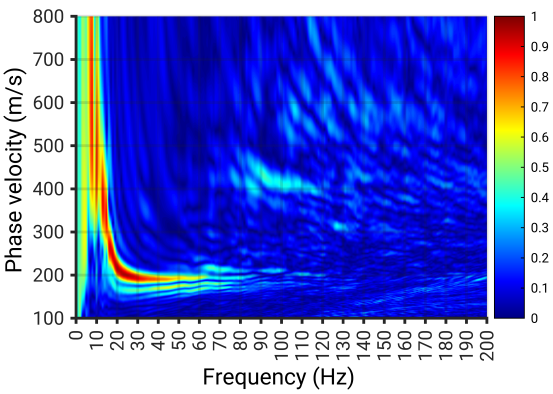
Shot 41



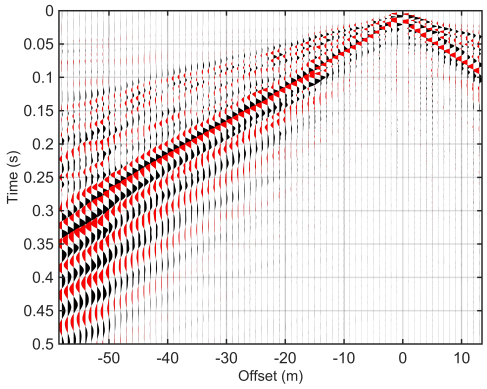
Dispersion image 41



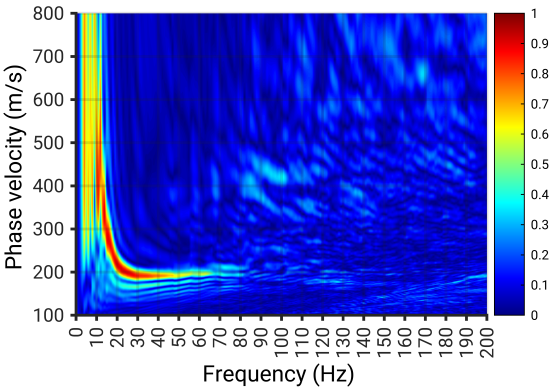
Shot 42



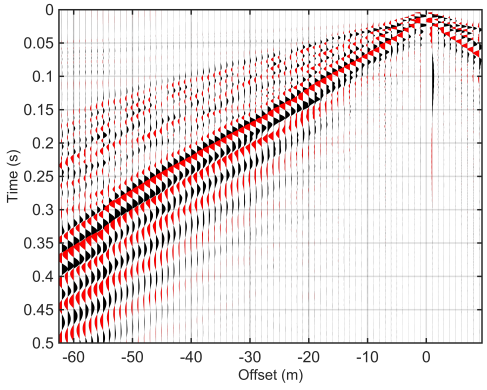
Dispersion image 42



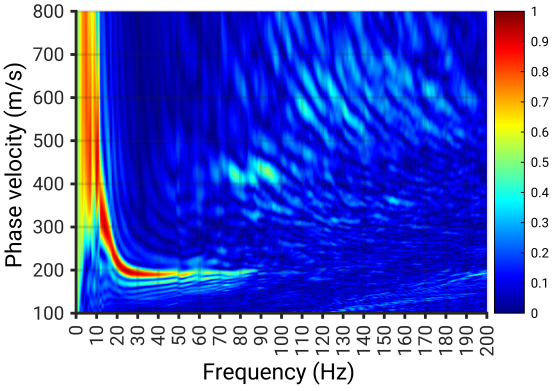
Shot 43



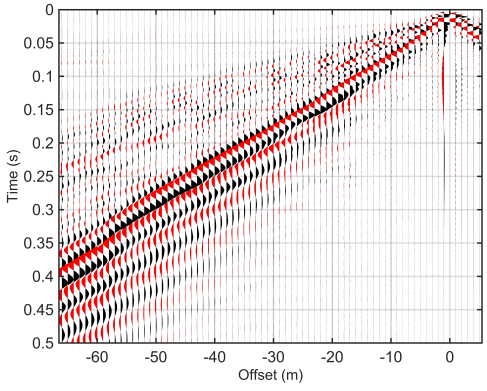
Dispersion image 43



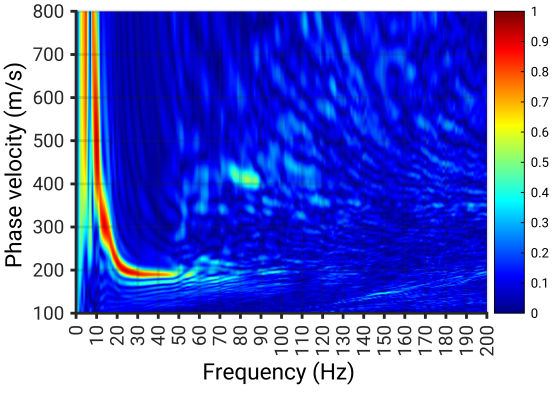
Shot 44



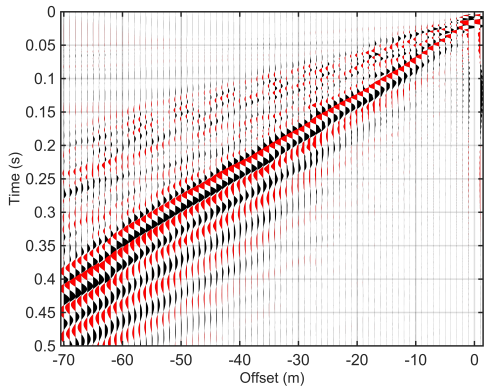
Dispersion image 44



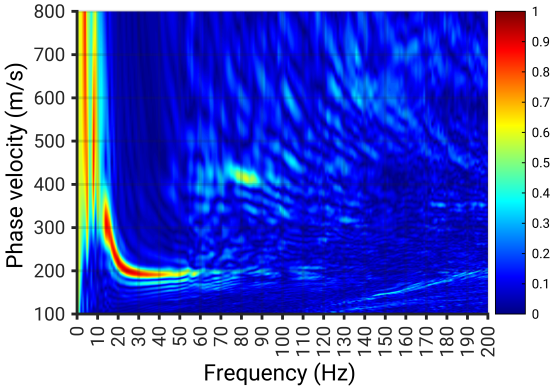
Shot 45



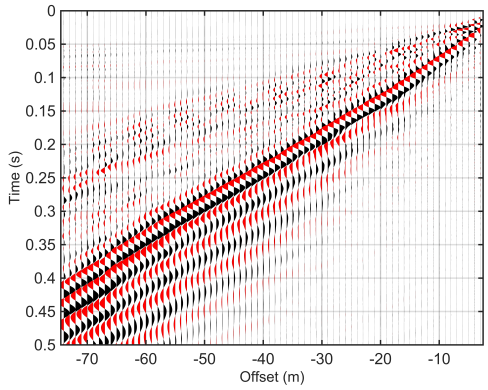
Dispersion image 45



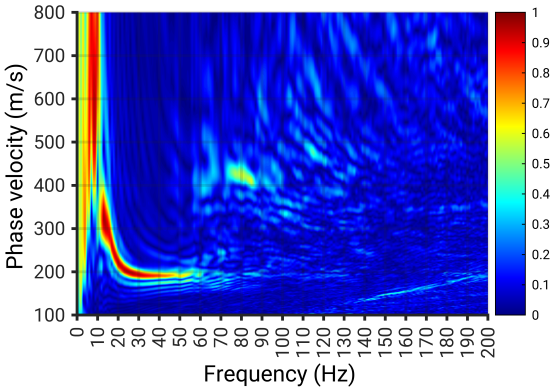
Shot 46



Dispersion image 46



Shot 47



Dispersion image 47

Bibliography

Aki, K. and Richards, P. G. (2002). *Quantitative Seismology*. 2nd ed. University Science Books. ISBN: 0935702962.

Bai, T. and Tsvankin, I. (2016). "Time-domain finite-difference modeling for attenuative anisotropic media". *geophysics* 81, pp. C69–C77. DOI: 10.1190/geo2015-0424.1.

Båth, M. (1974). *Spectral analysis in geophysics*. Developments in solid earth geophysics v. 7. Elsevier Scientific Pub. Co. ISBN: 978-0-444-41222-5.

Blanch, J. O. (1996). "A study of viscous effects in seismic modeling, imaging, and inversion: methodology, computational aspects, and sensitivity". PhD thesis. Rice University.

Bohlen, T. (1998). "Viskoelastische FD-Modellierung seismischer Wellen zur Interpretation gemessener Seismogramme". PhD thesis. Kiel University.

Bohlen, T. (2002). "Parallel 3-D viscoelastic finite difference seismic modelling". *Computers & Geosciences* 28.8, pp. 887–899. DOI: 10.1016/S0098-3004(02)00006-7.

Bohlen, T., De Nil, D., Köhn, D., and Jetschny, S. (2016). *SOFI2D - seismic modeling with finite dif/ Geoforschungszentrum Potsdamferences: 2D - elastic and viscoelastic version*. Updated 2022. URL: https://gitlab.kit.edu/kit/gpi/ag/software/sofi2d.

Clauser, C. (2018). *Grundlagen der angewandten Geophysik - Seismik, Gravimetrie*. Springer Berlin Heidelberg. DOI: 10.1007/978-3-662-55310-7.

Kjartansson, E. (1979). "Constant Q-wave propagation and attenuation". *Journal of Geophysical Research: Solid Earth* 84.B9, pp. 4737–4748.

Kramer, S. L. (1996). *Geotechnical earthquake engineering*. Prentice-Hall international series in civil engineering and engineering mechanics. Prentice Hall.

Lay, T. and Wallace, T. C. (1995). *Modern global seismology*. International geophysics series v. 58. Academic Press. ISBN: 978-0-12-732870-6.

Liu, H.-P., Anderson, D. L., and Kanamori, H. (1976). "Velocity dispersion due to anelasticity; implications for seismology and mantle composition". *Geophysical Journal International* 47.1, pp. 41–58. DOI: 10.1111/j.1365-246X.1976.tb01261.x.

MASWaves User Manual (2017). User manual for MASWaves software. Faculty of Civil and Environmental Engineering, University of Iceland. URL: https://uni.hi.is/eao4/maswaves_download/.

Müller, G. and Weber, M. (2007). "Theory of elastic waves". *Scientific Technical Report*. DOI: 10.23689/fidgeo-558.

Nazarian, S., Stokoe, K. H., and Hudson, W. R. (1983). "Use of spectral analysis of surface waves method for determination of moduli and thicknesses of pavement systems."

Transportation Research Record, pp. 38–45. URL: https://api.semanticscholar.org/CorpusID:58935998.

Nelder, J. A. and Mead, R. (1965). "A Simplex Method for Function Minimization". *The Computer Journal* 7.4, pp. 308–313. DOI: 10.1093/comjnl/7.4.308.

Olafsdottir, E. A. (2016). "Multichannel Analysis of Surface Waves for assessing soil stiffness". M.Sc. thesis. Faculty of Civil and Environmental Engineering, University of Iceland.

Olafsdottir, E. A., Erlingsson, S., and Bessason, B. (2018). "Tool for analysis of multichannel analysis of surface waves (MASW) field data and evaluation of shear wave velocity profiles of soils". *Canadian Geotechnical Journal* 55.2, pp. 217–233. DOI: 10.1139/cgj-2016-0302.

Park, C. (1998). "Imaging dispersion curves of surface waves on multi-channel record". *SEG Technical Program Expanded Abstracts* 17. DOI: 10.1190/1.1820161.

Park, C. and Carnevale, M. (2010). "Optimum MASW survey - Revisit after a Decade of Use". *Geotechnical Special Publication*, pp. 1303–1312. DOI: 10.1061/41095(365)130.

Park, C. B. and Adkins-Heljeson, M. (2006). *SurfSeis – Active and Passive MASW: User's Manual V 2.0*. Software manual for geophysical subsurface imaging tools. Kansas Geological Survey.

Socco, L. V., Foti, S., and Boiero, D. (2010). "Surface-wave analysis for building near-surface velocity models — Established approaches and new perspectives". *geophysics* 75.5, 75A83–75A102. DOI: 10.1190/1.3479491.

Stokoe, K., Wright, S., Bay, J., and Roesset, J. (1994). "Characterization of Geotechnical Sites by SASW Method". In: *Geophysical Characterization of Sites*. Ed. by R. Woods. ISSMFE Technical Committee, pp. 15–25.

Tonn, R. (1989). "Comparison of seven methods for the computation of Q". *Physics of the Earth and Planetary Interiors* 55.3, pp. 259–268. DOI: https://doi.org/10.1016/0031-9201(89)90074-5.

Xia, J., Miller, R., and Park, C. (1999). "Multichannel analysis of surface waves". *geophysics* 64.3, pp. 800–808. DOI: 10.1190/1.1444590.

Xia, J., Miller, R., Park, C., and Ivanov, J. (2000). "Construction of 2-D Vertical Shear-Wave Velocity Field by the Multichannel Analysis of Surface Wave Technique". *SAGEEP 2000*, pp. 1197–1206. DOI: 10.4133/1.2922726.

Xia, J., Miller, R., Park, C., and Tian, G. (2002). "Determining Q of near-surface materials from Rayleigh waves". *Journal of Applied Geophysics* 51, pp. 121–129. DOI: 10.1016/S0926-9851(02)00228-8.

Zener, C. (1948). *Elasticity and Anelasticity of Metals*. Chicago University Committee on Publications in the Physical Sciences. University of Chicago Press. ISBN: 978-0-226-98054-6.

Acknowledgments

First and foremost, I would like to express my deepest gratitude to God for granting me the strength, perseverance, and clarity to complete this thesis.

I would like to extend my heartfelt thanks to my supervisor, Prof. Dr. Thomas Bohlen, for assigning me this topic and for his unwavering support, open-mindedness, and invaluable advice throughout the research and writing process. His willingness to answer all my questions with patience and insight have been greatly appreciated.

I am also sincerely grateful to Dr. Thomas Hertweck, Dr. Laura Gaßner, and Dr. Lars Houpt for their assistance with proofreading, corrections, and thoughtful feedback.

Finally, I want to thank my family and everyone who offered their support, whether emotionally, intellectually, or practically, during my studies.